Title
Characterization of the Spinal Disc-Vertebra Interface and its Relation to Injury and Back Pain

Author
Berg-Johansen, Britta

Publication Date
2017

Peer reviewed|Thesis/dissertation

Characterization of the Spinal Disc-Vertebra Interface and its Relation to Injury and Back Pain

by

Britta Berg-Johansen

DISSERTATION

Submitted in partial satisfaction of the requirements for the degree of

DOCTOR OF PHILOSOPHY

in

Bioengineering

in the

GRADUATE DIVISION

of the

UNIVERSITY OF CALIFORNIA, SAN FRANCISCO

AND

UNIVERSITY OF CALIFORNIA, BERKELEY

Acknowledgments

I have not gotten to where I am today on my own. I have had amazing supporters throughout my life who have inspired and motivated me beyond belief.

First, I want to thank everyone in the Berkeley-UCSF Bioengineering program who I have worked with and became friends with over the past five years. I want to give a special thanks to **Dr. Jeff Lotz**, who is truly the ultimate graduate advisor. He is motivating and positive, and mentors with patience and good humor. Jeff has managed to build a lab with a culture of collaboration and support, that is both academically rigorous *and* enjoyable. I also want to thank **Dr. Sunita Ho** and **Dr. Grace O'Connell**, my dissertation committee members, for offering their support and helpful expertise towards my research goals. I want to thank **Dr. Aaron Fields** for being a patient, devoted, and selfless mentor. Aaron is one of the most meticulous and hard-working researchers I have known, and is always generous with his time, carefully listening and offering brilliant ideas.

Annie, thank you for being the best bench-mate and lunchtime crossword collaborator. You might be the kindest human I have ever met. **Jeannie**, thank you for taking coffee breaks with me and keeping me going with your electric energy and sarcastic wit. Your assessments that my outfits were "on point" helped get me through days with failed experiments. Thanks to **Devante, Alice, and Ellen** for being truly awesome lab mates, and thanks to **Julea** for being my grad school BFF and sharing countless fun times, including kayaking in the bay, coming up with puns and new songs, and eating *all* of the macaroni and cheese.

Equally as important to my success and happiness, I want to thank my family for their endless love and support. My family is the most fun, vibrant, and loving family on the planet – I'm

pretty sure of it. My family is always on my side, and I never forget how lucky I am. They have taught me the religion of love and have shaped me into the person I am today.

I will never be able to put into words how much **my mom**, Bonnie Bruerd, has inspired and motivated me over the years. My mom is the most positive person I know, and has taught me how to be resilient and take life's challenges in stride. She has taught me to dance like nobody's watching, and get everyone around me to join. It is becoming increasingly clear that I am turning into my mother, and I could not be happier about this realization. Upon completion of this dissertation, I will be an official new member of the "Fun Doctors," a group of exuberant ladies with doctoral degrees that consists of my mom and her best friends.

My dad, Roar Berg-Johansen, is the most practical, down-to-earth human on the planet, and has kept me leveled throughout my many years of engineering school. Anyone who knows my dad would describe him as silly and optimistic, and I have always admired his air of calm confidence. My dad is a nerd like me, and inspired me to become an engineer through childhood activities like building circuits and taking apart watches and metronomes.

Huge shout-out to **my brother**, Erik Berg-Johansen, for being the coolest brother and a truly quality human being. As I told Erik last week, he "pushed my buttons" so much growing up that now my buttons are broken. In all seriousness, his joking and pranking throughout our childhood taught me to laugh at my mistakes and not take life too seriously. I cannot think of happier times than making music with my brother and finding new and interesting harmonies. Erik, move to California so we can hang out more!!

Alek Milovidov, pronounced "my lovey dove," you are the funniest guy I know, and you are way too good to me. Your intelligence and imagination never cease to challenge me and make

me a more creative person. Cheers to a future full of good movies, deal hunting, and food adventures!

I would also like to thank **Dr. Steve Klisch** at Cal Poly for inspiring my career in bioengineering. He introduced me to the fascinating world of biomechanics, and lit my passion for approaching biology using mechanical engineering principles. Steve has also been a key role model in my life. He surfs in the morning, teaches and does exciting biomechanics research during the day, and has a wonderful family he hangs out with in the evenings. I want that!

Lastly, I want to thank all my friends, who have kept me sane and shared so many good memories. I am a strong believer in working hard and playing hard, and have managed to find some pretty cool people in this world who are on the same page.

Abstract

Characterization of the Spinal Disc-Vertebra Interface and its Relation to Injury and Back Pain

by

Britta Berg-Johansen

Back pain is the most common musculoskeletal condition, affecting 80% of Americans during their lifetimes. Irregularities of the spinal disc-vertebra interface are associated with back pain and over 60% of disc herniation injuries. Despite the vulnerability of this interface, its structure and function are not well characterized. This dissertation explores the structural and biomechanical features of the disc-vertebra interface, with the goal of motivating improved diagnostics and treatments for back pain patients.

Towards this goal, this dissertation is broken into four studies. In the first, we show that bending strength and flexibility of the disc-vertebra interface in murine spines are reduced following spaceflight. This coincides with bone loss, and suggests that lowered bone density may lead to the increased risk of disc herniation seen in astronauts. This work translates to humans on Earth, suggesting that strategies that maintain bone health may help prevent disc herniation. In the second study, we identify failure mechanisms, quantify mechanical properties, and measure architectural features at the disc-vertebra interface in human cadaver spine specimens tested in tension. The majority of specimens failed at the disc-vertebra interface, as explained by a lack of structural integration observed with high-resolution microscopy. We also found that disc degeneration and lowered bone density in the vertebral endplate led to decreased interface strength. In the third study, we present a histological classification system for endplate

irregularities. During this work, we discovered a highly prevalent irregularity in which the disc separates from the vertebra at the tidemark – the mineralization front between the annulus fibrosus and calcified cartilage layer. We show that even small separations at the tidemark may be clinically relevant, as they are visible as high-intensity zones (HIZs) using MRI. In the last study, we present a novel Matlab algorithm for quantifying cartilage endplate morphology using MRI, and show that variation in endplate thickness is correlated with disc degeneration.

Collectively, the work presented in this dissertation emphasizes the vulnerability of the disc-vertebra interface and uncovers potential risk factors for injury. These findings will motivate new specialized diagnostics, preventive strategies, and treatments for many patients suffering from low back pain.

Table of Contents

List of Tables

Chapter 5

List of Figures

Chapter 1

Chapter 2

Chapter 3

Chapter 4

Chapter 5

Chapter 6

Appendices

Chapter 1: Introduction

The Burden of Low Back Pain

Low back pain is the leading cause of disability worldwide, affecting 50% of working Americans each year and 80% of the population at some point in their lives.[1,2] Back pain is the second most frequent reason for doctor visits, the fifth most frequent reason for hospital admissions, and the third most frequent reason for surgery.[3] A team of researchers at Duke found that the total health care expenditures incurred by Americans with back pain surpassed $90 billion in one year alone, with $26 billion directly attributable to treating back pain.[4]

Approximately 90% of low back pain is nonspecific, meaning the source of pain is not identifiable.[5] This lack of accurate diagnosis has major implications for treating back pain. For example, spinal fusion surgery, which costs upwards of $35,000 per patient, is often performed on patients with non-specific back pain, with outcomes no better than nonsurgical treatments.[6,7] Yet, the number of fusion surgeries is rapidly increasing, doubling between the years of 1990 and 2001.[6,7] Experts in the field have recommended that fusion surgery only be applied in carefully selected patients; however, lack of clear criteria to select these patients makes this a major challenge.[8] Given the large socioeconomic burden of back pain, the overarching importance of studies focusing on tissue sources of back pain is as follows: if we can understand the mechanisms of specific injuries, we can work to develop enhanced diagnostics and specialized treatments for back pain.

The Intervertebral Disc

The most common identifiable source of low back pain is the intervertebral disc, accounting for more than 40% of low back pain cases.[9] The intervertebral disc is composed of three main parts: the central nucleus pulposus, the surrounding annulus fibrosus, and adjacent cartilage endplates. The nucleus pulposus is a gel-like material mainly composed of water and proteoglycan and held together loosely by a network of fine type II collagen and elastin fibers. Proteoglycan aggregates possess a fixed negative charge that draws water into the disc and creates a swelling pressure to resist compressive loads.[10–12] The annulus fibrosus is a strong fibrous outer layer composed of 15-25 layers (lamellae) of collagen fibers oriented at ±30° angles with respect to the transverse plane (Figure 1).[10,12,13] These alternating angles create a structure that is both strong and flexible in the multiaxial loading conditions of the spine. Cartilage endplates are thin layers of hyaline cartilage between the disc and adjacent vertebrae that function to distribute intradiscal pressure onto the vertebrae, prevent the nucleus from bulging into the vertebrae, and allow nutrient transport between vertebral blood vessels and nucleus pulposus cells.[12,14] As a unit, the intervertebral disc acts as a shock absorber for spinal compression and allows for spinal flexibility with six degrees of freedom.

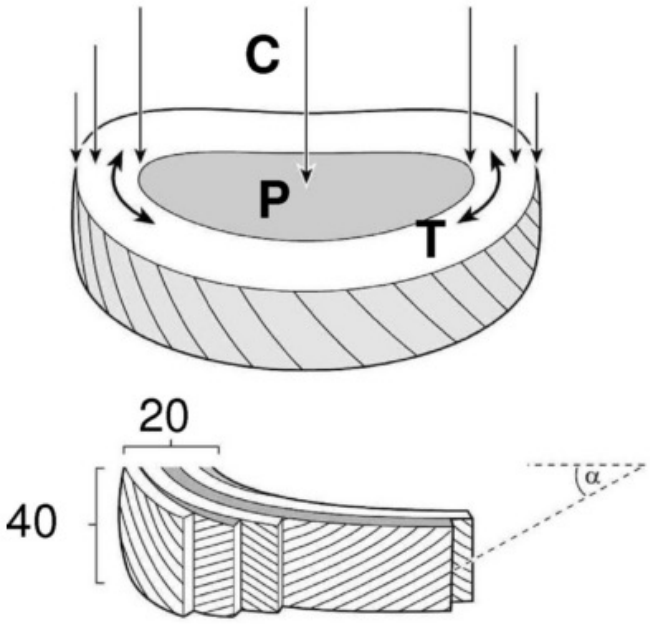

Figure 1. Intervertebral disc structure and function. (Top) Spinal compression (C) creates hydrostatic pressure (P) in nucleus pulposus and tensile stresses (T) in annulus fibrosus. (Bottom) annulus layers are oriented in alternating 30 degree angles, with ~20 collagen fiber bundles in each lamella. Image adapted from Adams et al. 2006[10]; originally published in Adams et al. 2006.[13]

The Endplate as a Source of Back Pain and Injury

Diagnosing the specific source of discogenic pain is difficult, and most diagnoses assume pain to be intrinsic to the disc. However, recent findings suggest that defects in the cartilage endplate may be a leading source of low back pain. This is supported by studies in our lab showing that regions of cartilage endplate damage are more highly innervated than regions of intact endplate (Figure 2) and than other disc tissues, therefore capable of generating pain.[14,15] Furthermore, data from imaging studies suggest that endplate damage is one of the most specific predictors of low back

pain.[14] Avulsion of the cartilage endplate from the subchondral bone (Figure 3) is a common endplate injury,[15] and the cause of over 60% of herniated disc injuries.[16]

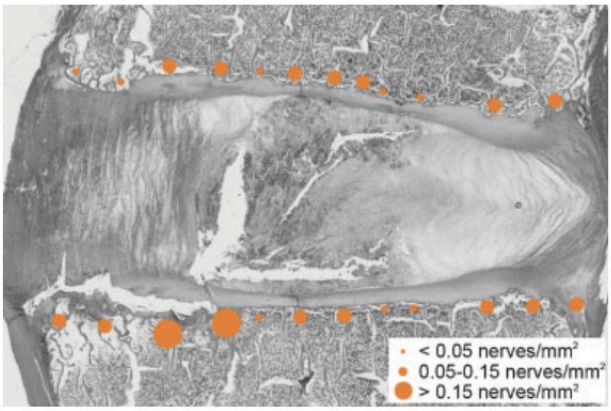

Figure 2. Distribution of nerve fibers across the endplates, showing higher nerve density in regions with endplate damage. Adapted from Lotz et al. 2013[14]

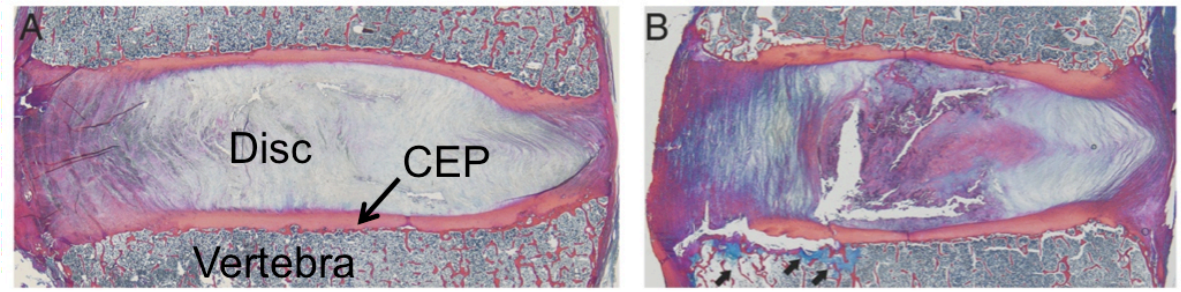

Figure 3. (A) Disc with healthy endplates, and (B) disc with inferior endplate avulsed from subchondral bone. Modified from Fields et al. 2013[17]

Various reasons may contribute to why the cartilage endplate has been vastly overlooked in back pain research and diagnostics. First, researchers are often either "disc researchers" or "bone researchers", rarely studying the entire motion segment and interactions between the disc and

vertebra. Second, the cartilage endplate is not visible using conventional magnetic resonance imaging (MRI) due to its short T_2 relaxation time, limiting the ability of clinical studies to relate endplate morphology to symptoms. However, recent studies have shown that short and ultrashort echo-time MRI sequences can be used to capture the signal of the cartilage endplate,[18–21] and will be useful for studies characterizing endplate changes and their contribution to back pain and injury.

Biomechanics of Soft-Hard Tissue Interfaces

The junction between the disc and vertebra, where the cartilage endplate lies, is biomechanically at risk because stress concentrations occur at joints and regions where material properties change abruptly. Soft-hard tissue interfaces in the body typically possess anisotropic structural properties that vary gradually from the soft to the hard tissue. This functional grading enables effective stress transfer and decreases stress concentrations at the interface.[22–24] For example, the fibrocartilaginous region between tendon and bone is graded in the degree of mineralization and in the density and organization of collagen fibers (Figure 4).[25] Soft-hard tissue interfaces also typically possess collagen fiber anchoring to enhance the integrity of attachment and arrest cracks from propagating. At the tendon-bone insertion, interdigitation creates a mechanical interlock (Figure 4). In articular cartilage, collagen fibers are oriented parallel to subchondral bone near the superficial zone to resist shear loading during articulation, but are graded through the cartilage depth and become perpendicular to the subchondral bone at the cartilage-bone interface for anchoring purposes.[26] This interface also has a calcification gradient as seen at the tendon-bone insertion.

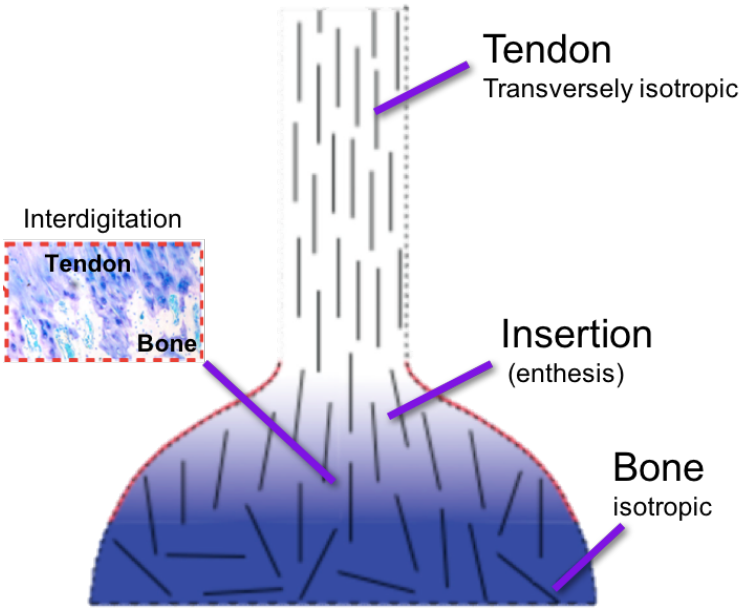

Figure 4. Tendon-to-bone insertion site. The tendon attached to bone through a tissue region that presents functional grading of mineral volume fraction (represented by shading) and collagen fiber orientation (represented by lines), as well as tissue interdigitation (dashed box). Figure adapted and modified from Liu et al. 2011.[25]

While the biomechanics of the annulus fibrosus and nucleus pulposus have been studied extensively, the biomechanics of the interface between the disc and subchondral bone are not well characterized. The cartilage endplate only covers the central region of the disc, adjacent to the inner annulus and nucleus pulposus. Recent imaging work suggests that a region of calcified cartilage exists between the endplate and subchondral bone that functions to decrease stress concentrations with a gradation of material properties.[27] The type II collagen fibers in the inner annulus may insert into this calcified cartilage zone but do not appear to insert into the subchondral bone,[27,28] indicating that the endplate-bone junction may be the structurally weakest location along the disc-vertebra interface. It has been shown that thicker endplates with a higher degree of

curvature are stronger than thin, flat endplates,[14] and thus endplate morphology may be another important structural determinant of disc-vertebra avulsion strength.

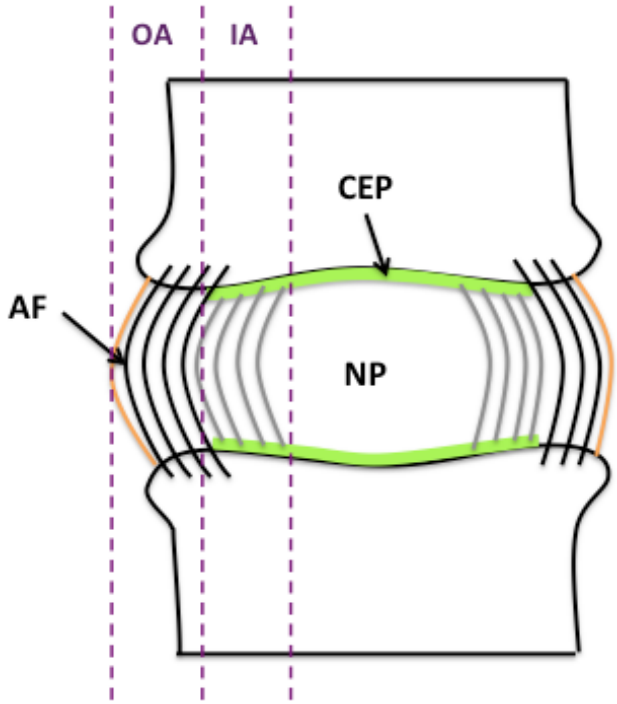

Figure 5. Structure of the intervertebral disc. CEP = cartilage endplate, NP = nucleus pulposus. OA/IA = outer/inner annulus. The CEP covers the central region of the disc and is not present around the periphery.

Despite the clinical significance of the disc-vertebra interface, its biomechanical behavior – including avulsion strength and potential risk factors for injury – is poorly understood. Understanding the specific mechanisms of endplate avulsion will motivate the development of enhanced diagnostic tools and more effective back surgeries and treatments targeted for patients with pathologic CEP tissue.

Overview of Chapters

The studies performed for this dissertation aim to better clarify the mechanics and structure of the disc-vertebra interface, and the interplay between mechanics and structure. Towards this goal, the following chapters are broken down as follows:

Chapter 2 explores the effects of spaceflight (weightlessness) on the biomechanics of mouse spines. Astronauts have a quadrupled risk of disc herniation injury, with the majority of disc herniation injuries initiating at the disc-vertebra interface. Disc herniation typically occurs during forward bending, yet the effects of spaceflight on spinal bending properties were previously unknown. Through a collaboration with the National Aeronautics and Space Administration (NASA), mice were sent to space for 30 days and, upon their return, we analyzed the bending properties of caudal motion segments and ground controls. We found that bending strength and flexibility were reduced following spaceflight, and the location of failure shifted from the disc-vertebra interface (in controls) to the growth plate and/or epiphyseal bone (in spaceflight animals). This shift in failure location coincided with bone loss, which is also observed in human astronauts. These results suggest that the bone loss and reduced flexibility may contribute to the increased herniation risk observed in astronauts, and conclusions from this study and others in our lab are being incorporated into new pre-and post-flight exercises and recommendations for NASA astronauts.

This study catalyzed my growing interest in the disc-vertebra interface and inspired the work presented in **Chapter 3**, which quantifies the structure and function and identifies failure mechanisms of the disc-vertebra interface in human cadaver spines. In this study, vertebra-disc-vertebra specimens were biomechanically tested to failure in tension, and the disc-vertebra interfaces was assessed using high resolution imaging techniques. Seventy-one percent of

specimens failed at the disc-vertebra interface between the cartilage endplate and bone. Histology and scanning electron microscopy (SEM) both indicated a lack of structural integration between the cartilage endplate and bone. Structure-function analyses showed that interface strength was higher in specimens with denser bone in the vertebral endplates and in less degenerated discs. This study's findings illuminate mechanisms of failure at this vulnerable interface and provide insight into structural features that may contribute to risk for disc-vertebra interface injury.

Throughout my studies described in Chapters 2 and 3, it became increasingly clear that the nomenclature used to describe the various endplate irregularities in the spine is incredibly varied. Studies on pathophysiology and clinical significance of specific endplate irregularities are limited by this lack of consensus on terminology. **Chapter 4** addresses this need and presents a new histological classification system for endplate irregularities. We analyzed 89 discs from 15 cadaver spines using both histology and MRI. Throughout our analysis, we identified a highly prevalent form of endplate irregularity in which the outer annulus separates from the vertebra at the tidemark. Interestingly, these "tidemark avulsions" were visible on MRI as high-intensity zones. These findings are clinically significant, and we are currently developing a histologically-driven MRI classification scheme for clinical use.

Despite the known associations between endplate irregularities and back pain and injury, the relationship between endplate morphology and disc degeneration is not well characterized, in part because the cartilage endplate is not visible using standard MRI sequences. **Chapter 5** presents a novel Matlab algorithm for measuring cartilage endplate morphology using ultrashort echo-time MRI, and correlates endplate morphology to disc degeneration. Through this study, we found that the spatial variation in endplate thickness and disc $T_{1\rho}$ were associated with

degeneration. This finding suggests that spatial variation in endplate morphology may be a useful clinical marker for back pain patients.

Chapter 2 is published as a manuscript in the *Journal of Orthopaedic Research*, and Chapter 3 is accepted as a manuscript and in press for the *Journal of Orthopaedic Research*. Chapter 4 represents a body of work that is currently being expanded upon and will be submitted as a manuscript to Spine in June 2017. Chapter 5 is a standalone manuscript, and was recently submitted and is currently in review for *Spine*.

Chapter 2: Spaceflight-induced Bone Loss Alters Failure Mode and Reduces Bending Strength in Murine Spinal Segments

The content of this chapter is published as a research article in the *Journal of Orthopaedic Research* (2015) by the following authors:

Britta Berg-Johansen[1], Ellen C. Liebenberg[1], Alfred Li[1], Brandon R. Macias[2],

Alan R. Hargens[2], Jeffrey C. Lotz[1]

[1]University of California, San Francisco; [2]University of California, San Diego

Abstract

Intervertebral disc herniation rates are quadrupled in astronauts following spaceflight. While bending motions are main contributors to herniation, the effects of microgravity on the bending properties of spinal discs are unknown. Consequently, the goal of this study was to quantify the bending properties of tail discs from mice with or without microgravity exposure. Caudal motion segments from six mice returned from a 30-day Bion M1 mission and eight vivarium controls were loaded to failure in four-point bending. After testing, specimens were processed using histology to determine the location of failure, and adjacent motion segments were scanned with micro-computed tomography to quantify bone properties. We observed that spaceflight significantly shortened the nonlinear toe region of the force-displacement curve by 32% and reduced the bending strength by 17%. Flight mouse spinal segments tended to fail within the growth plate and epiphyseal bone, while controls tended to fail at the disc-vertebra junction. Spaceflight significantly reduced vertebral bone volume fraction, bone mineral density, and trabecular thickness, which may explain the tendency of flight specimens to fail within the epiphyseal bone.

Together, these results indicate that vertebral bone loss during spaceflight may degrade disc joint bending properties and contribute to increased disc herniation risk in astronauts.

Introduction

Microgravity exposure during spaceflight negatively impacts the human spine and increases the risk for low back pain and injury. Astronauts experience a 4.3-fold increase in intervertebral disc herniation rate following spaceflight (Figure 6 & Figure 7).[29] Herniation occurs when the annulus fibrosus or CEP junction is damaged and nucleus pulposus material extrudes through the damaged region. The extruded nucleus material can press on spinal nerves, causing severe pain and often requiring surgery. Disc herniation can be mechanically induced via a combination of hyper-flexion plus compression,[30,31] making herniation likely during heavy lifting events in a flexed posture.

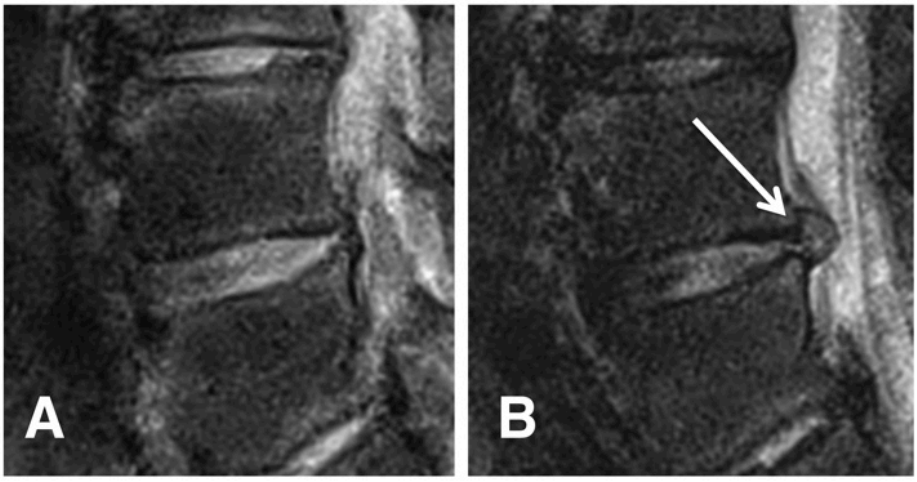

Figure 6. T2-weighted MR images of an astronaut's L4-L5 disc (A) immediately post-flight and (B) 30 days after landing, with a visible disc herniation (white arrow). Image courtesy of Dr. Alan Hargens.

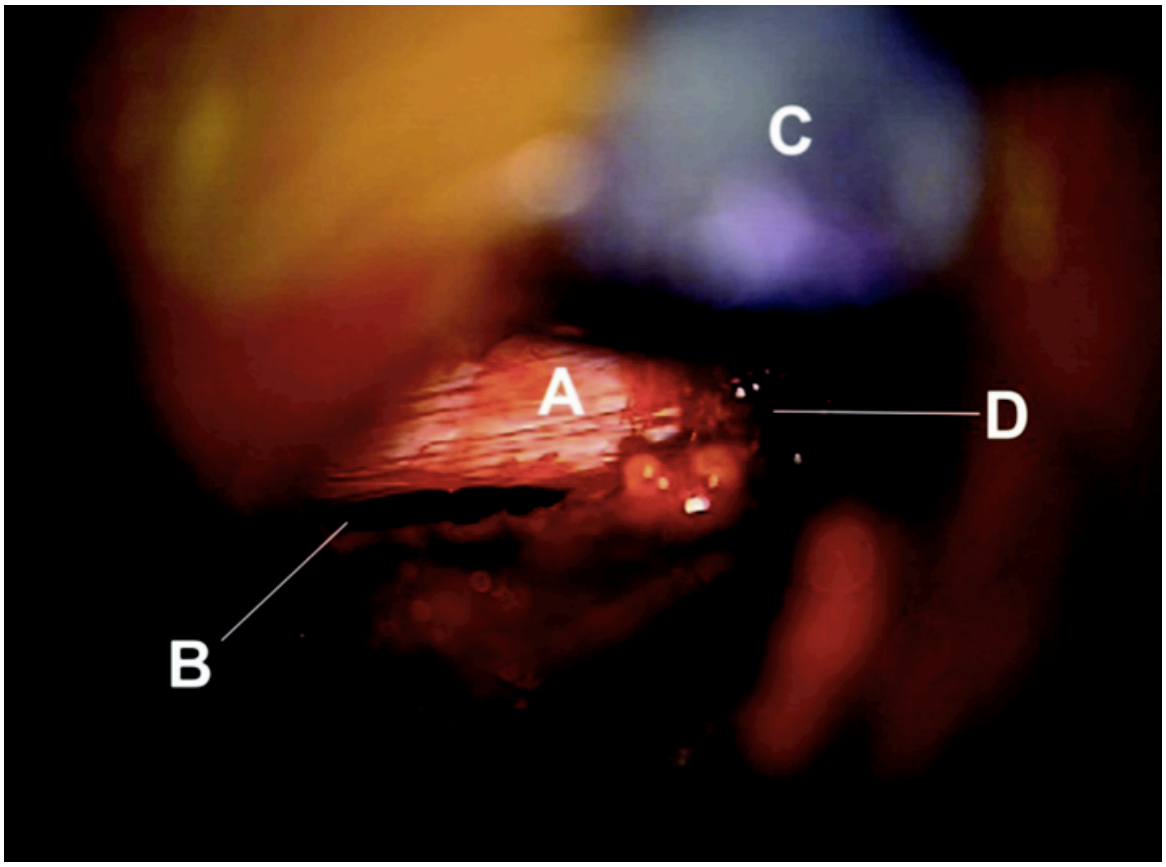

Figure 7. Astronaut disc herniation photographed during surgery showing a tear at the endplate junction (B). The annulus fibrosus (A) has been avulsed from the vertebra and the nucleus pulposus herniated through the space. (C) is a retractor retracting the ligamentum flavum, and (D) is fat tissue. Image kindly provided by the Belavy et al.[32] under the Creative Commons Attribution License.

Various phenomena may account for the increase in post-spaceflight herniation rates. Spine unloading, due to microgravity exposure, is thought to cause supraphysiologic disc swelling and hydration, as suggested by the increased spine length during spaceflight[33,34] and disc swelling observed during prolonged bed rest.[35] Disc swelling has been shown to place the annulus and intervertebral ligaments in greater tension and limit the range of motion of the spine.[36] By contrast,

gravity loading increases slack in intervertebral ligaments and reduces the disc's resistance to bending; consequently, forward bending stresses are 300% lower in the evening than in the early morning.[37] Increased tension in the annulus following prolonged unloading may also cause annular tissue degradation and negatively affect matrix production.[38] Furthermore, supraphysiologic disc swelling leads to a loss of lumbar lordosis,[39] offsetting tensile and compressive differences between the anterior and posterior annulus and increasing tension in the posterior annulus.[40,41] Together, these altered disc biomechanics associated with spaceflight may elevate an astronaut's herniation risk during flexion movements upon return to a gravitational environment.

Although imaging and biopsy studies on human astronauts have uncovered a multitude of compositional and geometric changes in the spine during spaceflight including bone loss,[42,43] muscle atrophy,[42,44] and disc heightening,[33] animal models are essential in studying changes in spinal mechanics invasively. Due to limitations of spaceflight research, very few of these animal studies have been performed, most of which use the rodent caudal disc model. For example, Bailey and coworkers observed that uniaxial compressive creep properties decrease in murine caudal discs post-spaceflight[45] and do not recover significantly over 7-day re-acclimation to gravity.[46] However, Sinha and coworkers found that neonatal rats exposed to a relatively short 5-day spaceflight do not demonstrate significant alterations in vertebral compressive strength or disc resiliency as determined by stress-relaxation.[47] No studies to date have measured changes in mechanical bending properties of the spine following spaceflight.

Given the importance of bending motions for herniation induction, we hypothesized that the biomechanical bending properties of mouse spines following spaceflight are diminished as compared to ground controls. Additionally, we hypothesized that the main site of disc failure is

the annular insertion to the vertebra, based on recent work showing this junction to be the most common site of failure in clinical lumbar disc herniations.[16]

Materials and Methods

Animals

This study was approved by the NASA Ames Research Center Institutional Animal Care and Use Committee (IACUC). Fourteen male C57BL/6 mice (19-20 wks old) were obtained through NASA's Biospecimen Sharing Program (BSP). Six mice had flown in low Earth orbit on a 30-day microgravity Bion M1 mission and were sacrificed 13-15 hours after landing. This 13-15 hour time period was required to perform initial health inspections and to transport animals from their landing site in the Orenburg region of Russia to the dissection site in Moscow. Eight control mice were kept on the ground during the same 30-day period in standard vivarium cages (GM 500, Techniplast). BSP personnel sacrificed mice and dissected and flash froze tissues. We received isolated frozen tails from the post-flight mice (flight, n=6) and vivarium controls (control, n=8).

Specimen Preparation

The C3-C4 caudal motion segment was isolated from each specimen and thawed. The ventral side of each motion segment was marked with tissue dye to track orientation. Surrounding ligaments and soft tissues were removed to isolate the discs and vertebrae, and x-ray scans were obtained for each specimen to measure disc height as an average of three measurements taken at the center of the disc. Specimens were kept hydrated with phosphate buffered saline (PBS) throughout tissue preparation.

Mechanical Bending Tests

Each motion segment was placed in a custom 3D-printed four-point bending device such that the plane of bending coincided with the ventral-dorsal plane (Figure 8). Four 25-gauge stainless steel needles were inserted through the top and bottom parts of the device, perpendicular to the plane of bending, to create the four contact points. The four needles were allowed to rotate freely within the holes so as to minimize longitudinal shear forces. Beam deflection calculations confirmed a negligible (<10 μm) maximum deflection of the needles during the bending tests, and x-rays taken at incremental bending displacements confirmed no bone-on-bone contact. The lower supports of the bending system were spaced 7.5 mm apart, while the upper supports were spaced 2.5 mm apart and attached to the moving cross-head of a materials test system (ElectroForce 3200; Bose, Eden Prairie, MN). Each specimen was carefully placed onto the lower supports and the lower stage was raised until the specimen was just touching the upper supports, as indicated by a load of 0.1 N. Specimens were preconditioned by ramping between 0 and 0.5 mm at a rate of 0.05 mm/sec for 5 cycles in order to create a uniform strain history and allow specimens to stabilize on the supports. Then, samples were loaded to failure under a displacement controlled protocol at a rate of 0.006 mm/sec. Ramping was terminated after failure, which was defined as a drop in force by 1.5 N.

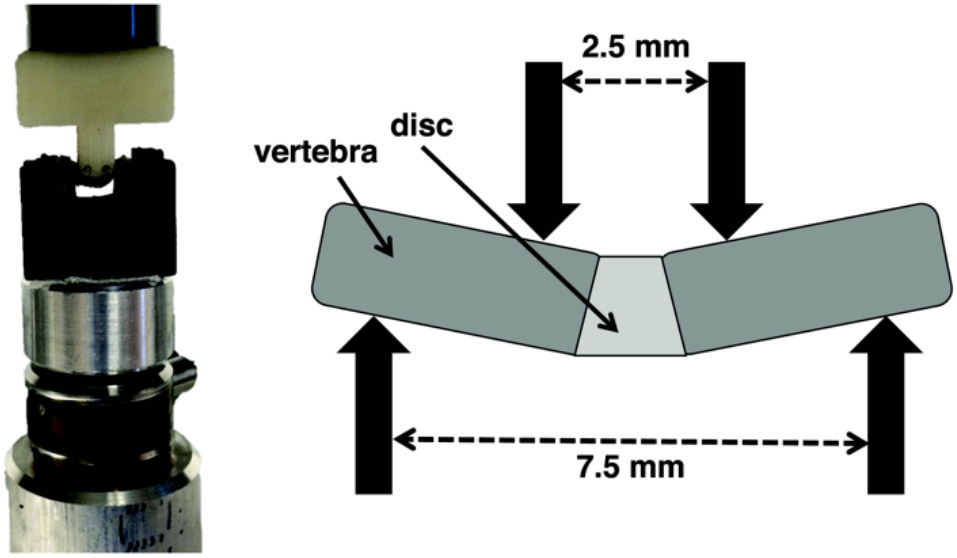

Figure 8. Mechanical testing 4-point bending setup (left) and spacing of bending supports (right)

From force-displacement data, the toe region was defined as the displacement corresponding to an applied force of 1 N. This nonlinear toe region has been reported for various annulus fibrosus mechanical studies.[48,49] As is generally accepted for aligned collagenous tissues, the nonlinearity in the toe region results from viscoelastic straightening and recruitment of initially lax annulus collagen fibers, and is thus indirectly related to the flexion range of motion of the disc. The bending stiffness was defined as the slope of the most linear region, and the bending strength was defined as the maximum load before failure (Figure 9). Data from the 5 preconditioning cycles was used to calculate the maximum load reached during preconditioning. Following mechanical testing, specimens were wrapped in PBS-soaked gauze and frozen.

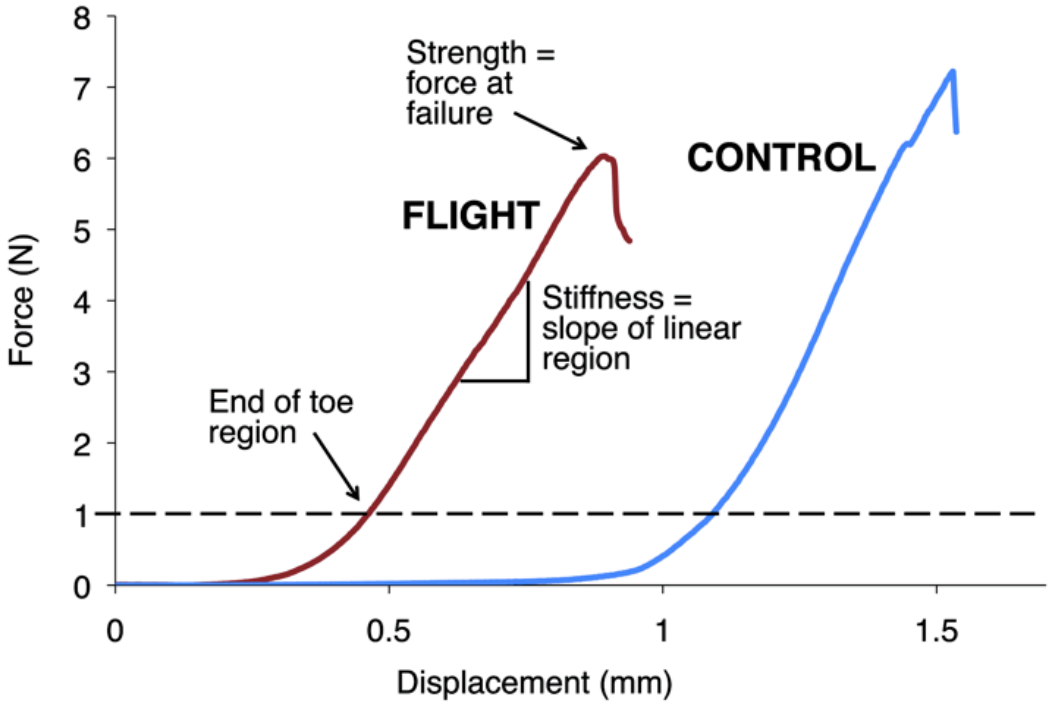

Figure 9. Representative load-displacement curves for flight and control mice. Toe region displacement and force at failure are decreased for flight mice, while stiffness (slope of linear region) remains relatively constant.

Histology

Failed motion segments (n=5 control, n=3 flight) were processed for histology. The decreased sample sizes for histology analyses were the result of preparing the remaining specimens for MRI scans that proved inconclusive. Specimens were fit into histology molds to maintain their bent position and fixed in formalin. Specimens were then decalcified with a mild ion-exchange agent (Biocare Medical; Concord, CA), embedded in paraffin, and cut into 7-μm thick sections. Sections from various equally-spaced locations throughout each specimen were stained with a tri-chrome Mallory-Heidenhain connective tissue stain that contains aniline blue (collagen stain), orange G (erythrocyte stain), and acid fuchsin (plasma stain), and analyzed for failure location. Polarized

light was used to visualize collagen fibers near failure locations.

Residual sections were stained with Safranin O. The intensity of Safranin O staining is directly proportional to the proteoglycan content in cartilage; thus, this method was used to assess relative proteoglycan contents in the growth plates of flight vs. control spinal segments. Growth plate thickness was quantified using an automated custom MATLAB segmentation script that segments and thresholds the growth plates.

Micro-Computed Tomography (*μ*CT)

Indication of post-flight vertebral rim fractures noted by histology prompted a μCT bone analysis. Adjacent whole motion segments were scanned using high-resolution X-ray microscopy to quantify bone mineral density and trabecular microarchitecture (μCT 50, SCANCO Medical, Brüttisellen, Switzerland). Motion segments were oriented with the longitudinal axis of the spine perpendicular to the radiation beam and scanned in 70% ethanol at a 4μm voxel size using a tube voltage of 55 kVp and an X-ray intensity of 109 μA.

Image reconstruction was performed using SCANCO software and scans were analyzed using SCANCO Evaluation Program v6.5-3 to quantify bone volume fraction (BV/TV), bone mineral density (BMD), and trabecular microarchitecture (trabecular number, thickness, and spacing) on each whole motion segment. Subsequently, these same analyses were performed on a trabecular compartment of bone in the metaphysis adjacent to the cranial growth plate of each vertebra to quantify changes in parameters specific to the trabecular bone. This trabecular volume of interest (VOI) was manually delineated using an irregular contour drawn a few pixels away from the endocortical surface. The VOI began just below the growth plate on the cranial end of the vertebra and extended 1mm (250 slices) towards the diaphysis (Figure 10). This VOI was

chosen rather than isolated epiphyses because murine epiphyses are very small (~0.7-0.8 mm^3) and composed largely of cortical bone, which remodels slower than trabecular bone.[50,51] The chosen VOI had a larger trabecular volume which improved our statistical power for identifying bone density changes induced by spaceflight.

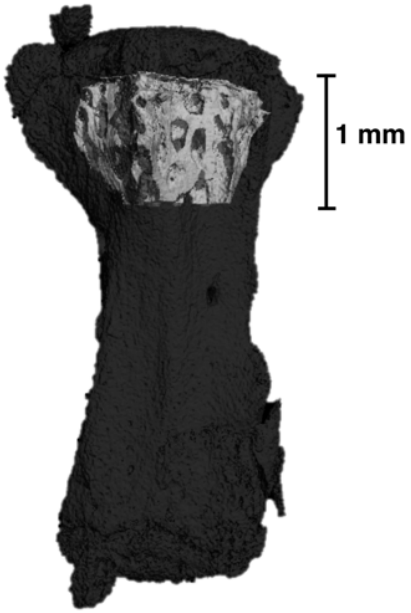

Figure 10. Representative *μ*CT scan showing the volume of interest used for analysis (light gray) highlighted within the entire vertebra (dark gray). Note the volume of interest only includes the trabecular core.

For all analyses, a lower threshold of 300 grayscale units was used to segregate mineralized tissue from soft tissue and scan medium, and Gaussian filters with a sigma of 0.5 and support of 2 were applied to remove noise. Morphometric indices were calculated using a 3D model-independent algorithm, and BMD was calculated using a linear attenuation coefficient determined by calibration with a SCANCO hydroxyapatite phantom.

Statistical Analyses

All statistical analyses were performed using R (R Foundation for Statistical Computing, Auckland, New Zealand). Unpaired two-tailed t-tests were used to assess differences in bending strength, toe region length, displacement at failure, and disc height between control and flight groups. Unpaired one-tailed t-tests were used to assess differences in bone parameters from micro-computed tomography scans by testing the alternate hypothesis that bone loss occurs in microgravity. One-tailed t-tests were appropriate due to bodies of research showing bone loss occurs in both rodents and humans in microgravity conditions.[52–55] Univariate linear regression analysis was performed to assess correlations between mechanical bending properties and bone properties, and two-tailed t-tests were used to determine whether regression slopes were significantly different than zero. Significance for all statistical tests was defined by $p < 0.05$, while trends were defined as $0.05 < p < 0.1$.

Results

Mechanical Bending Properties

Spaceflight reduced bending strength by 17% relative to controls (6.27 ± 0.94 vs. 7.53 ± 1.13 N, $p < 0.05$), shortened the toe region by 32% (0.53 ± 0.13 vs. 0.77 ± 0.21 mm, $p < 0.05$), and tended to reduce displacement at failure (1.01 ± 0.22 vs. 1.35 ± 0.40 mm, $p = 0.07$), with no significant effect on bending stiffness ($p > 0.25$; Figure 9 & Figure 11). The maximum load reached during preconditioning was 4X higher in flight mice (2.14 ± 1.42 N vs 0.40 N ± 0.33 N, $p < 0.05$). Disc height was reduced by 16% in flight mice (0.25 ± 0.03 vs. 0.29 ± 0.04 mm, $p < 0.05$).

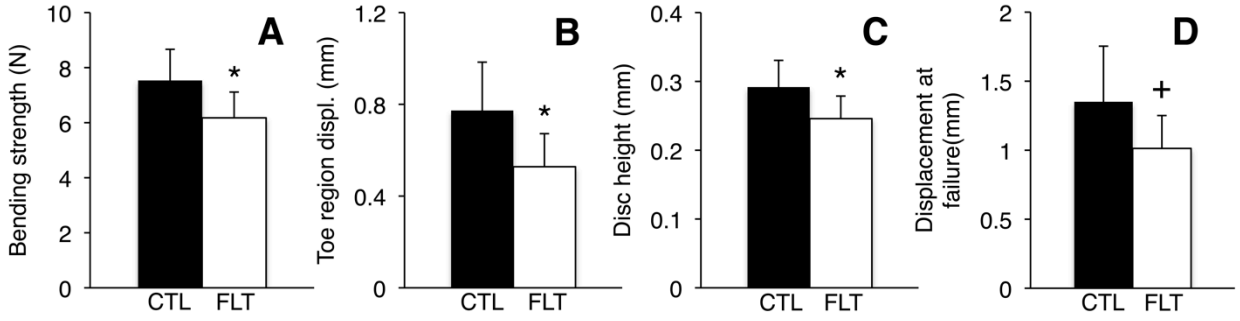

Figure 11. Bending strength, toe region, disc height and displacement at failure are all reduced for flight mice (FLT, n = 6) compared to controls (CTL, n = 8). *p < 0.05, +0.05 < p < 0.1, unpaired t-tests. Error bars represent standard deviation.

Histology

The two failure modes identified by histology were: (1) annulus avulsion at the disc-vertebra endplate junction, and (2) separation within the growth plate (Figure 12). All specimens that failed within the growth plate also underwent fractures in the trabecular bone of the epiphysis adjacent to the failed growth plate. Four of the five control spinal segments failed at the disc-vertebra endplate junction while two of the three post-flight spinal segments failed within the growth plate and epiphyseal bone. Specimens did not preferentially fail at the cranial or caudal ends of the discs. No significant changes in growth plate thickness or proteoglycan content were identified.

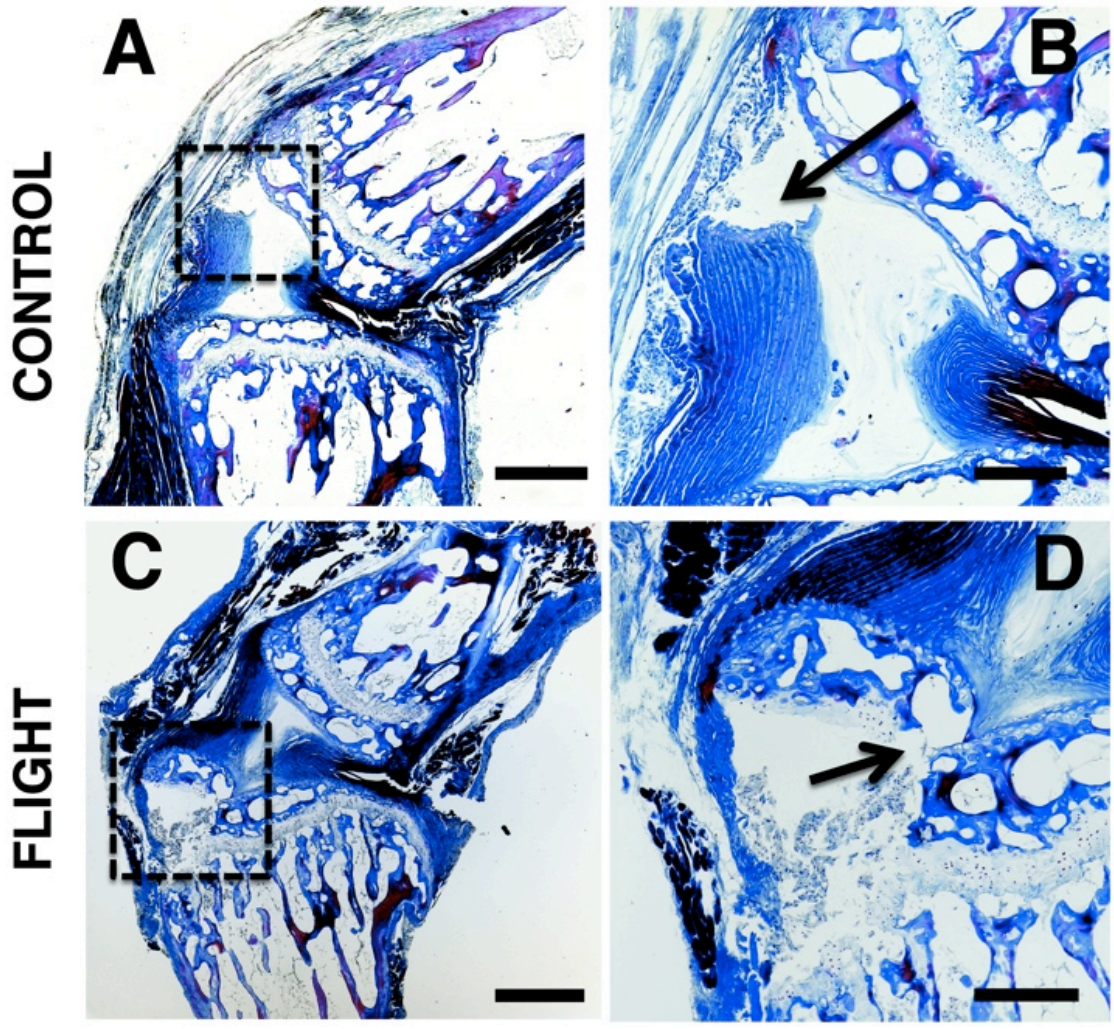

Figure 12. Representative histology images showing (A, B) failure at the endplate junction in control spinal segments and (C, D) failure in the growth plate and epiphyseal bone in post-flight spinal segments. (A and C) show the failure locations in the regions bounded by the dashed boxes and (B and D) show the failure locations indicated by arrows. Image parameters: (A, C) 4X magnification (scale bars: 500 μm); (B, D) 10X magnification (scale bars: 200 μm). These sections were stained with a tri-chrome Mallory-Heidenhain stain.

Micro-Computed Tomography

μCT analysis on the trabecular VOI adjacent to the cranial growth plate identified significant post-flight decreases in bone parameters (Figure 13 and Figure 14). Spaceflight reduced BV/TV by 20% ($p < 0.05$), reduced BMD by 18% ($p < 0.05$), and – most significantly – reduced trabecular thickness by 14% ($p = 0.001$). Spaceflight had no statistically significant effect on trabecular number or trabecular spacing ($p > 0.1$). Linear regression analyses indicated positive relationships between bending properties and bone quality (Figure 15). For example, displacement at failure increased with BV/TV ($R^2 = 0.48$, $p = 0.05$) and with BMD ($R^2 = 0.45$, $p = 0.07$). Toe region displacement increased with trabecular thickness ($R^2 = 0.40$, $p = 0.09$). Bending strength also showed a weak positive correlation with BMD ($R^2 = 0.24$, $p = 0.22$). Regression analyses between bone density and trabecular microarchitecture showed that BMD increased significantly with trabecular thickness ($R^2 = 0.66$, $p < 0.05$). BMD also increased significantly with trabecular number ($R^2 = 0.72$, $p < 0.05$) and – because trabecular number and trabecular spacing are so strongly correlated ($R^2 = 0.99$, $p < 5.0e\text{-}7$) – decreased significantly with trabecular spacing ($R^2 = 0.70$, $p < 0.05$).

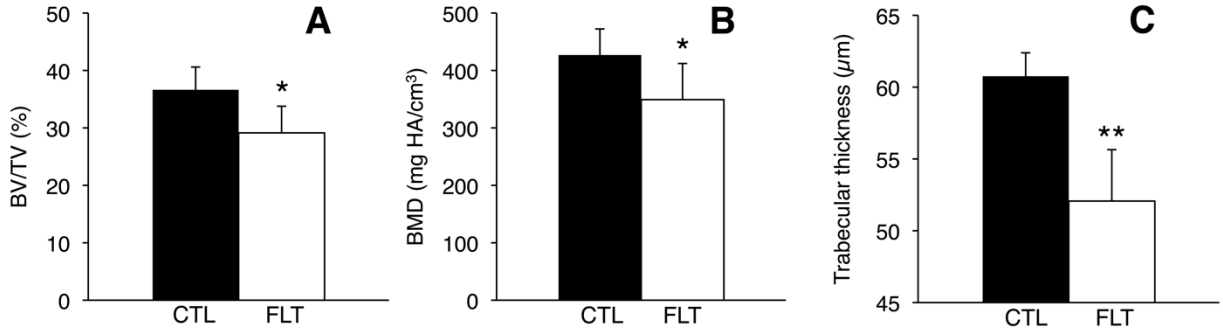

Figure 13. Bone parameters for trabecular bone VOI adjacent to growth plate in control (CTL, n = 5) and flight (FLT, n = 3) specimens. (A) Trabecular bone volume fraction, (B)

trabecular thickness, and (C) bone mineral density all decreased post-spaceflight. *p < 0.05, **p < 0.005, unpaired t-tests. Error bars represent standard deviation.

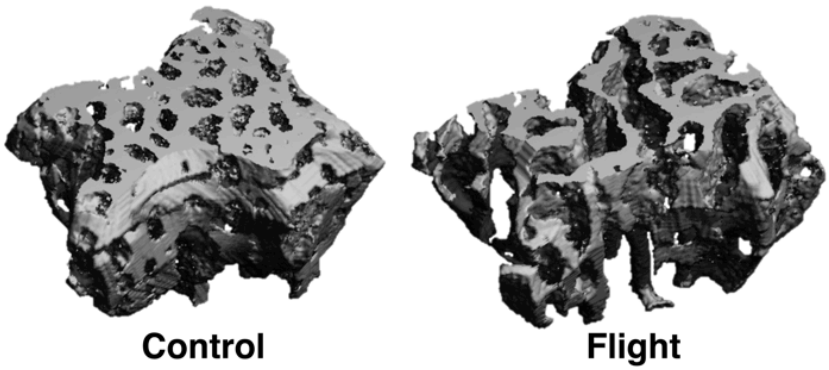

Figure 14. Representative μCT scans of trabecular volume of interest for control and flight mice. Flight specimens show significant bone loss compared to pre-flight controls.

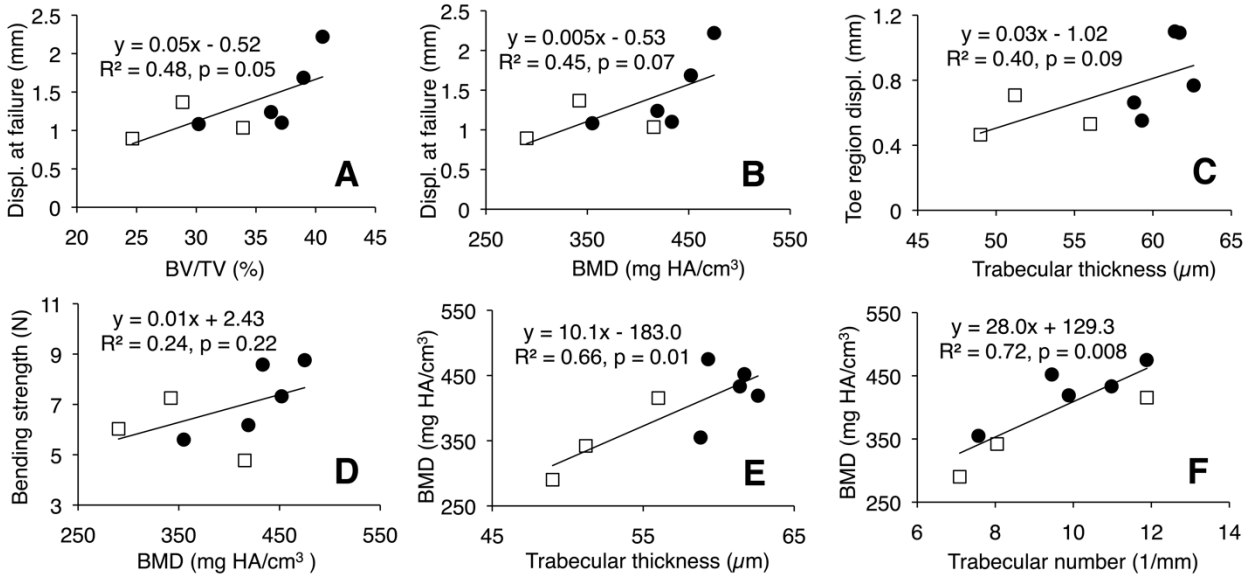

Figure 15. Regression between mechanical properties and bone properties for trabecular bone volume of interest. White squares represent flight specimens and dark circles represent

controls. Displacement at failure increased with (A) trabecular bone volume fraction and (B) bone mineral density. (C) Toe region displacement increased with trabecular thickness and (D) bending strength increased with bone mineral density as trends. Bone mineral density significantly increased with (E) trabecular thickness and (F) trabecular number.

Analysis of entire vertebrae indicated a significant 9% decrease in trabecular thickness ($p = 0.0008$; Figure 16A), but no significant differences in BV/TV or BMD ($p > 0.1$). Toe region displacement increased significantly with trabecular thickness ($R^2 = 0.53$, $p < 0.05$; Figure 16B), with no other significant correlations found between mechanical properties and bone microarchitecture. BMD was not correlated with trabecular thickness for the entire vertebrae; however, BMD once again increased with trabecular number ($R^2 = 0.67$, $p < 0.05$; Figure 16C) and decreased with trabecular spacing ($R^2 = 0.59$, $p < 0.05$).

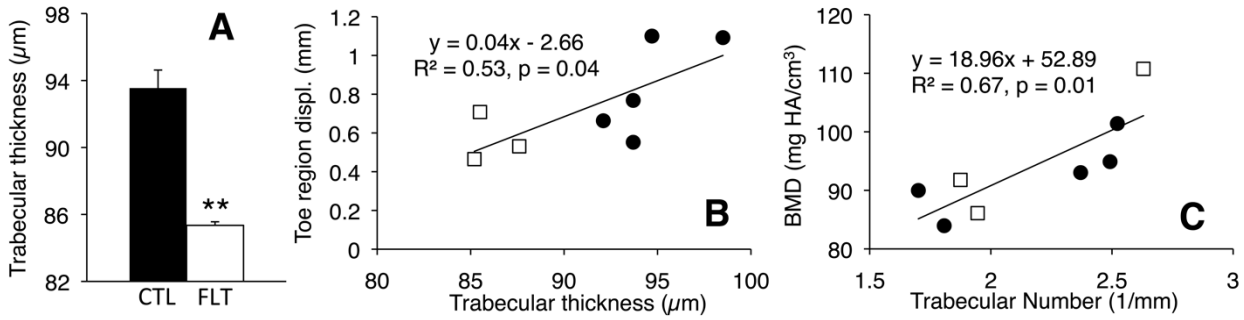

Figure 16. (A) Trabecular thickness for entire vertebra μCT analysis, showing large decrease post-flight (p < 0.001, unpaired t-test); (B&C) Regression between (B) toe displacement and trabecular thickness, and (C) BMD and trabecular number for entire vertebra analysis, showing significant positive correlations. White squares represent flight specimens and dark circles represent controls.**

Discussion

The results of this study demonstrate that spaceflight reduces the bending properties of spinal segments. The 17% reduction in bending strength may be an important factor for explaining the increased herniation risk in astronauts post-spaceflight, and the 32% reduction in toe region – in conjunction with the 25% reduction in displacement at failure – is consistent with reports of decreased range of motion following bed rest.[37,56] The shortened toe region indicates that post-flight specimens built up force more rapidly, causing a leftward shift of the force-displacement curve and a decreased displacement at failure (Figure 9). Post-flight specimens also reached a 441% higher load during preconditioning, providing further evidence of rapid force build-up and decreased flexibility. Although contradictory to the spine lengthening observed in human astronauts,[33,34] the disc height shortening we observed is consistent with other microgravity studies conducted by Bailey and coworkers using the murine caudal disc model.[45,46] Murine caudal discs may not experience the same amount of daily loading as human discs, and thus the change in load in microgravity conditions may not be great enough to cause as much disc swelling as in humans.

We were able to visualize the failure location in all seven specimens analyzed histologically. It is well known that physical properties of the annulus are rate dependent, and thus the failure location may change with different loading rates, as observed in ligament-bone complexes.[57] However, strain rate was held constant and thus did not contribute to changes in failure location among specimens. All specimens failed near the disc-bone interface, presumably due to complicated stress fields and stress concentrations at this junction of dissimilar materials. Control specimens tended to fail at the CEP junction, which is known to be a source of weakness and the most common location of failure causing disc herniation in humans.[16] Endplate junction failure has also been observed in astronaut disc herniations[32] (Figure 7). The weakness of the

endplate junction may be due to an apparent lack of structural attachment (i.e. collagen fibers) between the CEP and subchondral bone.[12,28,58,59] Interestingly, the post-flight specimens did not tend to fail at the endplate junction; rather, these specimens showed tears in the growth plate as well as trabecular fractures in the epiphyseal bone adjacent to the growth plate. This suggests one of two possible failure mechanisms: (1) mechanical bending tore the growth plate, allowing rapid hyper-flexion that induced bony fractures, or (2) mechanical bending fractured the epiphyseal bone, allowing a fragment of bone to tear away with the annulus fibrosus, bringing along an adjacent fragment of growth plate tissue. Mechanism (1) suggests a decrease in growth plate integrity following exposure to microgravity, while mechanism (2) suggests bone loss or weakening. Alternatively, growth plate and bone weakening may both occur. The observed shift in failure location for flight mice may explain the reduction in bending strength without a corresponding reduction in bending stiffness.

The μCT results support bone weakening as the cause for failure mechanism differences observe between flight and control mice. For the trabecular VOI adjacent to the growth plate, we found that spaceflight significantly reduced BV/TV, BMD, and trabecular thickness. The 18% reduction in BMD we measured is comparable to the 7-15% reductions in BMD reported for rat tibias subjected to 23-30 days of hindlimb unloading.[60,61] The most significantly reduced parameter in this study was trabecular thickness, which decreased by 14% for the trabecular VOI ($p = 0.001$) and 9% for the entire vertebra ($p = 0.0007$), and is consistent with reports of decreased trabecular thickness in hindlimb unloading models of the rat tibia.[61] This thinning of trabeculae may help explain the fractures of individual trabeculae that we observed in failed post-flight specimens (Figure 11D). The increased significance of trabecular thinning when analyzing the entire vertebra is likely attributed to error reduction over a larger region of bone, as supported by smaller standard

deviations. The lack of significant changes in other bone parameters that are not specific to the trabeculae when analyzing the entire vertebra may be explained by the higher amount of bone turnover in trabecular than cortical bone.[50,51] In agreement with this, astronauts experience greater levels of bone loss in trabecular than cortical bone.[52] Our findings of bone loss following spaceflight agree with various rodent studies showing decreased trabecular bone volume fraction and decreased bone formation resulting in a relative osteopenia following spaceflight.[53–55] Bone formation can be inhibited within less than a week of spaceflight, and is correlated with decreased mRNA levels for bone matrix proteins.[62,63] Overall, the bone loss following spaceflight we report may explain the tendency of flight mice to fail within the growth plate and bone, as compared to at the endplate junction as seen in controls.

We identified various trends between bone parameters and mechanical bending properties. For the trabecular VOI, displacement at failure increased with BV/TV and BMD, and bending strength weakly increased with BMD, indicating that BMD may be a reasonably good predictor of failure risk in bending. For both the trabecular VOI and the entire vertebra, toe region displacement positively correlated with trabecular thickness. This finding is intriguing, because it implies that disc quality (as indicated by toe region displacement) may be related to bone quality (as indicated by trabecular thickness). One possible explanation is that bone loss affects stress distributions in the disc and leads to regions of high stress. This is supported by a cadaver study showing that even minor compressive damage to a lumbar vertebra caused large changes in the internal stress distribution of adjacent discs and generated peaks of compressive stress in the annulus during complex loading.[64] The reverse is also true: another cadaver study showed that forces on the vertebral body in motion segments with healthy discs were always distributed evenly, while forces on the vertebral body in motion segments with severely degenerated discs were concentrated

anteriorly in forward bending and posteriorly in an erect posture.[65] Therefore, any disc degeneration that occurs in microgravity may increase the likelihood of vertebral fracture.

The observed correlations between bone parameters and mechanical bending properties suggest that poor bone quality may contribute to herniation risk – a finding that would have major implications for treating and preventing clinical disc herniation injuries. Failure at the endplate junction, which accounts for 65% of clinical disc herniation injuries,[16] may be caused by poor structural attachment between the disc and vertebra due to poor bone quality. This idea is supported by the observation that relatively healthy discs are more susceptible to herniation-type injuries than severely degenerated discs,[30,31] indicating that the weak link may be within the vertebra. Furthermore, people with low bone density have larger discs,[66] presumably because decreased bone strength allows the discs to expand past normal limits. Increased disc size in osteoporotic patients may lead to increased risk for herniation by the same mechanism as disc swelling during spaceflight. Future studies should investigate the relationship between bone quality and disc herniation in human motion segments.

Despite its novel and intriguing results, this study has various limitations. An inherent limitation of animal models used in spaceflight missions is the lack of clarity on whether post-flight changes are caused by the same mechanisms as in human astronauts despite anatomical and physiological differences. The orientation of the spine in bipedal versus quadrupedal animals may affect the loading on the spine and – in turn – affect the differences in loading observed in microgravity conditions. However, it is thought that quadrupedal animals may have comparable spinal compression due to periodic upright posture as well as muscle contraction and ligament tension required to support the spine's horizontal alignment.[67] Swelling pressure in bovine discs is similar to human lumbar discs (typically ranging from ~0.1 – 2.0 MPa),[68–70] indicating similar-

magnitude compressive loading. Furthermore, the average compressive and torsional stiffness values of human discs (3-9 MPa and 2-9 MPa, respectively) are similar to those of mouse discs (2-4 MPa and 5-11 MPa, respectively).[71] Due to tissue availability constraints, we only obtained tails and were therefore unable to test lumbar motion segments. Tails of mice may experience less loading from muscles and passive structures. Additionally, while murine caudal discs have a similar average aspect ratio (height/diameter) to human lumbar discs (0.23 vs. 0.24, respectively),[67,71] caudal motion segments have a more circular geometry with no posterior elements, which may affect loading. However, *in vivo* rodent tail force data are lacking. Furthermore, flexion range of motion in the lumbar spine is more constrained due to posterior elements and postural musculature, and thus the bending strength of lumbar segments may be less influenced by microgravity. This would fit with reports of increased propensity for astronaut discs to herniate in the cervical spine, which undergoes larger flexion displacements, vs. the lumbar spine.[29] However, additional studies are needed for clarification.

Aside from geometric differences, rodents differ from humans in that they do not express matrix metalloproteinase-1,[67] which is thought to be involved in bone remodeling and may have differential effects on the amount of bone loss in space. In addition, rodents retain open epiphyseal growth plates throughout their adult lives, which limits our ability to compare rodent growth plate fractures to adult human discs with fused growth plates. Mouse discs also retain notochordal cells in the nucleus throughout life, which may affect swelling and viscoelastic properties and, in turn, cause rodent discs to respond differently to mechanical loading than those of humans.[67] Lastly, mice are observed to use their tails intermittently to move about inflight enclosures during spaceflight,[45] which in theory may *overload* the tails and accelerate disc degeneration. However, the post-flight bone loss observed in this study indicates that the underloading effect of

microgravity outweighs any periodic overloading. A detailed analysis of tail movement during spaceflight and/or inflight force data (measured *in vivo* or at the walls of the enclosures) would be needed to assess the degree of periodic overloading.

It should also be noted that the study design made it necessary to impose two freeze/thaw cycles (one after dissection on landing day and one after mechanical testing) that made it unfeasible to extract reliable biochemical and genetic information from the growth plate and disc. The specimens also re-acclimated to 1-G for 13-15 hours before being sacrificed, during which the biochemical properties may be affected by re-loading. However, the mechanical properties measured in this study were likely unaffected by the re-acclimation or freeze-thaw cycles, as supported by prior work showing that (1) diminished compressive properties of murine discs during spaceflight do not recover over a 7-day post-flight period,[44] and (2) frozen storage has little to no effect on the elastic response of porcine or human discs,[72–74] compressive creep properties of human discs,[75] or flexion/extension rigidity of sheep discs.[76] Therefore, we are fairly confident that the present mechanical and structure findings are primarily reflective of spaceflight effects and not the reloading phase. It should also be noted that the mechanical testing and μCT analyses were performed on two separate levels of the spine due to study limitations, and that if this had not been the case, correlations between bending properties and bone properties would likely increase in significance. Lastly, the relatively small sample size of mice onboard the Bion M1 mission – and the further reduced sample sizes for histology and μCT due to study constraints – limited the strength of our observations. A post-hoc power analysis indicated that n=14 specimens per group would be necessary to detect a statistically significant difference in failure displacement ($p < 0.05$ with 80% power). For correlations, we pooled data from both groups to increase the spread and observe overall relationships between bone quality and mechanical properties. While correlations

within each experimental group were not significant due to the small sample size, the pooled data indicated overall structure-function trends, some of which were significant and some of which neared significance. Power analysis for correlation coefficients indicated that n=14 total specimens would be necessary to detect a significant correlation between toe displacement and trabecular thickness, while n=11 specimens would be necessary to detect a significant correlation between failure displacement and BV/TV.

Despite these limitations, this study provides the first analysis of bending properties of intervertebral discs following spaceflight. This study also presents the first measurements of trabecular thickness, spacing, and number in the mouse spine following spaceflight. Our findings have various clinical implications. First, control specimens failed at the endplate junction, which is the most common source of failure in human disc herniation injuries;[16,77] thus, our results for the control specimens in this study may provide insight into general disc herniation mechanisms. The decrease in bending strength following microgravity also supports the idea that herniation risk may be higher in the morning when the discs are most swelled,[37] suggesting that flexion activities should be limited in the early morning. Additionally, the post-flight growth plate separations we observed in the post-flight mice may provide insight into mechanisms of growth plate fractures in children, which account for 30% of long bone fractures in children prior to growth plate closure.[78] Lastly, as previously mentioned, the correlations we observed between bone properties and mechanical bending properties suggest that clinical risk for herniation injuries may be related to bone quality.

Altogether, this study's findings demonstrate that the observed post-flight increase in herniation risk in astronauts may be a result of decreased mechanical bending strength in the disc-vertebra complex. The vertebral bone loss observed in this study may be relevant to astronaut disc

herniation by affecting the structural attachment between the disc and bone (Figure 7). Furthermore, as previously mentioned, bone health affects disc loading distribution,[64] and thus astronaut bone loss may negatively affect disc mechanics. These observations motivate development of countermeasures related to monitoring and preventing bone loss during spaceflight and limiting bending movements upon return to Earth. Future studies should determine the time course of bending strength recovery upon return to Earth to improve rehabilitation recommendations.

Acknowledgements

This work was supported by NASA grants NNX09AP11G, NNX13AM89G, and NNX14AP25G, as well as NSBRI grant NCC 9-58 and an NSF Graduate Research Fellowship. We would like to acknowledge the Russian Federal Space Agency for flying the Bion M1 mission, as well as the staff of the M.V. Lomonosov Moscow State University Institute of Mitoengineering for providing animal facilities. μCT imaging was performed at the Bone Imaging Research Core of the Endocrine Research Unit at the UCSF-affiliated Veterans Affairs Medical Center. We would also like to thank Aaron Fields and Jeannie Bailey for contributing helpful advice for this study. None of the authors have affiliations that are perceived to have biased the presentation.

Chapter 3: Structure-Function Relationships at the Human Spinal Disc-Vertebra Interface

The content of this chapter is accepted as a manuscript and in press for the *Journal of Orthopaedic Research* by the following authors:

Britta Berg-Johansen, Aaron J. Fields, Ellen C. Liebenberg, Alfred Li, Jeffrey C. Lotz

University of California, San Francisco

Abstract

Damage at the intervertebral disc-vertebra interface associates with back pain and disc herniation. However, the structural and biomechanical properties of the disc-vertebra interface remain underexplored. We sought to measure mechanical properties and failure mechanisms, quantify architectural features, and assess structure-function relationships at this vulnerable location. Vertebra-disc-vertebra specimens from human cadaver thoracic spines were scanned with micro-computed tomography (μCT), surface speckle-coated, and loaded to failure in uniaxial tension. Digital image correlation (DIC) was used to calculate local surface strains. Failure surfaces were scanned using scanning electron microscopy (SEM), and adjacent sagittal slices were analyzed with histology and SEM. Seventy-one percent of specimens failed initially at the cartilage endplate-bone interface of the inner annulus region. Histology and SEM both indicated a lack of structural integration between the cartilage endplate and bone. The interface failure strength was increased in samples with higher trabecular bone volume fraction in the vertebral endplates. Furthermore, failure strength decreased with degeneration, and in discs with thicker cartilage endplates. Our findings indicate that poor structural connectivity between the cartilage endplate

and vertebra may explain the structural weakness at this region, and provide insight into structural features that may contribute to risk for disc-vertebra interface injury. **Statement of clinical significance:** The disc-vertebra interface is the site of failure in the majority of herniation injuries. Here we show new structure-function relationships at this interface that may motivate the development of diagnostics, prevention strategies, and treatments to improve the prognosis for many low back pain patients with disc-vertebra interface injuries.

Keywords: Intervertebral disc, cartilage endplate junction, disc herniation, collagen, avulsion

Introduction

The intervertebral disc-vertebra interface is structurally complex as it serves as the junction for multiple tissue types (Figure 17A). Injury at this site has received growing interest due to its clinical significance. For instance, avulsion of the cartilage endplate (CEP) from bone at the cartilage-vertebral endplate junction (EPJ) may be the most common form of disc injury since it is reportedly the initial site of failure in over 60% of intervertebral disc herniations[16,77] (Figure 17B). Damage at the disc-vertebra interface is highly innervated[15] and is a specific imaging predictor of low back pain.[79] The EPJ is intrinsically prone to failure because of stress concentrations that occur where material properties change abruptly.[22,23]

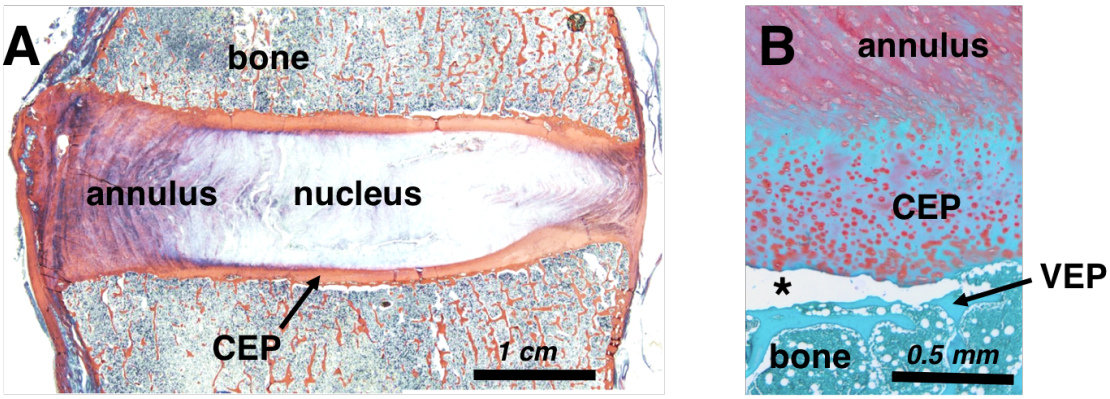

Figure 17. Histologic sections from human cadaveric lumbar spines. (A) Tri-chrome Mallory-Heidenhain stained section depicting the annulus fibrosus, nucleus pulposus, vertebra bone, and cartilage endplate (CEP). (B) Safranin-O stained section illustrating an in situ CEP avulsion (at asterisk) from the underlying vertebral endplate (VEP).

Despite its clinical significance, the biomechanical behavior and structural risk factors of the disc-vertebra interface remain underexplored. *Ex vivo* imaging studies have shown that collagen fibers of the outer annulus extend into adjacent vertebrae and serve to anchor the disc to the bone at the vertebral rim.[59,28] By contrast, fibers of the inner annulus and nucleus integrate with the CEP and sometimes extend into the calcified cartilage layer,[59,80,27] but the CEP shows little to no integration with the underlying bone. Historical data suggest structural weakness at the cartilage-vertebral EPJ, as supported by recent work showing this location as the weak link of the disc-vertebra interface.[81]

The architectural features and biomechanical behavior of other hard-soft tissue interfaces in the body inform hypotheses about structural properties of the disc-vertebra attachment. For example, functional grading of material properties (i.e. mineralization and collagen fiber organization) enables effective stress transfer and decreases stress concentrations across tendon-bone interfaces,[22,23,25] while collagen fiber anchoring of articular cartilage to bone enhances the integrity of attachment.[26] It remains unclear whether similar mechanisms are in place to enhance disc-vertebra integrity.

The goal of the current study was to perform an in-depth analysis of the failure mechanisms of the human disc-vertebra interface and the associated structural features related to collagen fiber anchoring and functional grading. Specifically, we sought to: 1) identify failure mechanisms at the disc-vertebra interface and measure the failure strength and local strain profiles of human bone-disc-bone specimens using biomechanical tension tests; 2) assess the degree of collagen fiber anchoring and functional grading across the EPJ using polarized light microscopy, SEM, and μCT; and 3) perform structure-function correlations to assess which structural features contribute to interface strength. Insight into mechanisms of endplate integrity and features associated with

weakness could help inform new diagnostic tools and more effective treatments for patients with pain due to pathologic EPJs.

Materials and Methods

Sample Preparation

Seventeen cadaveric motion segments were isolated from seven human spines (levels T10-L1, 4M/3F, range 49-65 years old, mean 57.0 ± 9.1 years old) within 72 hours post-mortem (UCSF Willed Body Program). Each motion segment was sectioned on a band saw into ~8mm-thick parasagittal slabs, which were visually classified by two raters using the Thompson grading scheme (Grade 1 = healthy; Grade 5 = severely degenerated),[82] with good inter-rater reliability (kappa = 0.69). Images from one spine (three motion segments) were unavailable for Thompson grading. From the central-most parasagittal slab of each motion segment, cuboidal bone-disc-bone specimens including both outer and inner annulus (~8mm x 8mm in cross-section) were extracted from the posterior annulus (PA) and anterior annulus (AA) regions. Specimens were held in place with wooden blocks while cutting. No visible tears were caused by the sectioning process. Tissue was kept hydrated by spraying with phosphate-buffered saline (PBS) throughout preparation. Six specimens showed existing fissures in the annulus or separations at the EPJ, and were not used for subsequent analyses. One 2mm-thick parasagittal slice from each sample was fixed in 10% formalin for histology and scanning electron microscopy. The remainder of each specimen was designated for μCT and mechanical testing (Figure 18).

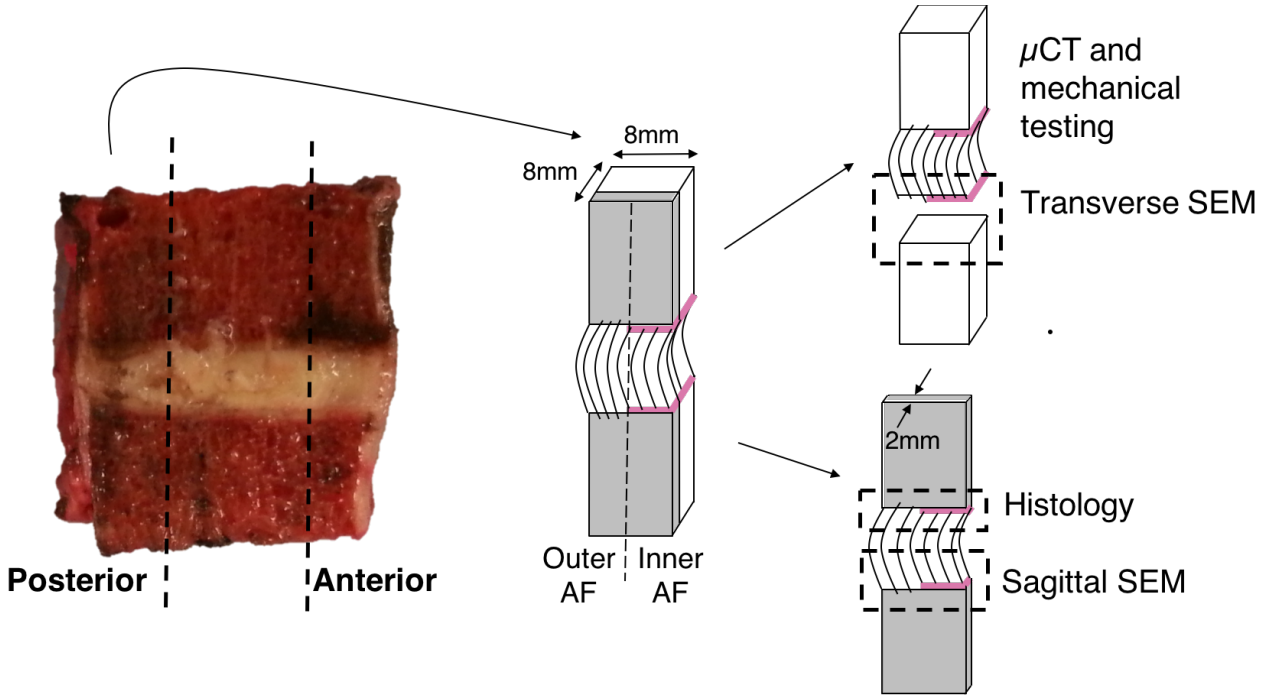

Figure 18. Sample preparation and allocation. Bone-disc-bone specimens were cut from the posterior and anterior annulus regions to include both outer and inner annulus fibrosus (AF). A thin sagittal slice was cut for sagittal-plane histology and SEM, while the bulk sample was scanned with *μ*CT and mechanically tested. Failure surfaces were scanned with SEM. Note that annulus fibers of the outer AF attach directly to the vertebra, while those in the inner AF attach to the cartilage endplate (denoted by pink line).

Micro-Computed Tomography (*μ*CT)

Prior to mechanical testing, specimens were thawed gradually on ice and scanned in PBS at a 15 μm voxel size using a tube voltage of 55 kVp and an X-ray intensity of 109 μA (μCT 50, SCANCO Medical, Brüttisellen, Switzerland). The average duration of the scans was 90 minutes. Image reconstruction was performed using SCANCO software.

A lower threshold of 300 grayscale units was used to segregate mineralized tissue from

soft tissue and scan medium, and Gaussian filters with a sigma of 0.5 and support of 2 were applied to remove noise. Morphometric indices were calculated using a 3D model-independent algorithm, and tissue mineral density (TMD) was calculated using a linear attenuation coefficient determined by calibration with a SCANCO hydroxyapatite phantom. SCANCO Evaluation Program v6.5-3 was used to quantify bone volume fraction (BV/TV), TMD, and trabecular microarchitecture (trabecular number, thickness, and spacing) on a 3 x 3 x 3 mm^3 central cube of trabecular bone 3 mm from the EPJ that failed in mechanical tests (superior or inferior).

Next, a custom script was written in Interactive Data Language (IDL) to quantify TMD and BV/TV at the inferior and superior vertebral endplate regions for each specimen. The algorithm performs the following steps: (1) reads in TMD data; (2) thresholds and masks the bone; (3) crops the central 2.6mm-diameter core of the sample; (4) marches in the axial (Z) direction – beginning above the endplate – and identifies the endplate surface by finding the first non-zero pixel for each X-Y position; and (5) stores TMD values at every pixel for the next 2.25mm depth. Then, the average TMD and BV/TV across the specimen were calculated and saved at every 0.015mm from the endplate to the 2.5mm depth. A custom MATLAB script was then written to calculate endplate TMD and BV/TV (defined as the average TMD and BV/TV in the first 0.2mm-thick region from the surface) and gradients in these properties (defined as the difference between (1) the peak TMD and BV/TV, and (2) the TMD and BV/TV 1mm deeper). The 1 mm distance spans the thickness of the vertebral endplate, which is typically between 0.4 and 1.0 mm thick.[83,84,85] This process is outlined visually in Figure 19.

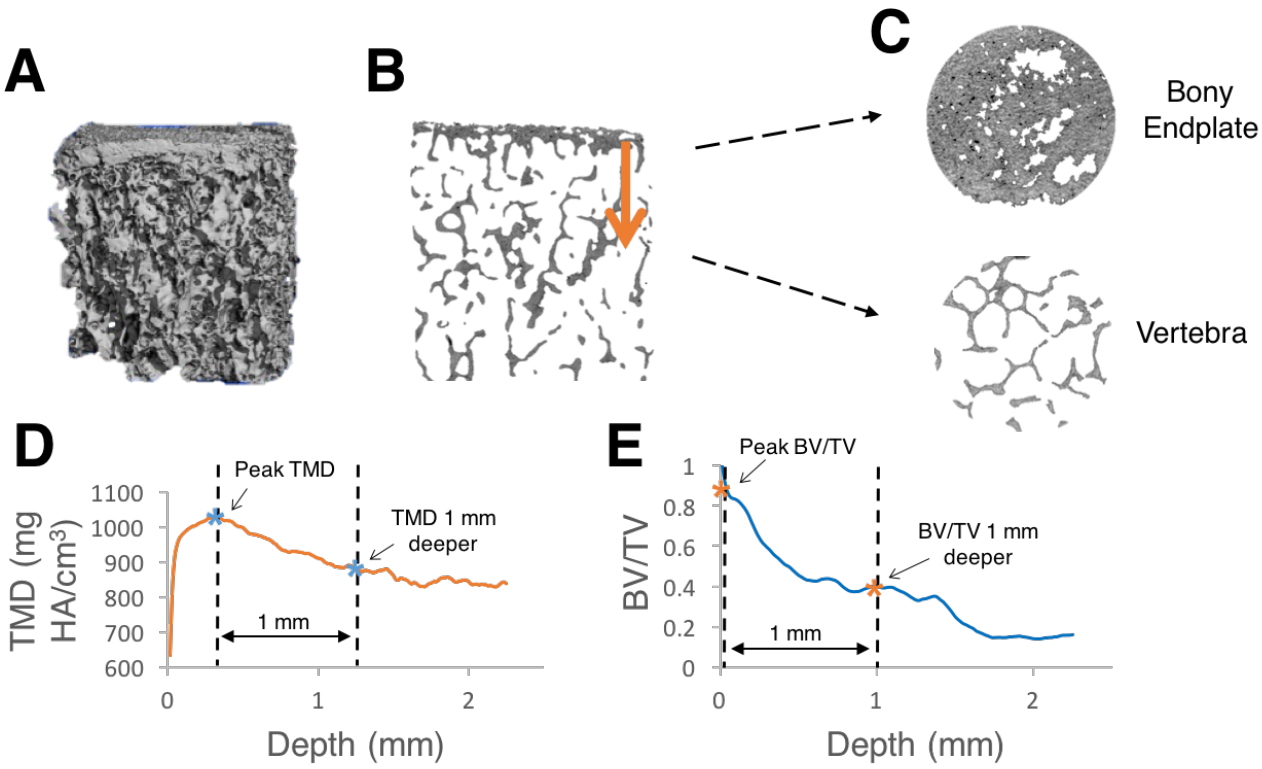

Figure 19. Process of calculating gradients in tissue mineral density (TMD) and trabecular bone volume fraction (BV/TV) at the endplate junction regions. (A) Three-dimensional *μ*CT data is loaded into custom IDL algorithm, (B&C) algorithm traverses from the dense bony endplate into the deeper vertebral bone, and average values of (D) TMD and (E) BV/TV are plotted by depth. Differences between peak values (first asterisk) and values 1 mm deeper (second asterisk) were used to assess local gradients in TMD and BV/TV. Note that (B) and (C) are slices in the sagittal and transverse planes, respectively.

Mechanical Testing

Specimens were cleaned of marrow using a water jet, X-rayed in two orthogonal planes to measure cross-sectional area, speckle-coated on one parasagittal surface with Verhoeff's tissue stain for

DIC, and affixed to a custom testing fixture using casting resin (Figure 20). Specimens were kept hydrated by spraying with PBS throughout preparation. Specimens were preconditioned for 5 cycles between 0-5% tensile strain and, then, loaded to failure in tension at 0.01 mm/s (ElectroForce 3200; Bose, Eden Prairie, MN). The side of the disc where each specimen failed (inferior vs. superior and inner vs outer) was recorded. Force-displacement data were normalized into stress-strain data using cross-sectional area (measured on X-rays as an average of cross-sectional area at the inferior endplate and superior endplate) and initial specimen height (measured with calipers as the average length between the two endplates along the center axis of the specimen's four faces). Measured cross-sectional areas and initial specimen heights were used to normalize the force-displacement data into stress-strain data. A MATLAB algorithm was written to calculate (1) toe region strain, defined as the strain where the stress-strain curve transitions to the linear portion ($R^2 > 0.99$), (2) tensile modulus, defined as the slope of the stress-strain curve during the linear portion, and (3&4) failure strength and strain (Figure 21). The toe region has been previously reported,[49,48] and results from viscoelastic straightening of initially curved annulus collagen fibers. Mechanical tests were unreliable for seven specimens (i.e, casting resin slipped and/or machine became unstable) and thus the data for these specimens were not used for subsequent analyses.

Failure locations were observed visually during testing (Figure 20C). Videos captured during tension tests at 30 frames/sec were watched in slow-motion to confirm initial failure location and observe failure progression. Failed specimen surfaces were visualized after testing to confirm precise failure locations (as determined by tissue types on either side of the failure).

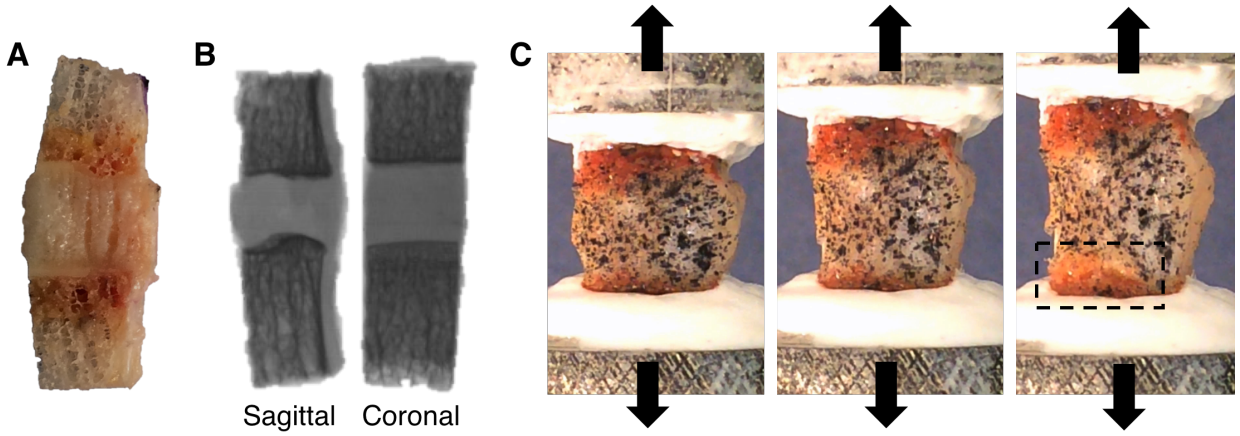

Figure 20. Specimen is (A) cleaned of bone marrow, (B) X-rayed in two orthogonal planes to calculate geometry, and (C) speckle-coated on parasagittal surface, mounted in custom-designed aluminum pots, and pulled in tension to failure. Box in (C) shows location of endplate junction failure. A, B(left), and C are all sagittal views with the inner annulus on the left and outer annulus on the right.

Surface Strain Tracking

Videos of tension tests (1920 x 1080 pixels, 30 frames/sec) were analyzed using DIC. A grid mesh was created on the front-facing speckle-coated sagittal tissue surface. This mesh and sequential images of surface deformation (sampled at 1 frame per 5 seconds) were converted to principal strain profile maps using strain tracking code provided by the Victor Barocas Group at the University of Minnesota.[86] Speckle-coating and tracking parameters were optimized such that tracked subsets were ~15x15 pixels and individual speckles were ~3-5 pixels in diameter. This ratio of speckle size to subset size has been shown to produce high accuracy for DIC[87] and allowed us to track local strains across the CEP, which was typically ~1 mm thick (~30-40 pixels). The error in strain measurements is a function of the optical resolution, speckle size, and subset size,

which for our particular settings was in the range of 10-100 μm. Strain maps were overlaid on specimen test videos (Figure 22). A MATLAB algorithm was written to plot principal strain at each central axial location across the specimen. Principal strains were analyzed – rather than axial strains – due to the nonhomogeneous nature of the tissue samples. Strain gradients were calculated as the difference between the maximum strain (in the annulus) and minimum strain (in the bone), as a surrogate measure of functional grading across the interface.

Scanning Electron Microscopy (SEM)

Following fixation, the adjacent 2 mm-thick parasagittal slices (untested) were separated into superior and inferior halves. The half corresponding to the side that failed mechanically was evaluated with SEM. These untested parasagittal sections, along with transverse failure surfaces of the samples tested mechanically, were dehydrated in an ethanol series with ascending concentrations. Scans of parasagittal sections and transverse failure surfaces were acquired using a Zeiss Sigma 500 scanning electron microscope (Carl Zeiss International, Thornwood, NY).

Histology

The remaining half of each untested parasagittal slice was decalcified in ethylenediaminetetraacetic acid (EDTA), dehydrated in ethanol, embedded in paraffin, and cut into 7-μm thick sections. Three to five sections from each specimen were stained with a tri-chrome Mallory-Heidenhain stain containing aniline blue, orange G, and acid fuchsin to observe gross morphology and to measure CEP thickness. CEP thickness was measured at the inner-most edge of each specimen using ImageJ. The inner-most edge was chosen because all specimens failed initially at the inner annulus. Three to five additional sections from each specimen were stained

with Picrosirius Red to visualize collagen fiber architecture at the EPJ using polarized light microscopy.

Statistics

Statistical analyses were performed using JMP (SAS Institute, Inc.). Paired two-tailed t-tests were used to assess (1) differences in mechanical properties and structural properties between posterior and anterior regions, and (2) differences in structural properties between failed and intact sides of each specimen. Univariate linear regression analysis was performed to assess correlations between mechanical properties and independent variables (structural properties, disc grade/height, and age/sex). Multiple linear regression was used to assess relationships between each mechanical property (toe region strain, modulus, failure strength, and failure strain) and independent structural variables (bone properties, CEP thickness, and Thompson grade). Least-squares estimation with backward elimination was used to predict each mechanical property, where only variables with significant slopes were retained in the model. Significance for all statistical tests was defined by $p < 0.05$.

Results:

Disc and Thompson Grade

The average whole disc height and isolated specimen height were 7.1 ± 1.5 mm and 6.9 ± 1.2 mm, respectively. All discs were Thompson grades 2, 3, and 4 (average 2.6; see Table 2 in Appendix B).

Micro-Computed Tomography

Bone properties measured from central trabecular cubes demonstrated that posterior specimens had a 13% higher tissue mineral density ($p < 0.005$) and 21% lower trabecular spacing ($p < 0.005$) than anterior specimens. This agrees with previous studies showing that bone is denser in the posterior regions.[88,89] Local analyses at the endplate regions revealed a gradient of decreasing BV/TV and TMD from the vertebral endplate into the trabecular bone (Figure 19). Average BV/TV and TMD in the vertebral endplates were 0.72 ± 0.10 and 782.9 ± 67.8 mg HA/cm^3, respectively. BV/TV gradients and TMD gradients (between the location of peak value and 1 mm deeper) were 0.82 ± 0.07 and 53.4 ± 41.6, respectively. BV/TV in the endplates was significantly correlated with BV/TV in the central trabecular bone ($R^2 = 0.23$, $p = 0.03$).

Mechanical Testing

Mechanical failures initiated near the disc-vertebra interface for all specimens (52% at the inferior side and 48% at the superior side). Failure initiated at the inner annulus region and progressed toward the outer annulus region. 71% of primary failures (at the inner annulus region) occurred at the CEP-bone interface, with CEP being stripped from the underlying bone. 21% occurred at the disc-CEP interface, and 8% occurred within the subchondral bone. Following primary failure at the inner annulus region, failure progressed to the outer annulus region, where 42% of secondary failures occurred mid-bone, 41% at the disc-bone interface (note: no cartilage endplate is present between the disc and bone in this out annulus region), and 17% within the annulus (Figure 21). The average modulus, strength, and failure strain were 2.08 ± 1.49 MPa, 0.43 ± 0.16 MPa, and 38.5 ± 20.3%, respectively.

Posterior specimens exhibited a 58% shorter toe region (4.5 ± 1.5% vs. 10.6 ± 6.2%, $p <$

0.01), 50% higher modulus (3.0 ± 1.7 MPa vs. 1.2 ± 0.5 MPa, $p < 0.005$), and 58% lower failure strain (21.3 ± 10.3% vs. 51.1 ± 16.0%, $p < 0.0005$) than anterior specimens (Figure 21). Failure strength was similar between anterior and posterior regions ($p > 0.25$).

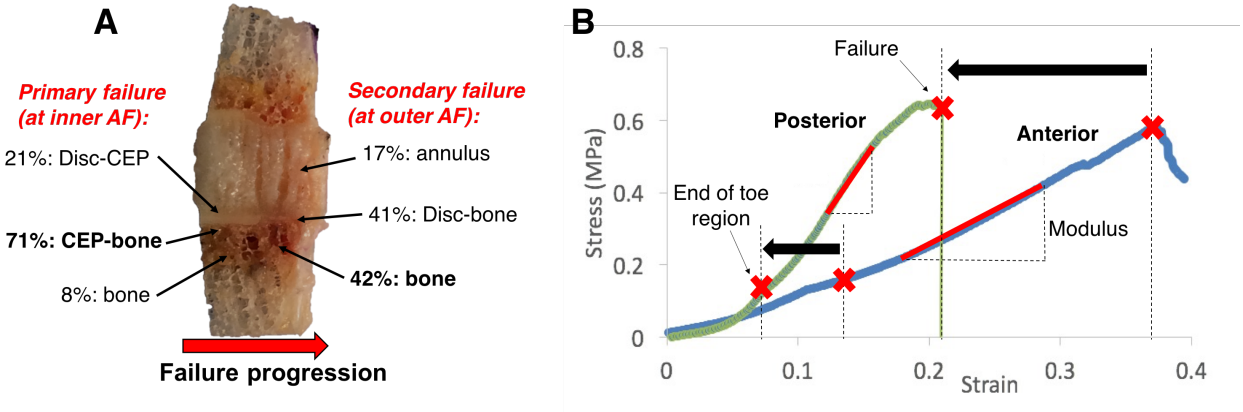

Figure 21. (A) Distribution of failure locations at inner annulus fibrosus (AF) an outer AF regions, with red arrow showing typical direction of failure progression from inner to outer AF. CEP = cartilage endplate; (B) Stress-strain curves for representative posterior annulus and anterior annulus specimens. Posterior specimens had a shorter toe region and lower failure strain (denoted by black arrows) than anterior specimens, as well as a higher modulus than anterior specimens ($p < 0.01$). Strains on x-axis are grip-to-grip strains along the loading axis.

Across all specimens, the highest principal strains occurred mid-annulus, while the lowest occurred in the bone. The strain gradient (measured as the difference between the maximum and minimum principal strains) became steeper with higher applied strains. At very high applied strains (near failure), high local strains were observed at the failure location (Figure 22).

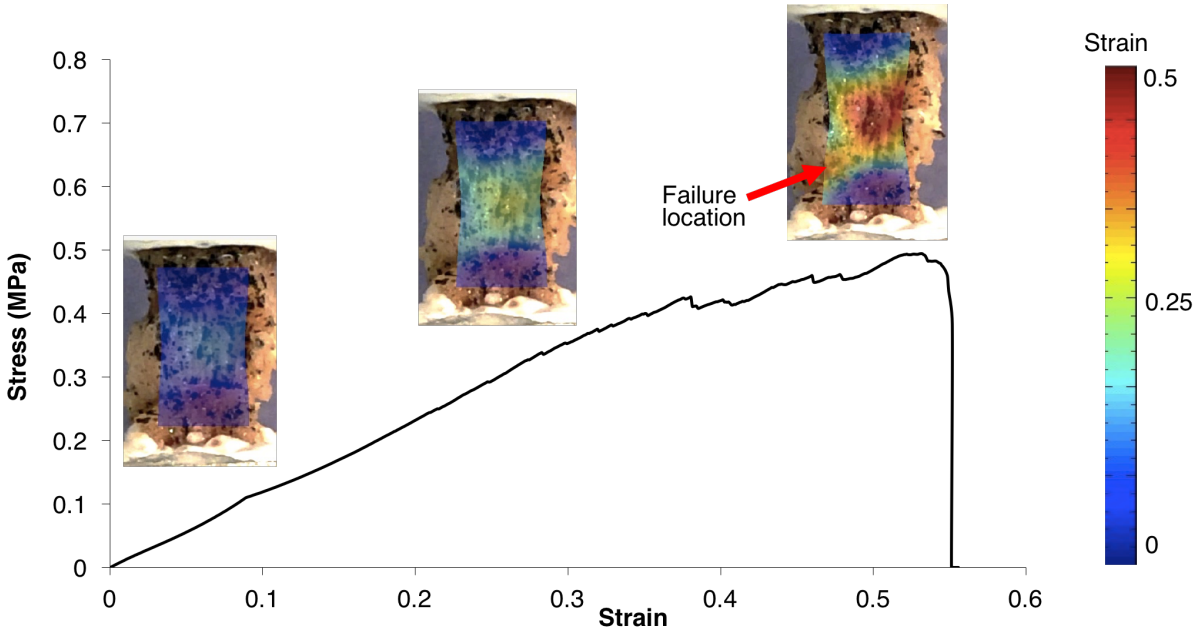

Figure 22. Stress-strain curve for a bone-disc-bone specimen. Strains on x-axis are grip-to-grip strains along the loading axis. Principal strain maps are overlaid on specimen images acquired at corresponding levels of applied strain,

Scanning Electron Microscopy

SEM scans in the sagittal plane indicated a lack of structural integration between the CEP and bone. Many specimens showed a physical gap (5-30 μm thick) between the CEP and bone (Figure 23 D&E). The gap typically either had sporadic thin collagen fibrils showing evidence of a weak connection (Figure 23D) or was void of collagen fibers altogether (Figure 23E). Transverse failure surfaces showed a bed of collagen fibers oriented in the plane of the failure interface (Figure 24). For specimens that appeared to fail at the CEP-bone interface, the vertebral endplate surface displayed cartilage-like fiber morphology, indicating that the specimen failed between the CEP

and the calcified cartilage layer.

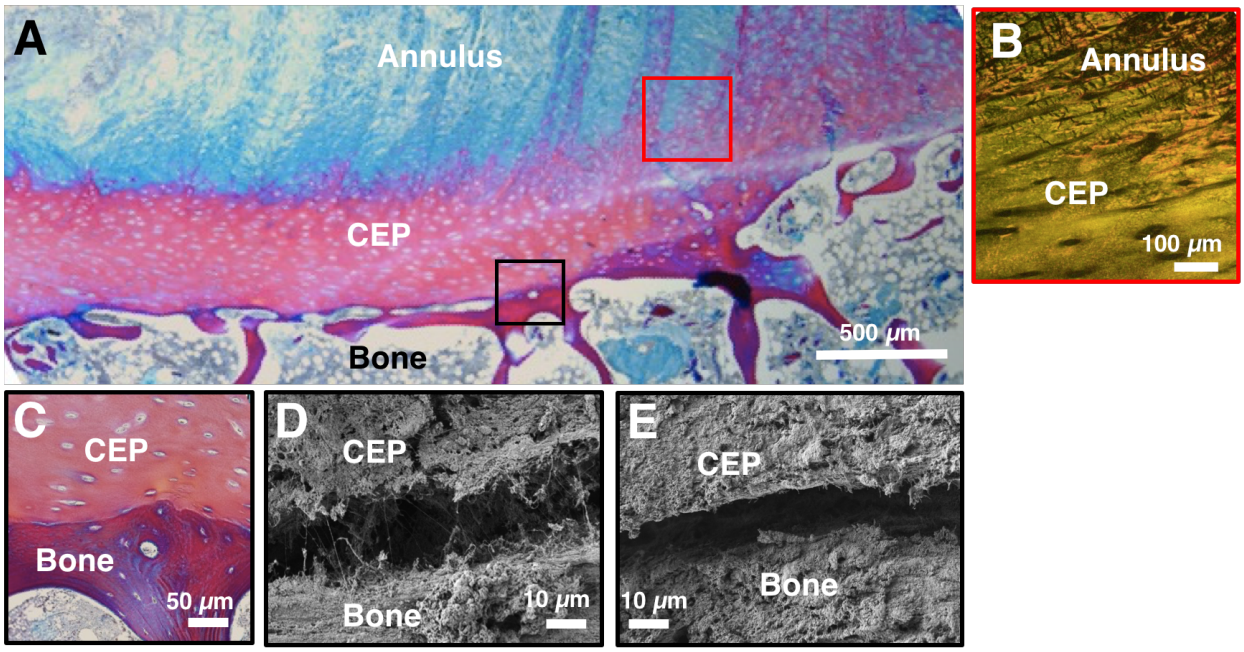

Figure 23. Sagittal histology (A, B, C) and SEM (D ,E) images of the endplate junction. (A, C) are stained with trichrome and (B) is stained with picrosirius red and visualized under polarized light. (B) shows annulus fibers integrating with the cartilage endplate (CEP), while (C) shows a clear demarcation between CEP and bone with no integration. (D & E) show a small gap between CEP and bone using SEM. Black and red boxes on (A) are color-coded to correspond with approximate regions of (B-E).

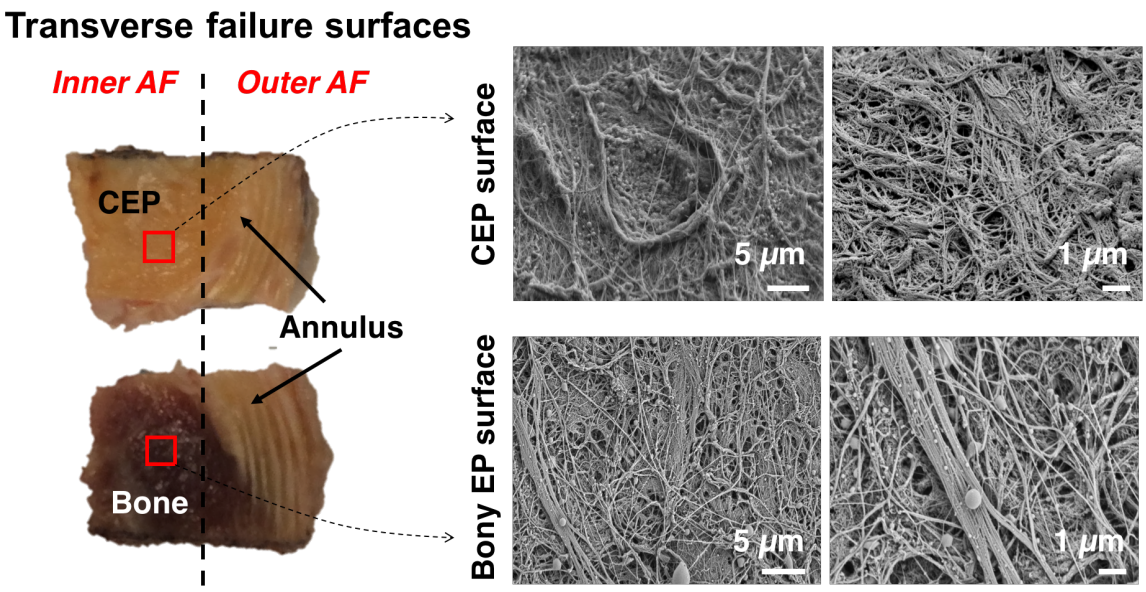

Figure 24. (Left) Transverse failure surfaces for specimen that failed at cartilage endplate (CEP)-bone interface at inner annulus fibrosus (AF) region and failed in mid-annulus at outer AF region. Red squares indicate location of SEM scans; (Right) SEM scans of failure surfaces imaged for CEP and opposing bony endplate surface.

Histology

Histologic sections also indicated a lack of structural integration between the CEP and adjacent bone (Figure 23). Inner annulus fibers joined at oblique angles with the CEP (Figure 23B), but did not anchor into the subchondral bone (Figure 23C). The outer annulus region did not contain CEP, and fibers anchored directly into the vertebral rim, as previously described. The average CEP thickness was 0.85 ± 0.21 mm, as measured at the inner edge of each specimen in ImageJ.

Structure-Function Relationships

Various relationships were found between structural and mechanical properties. Failure stress was

significantly lower in specimens with a Thompson Grade of 4 than those with a Thompson Grade of 2 ($p = 0.026$, t-test; Figure 25). Interestingly, failure stress significantly increased with BV/TV in the failed endplate ($R^2 = 0.35$, $p = 0.015$; Figure 25). Within each specimen, the endplate (inferior or superior) that remained intact during mechanical tests had 8% higher BV/TV and 3% higher TMD than for the endplate that had failed ($p < 0.05$). The intact side also tended to have a 5% lower (less steep) BV/TV gradient ($p = 0.08$).

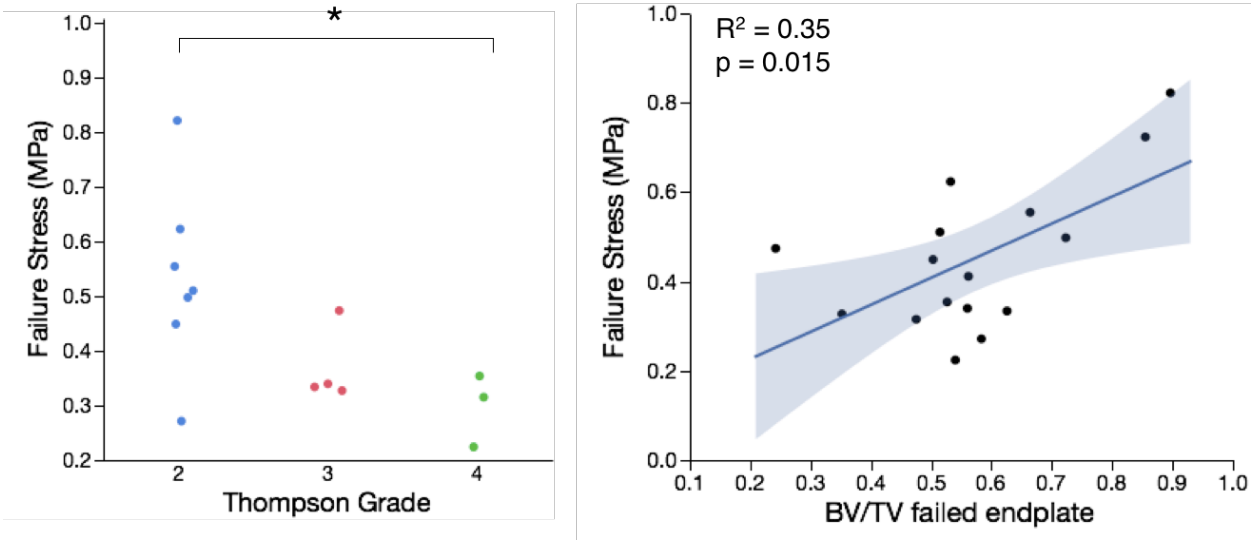

Figure 25. (Left) Failure stress was significantly lower in samples from discs with Thompson Grades 4 vs. 2 (*p = 0.026, t-test); (Right) Failure stress was positively correlated with trabecular bone volume fraction (BV/TV) in the vertebral endplate that failed during mechanical tests ($R^2 = 0.35$, $p = 0.015$).

Failure strength tended to increase with decreasing cartilage endplate thickness, but this relationship was not significant ($R^2 = 0.22$, $p = 0.17$). However, Thompson Grade and CEP thickness were both significant predictors of failure stress in a multiple linear regression model ($p = 0.03$ for both). This multiple linear regression model was statistically significant, with 68% of

the variation in failure stress explained by the predictors (overall p = 0.02). Neither failure strength nor modulus were significantly associated with age, sex, or strain gradients across the endplate (measured by surface strain tracking). However, toe region strain decreased with age (p = 0.03), and both toe region strain and failure strain increased with steeper strain gradients (p = 0.08 and p = 0.02, respectively). No additional significant relationships were found between structural properties and toe region strain, modulus, or failure strain.

Discussion

Our findings indicate that the CEP and vertebra at the inner annulus region are not well-integrated, which is supportive of previous findings[12,90,91] and may explain the weakness of this zone. Because the CEP and inner annulus are structurally integrated, tension at the CEP-bone interface generated during certain spinal movements can avulse the cartilage from the underlying bone (Figure 26).

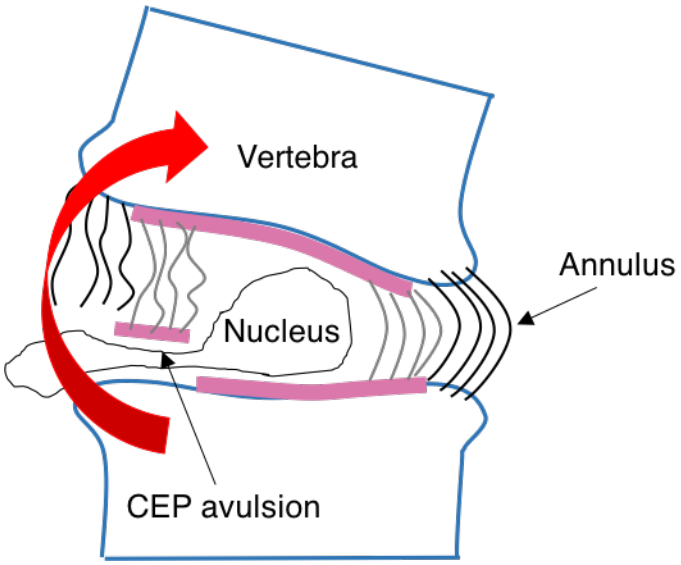

Figure 26. One proposed mechanism of disc herniation, in which cartilage endplate (CEP) is avulsed from bone, allowing disc material to escape. Endplate junction failure is the most

common cause of clinical disc herniations[16] and may occur during spinal movements involving bending motions that place the CEP-bone interface in tension.

Experimentally, we observed that 71% of primary failures occurred at the CEP-bone interface at the inner annulus region, which is consistent with reports that 65% of clinical disc herniations initiate at the CEP-bone interface.[16] After initial failure, the failure surface propagated to the outer annulus region, where secondary failures occurred most often within the annulus or bone rather than the interface. This shift from an interface failure to a tissue substance failure may be attributed to the firm anchoring of the outer annulus fibers into the underlying bone at the vertebral rim,[59,28] which creates a strong connection and transfers the vulnerability away from the interface. This is further supported by whole motion segment bending tests showing that the peripheral annulus fibers remains attached to the vertebral rim, while the middle annulus commonly pulls cartilage away from the underlying bone.[92] This may mimic failure progression *in vivo* during herniation.

We have reported new structure-function relationships at the disc-vertebra interface. We observed that bone density of the vertebral endplates plays an important role in the strength of the disc-vertebra interface, as evidenced by: (1) a positive linear correlation between BV/TV and failure strength, and (2) significantly higher BV/TV and TMD in the intact end compared to the damaged end of each specimen. These findings suggest that denser bone in the vertebral endplate creates a larger surface area of attachment to the CEP, thereby strengthening the interface.

Importantly, we found significant relationships between clinically measurable parameters and failure strength. Peripheral CEP thickness can be measured clinically with new imaging techniques that can visualize the CEP, such as fast low-angle shot (FLASH) MRI[20] and ultrashort

echo-time (UTE) MRI.[19,21,93] Our findings suggest that disc degeneration grade and CEP thickness may serve as potential clinical risk measures for avulsion-type herniation. However, the sample size was limited, and future studies should further assess these correlations in human subjects. We did not find a significant effect of age on failure strength, which may be related to the narrow age range in this study or the fact that disc degeneration occurs at different rates. Interestingly, CEP thickness was a negative predictor of failure strength. This may be due to a thicker CEP creating a larger separation between the annulus and bone, thereby reducing structural integration between the annulus and bone. Lastly, we found that BV/TV in the failed endplate (which was a significant predictor of failure strength) was significantly correlated with trabecular BV/TV in the vertebra, indicating that clinical quantitative computed tomography (QCT) or dual-energy X-ray absorptiometry (DXA) measures of vertebral bone quantity may also be predictive of disc-vertebra injury risk.

Although the disc-vertebra interface bears complex loads including shear, compression, tension, and torsion, we applied uniaxial tension in order to examine the cohesive properties of the EPJ. Further, tension at this interface may be particularly important since it is known that forward bending is the main contributor to disc herniation injuries, which places the posterior annulus into tension.[92,30] Moreover, sheep discs subjected to axial tension contain more EPJ failures than those subjected to torsion or in-plane tension.[58] Failure stresses and failure locations measured in the current study were consistent with those found in previous human disc-bone tensile tests. Our measured failure stresses (range: 0.22 - 0.93 MPa) were within the range of those reported by Balkovec and coworkers[81] (range: 0.14 - 2.8 MPa) and lower than those found by Green and coworkers[49] (average 1.7 MPa for posterior and 3.8 MPa for anterior annulus), presumably because we cut our specimens smaller to isolate more specific regions, thus disrupting the collagen network

mid-fiber due to the angled orientation of annulus fibers. The higher modulus of the posterior annulus compared to the anterior annulus may help to resist forward bending movements, but the lower extensibility may put weak EPJs at risk for herniation.

Microstructural imaging showed very little structural integration between the disc and vertebra. SEM showed 5-30 μm discernible gaps between the CEP and bone with no ligament-like bridging other than thin individual collagen fibrils (Figure 23D&E). These gaps may be a result of interlaminar delamination caused by scanning under vacuum (low pressure), which is a known artifact of electron microscopy and has been observed in previous studies.[94,27] Delamination was not observed in any other regions of the specimens, and provides additional evidence of the fragility of this interface.

The weakness of the CEP-vertebra interface is in stark contrast to other cartilage-bone interfaces, such as the articular cartilage-bone interface and ligament and tendon insertions, where collagen fibers are oriented perpendicular to the interface and anchor the soft tissue to the bone[25,26,95]. Collagen fiber anchoring at the CEP-vertebra interface may be unnecessary in healthy discs with normal loading, as high nucleus pressure keeps the cartilage pressed onto the bone and prevents tension from developing across the interface.[77,96] However, when a disc is subjected to very high bending loads, tensile forces in the inner annulus may cause the CEP to avulse. Degenerated discs with diminished nuclear pressure may be at a higher risk of CEP avulsion. This is supported by studies showing that CEP fragments found in disc herniations were associated with increasing age and degeneration.[97–99] Therefore, although many disc herniations occur in younger individuals with non-degenerated discs,[13] avulsion-type herniations may occur more commonly in the elderly.

A significant limitation of this study is that we tested only thoracic levels because most lumbar levels of the donor spines contained annular fissures and existing defects at the CEP-bone interface that precluded harvesting intact specimens for analysis (Figure 27. The majority of clinical disc herniations occur in the lumbar spine.[100] Although we tested only lower thoracic levels (T10-L1), we expect that our conclusions regarding the importance of structural integration applies to lumbar specimens, which have similar endplate morphology. Moreover, the annular fissures and defects at the CEP-bone interface in the lumbar levels further evidences the weakness of this interface *in vivo*.

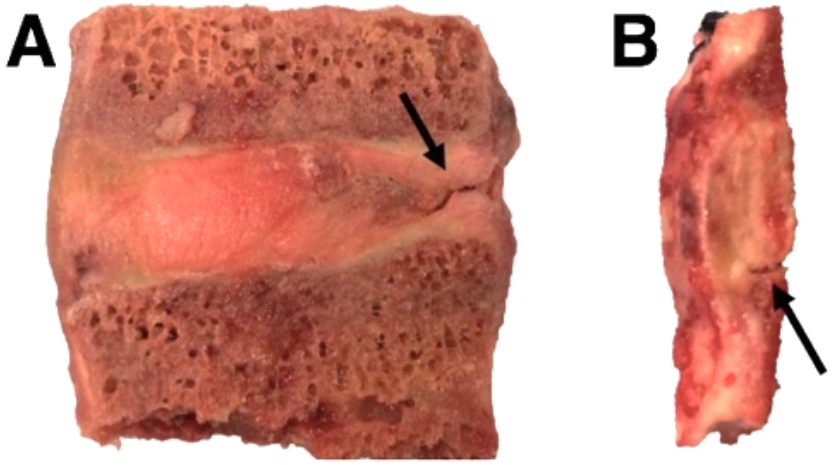

Figure 27. Un-tested lumbar specimens. Specimens are often too degenerated for mechanical testing and show (A) annular fissures and (B) separation at the CEP-bone interface.

Another limitation of this study is that deformation fields were only measured on the front-facing parasagittal surface during tension testing. Because of this, initial failures that occurred mid-section or at the opposite parasagittal surface were not captured in videos. This is an inherent limitation of 2D strain tracking on 3D tissue. However, we were able to determine when initial

failure occurred from drops in force-displacement curves and correlate failure strength to our measured structural properties. Furthermore, the general location of initial failure (i.e. inner vs. outer annulus) was evident by visually observing failure progression as samples were pulled to complete failure, and precise locations of failure were evident by observing the failed surfaces following testing.

Functional grading of material properties at interfaces of dissimilar biological materials is a mechanism of smoothing structural discontinuities and decreasing stress concentrations. Examples of this are the grading of mineral and collagen at the tendon-bone interface[22,23,25,101], grading of structural and chemical properties of the bone-tooth interface,[102] and grading of fiber orientation in the tissue encasing blood vessels in bone.[103] At the disc-vertebra interface, we observed that local TMD and BV/TV gradients weakly associated with interface strength, although the magnitude of TMD and BV/TV at the endplates was a more significant predictor. Future studies should investigate functional grading across the entire endplate junction (annulus-CEP-bone). For example, nano-indentation could be used to investigate stiffness of each involved tissue, and whether gradients in stiffness affect attachment strength.

In summary, we have measured failure strength, characterized failure mechanisms, assessed nanoscale structural connectivity, and uncovered structure-function relationships at the human disc-vertebra interface. Our results highlight the vulnerability of the CEP to tensile failure because of poor structural integration with the subchondral bone. We have also shown that disc degeneration grade, vertebral endplate bone density, and CEP thickness are all important predictors of disc-vertebra failure strength. Our observations reinforce the need for diagnostic tests to characterize the integrity of this region, and activity modification to reduce the tensile stresses at this interface in at-risk individuals. Further, these data motivate the development of treatments

that target this region.

Acknowledgements

This work was supported by NIH R01 AR063705 and an NSF Graduate Research Fellowship. μCT imaging was performed at the Bone Imaging Research Core of the Endocrine Research Unit at the UCSF-affiliated Veterans Affairs Medical Center. We would like to thank Claudia Iriondo for collecting sagittal SEM images, Dr. Jeannie Bailey for helping with Thompson grading and offering statistics advice, and Alice Rochette for assisting with histology sectioning and staining. We would also like to thank Dr. Amy Claeson for graciously helping us with the strain tracking code provided by the Victor Barocas Group, and Dr. Sunita Ho and Dr. Ling Chen for assisting with SEM scanning and interpretation. None of the authors have affiliations that are perceived to have biased the presentation.

Chapter 4: Classification of Endplate Irregularities and High Prevalence of Tidemark Avulsions

The content of this chapter will be included as part of a research article that will be submitted to Spine in June 2017 by the following authors:

Britta Berg-Johansen, Deeptee Jain, Ellen C. Liebenberg,

Aaron J. Fields, Thomas M. Link, Conor W. O'Neill, Jeffrey C. Lotz

University of California, San Francisco

Abstract

Irregularities at the spinal disc-vertebra interface are associated with back pain and intervertebral disc herniation injuries. However, studies on pathophysiology, natural history, and clinical significance are limited by a lack of consensus on terminology and classification.

To address this, we identified and categorized types of endplate irregularities using histology. We identified a highly prevalent form of endplate irregularity, in which the outer annulus separates from the vertebra at the tidemark. These "tidemark avulsions" were visible on T^2-weighted MRI as high-intensity zones (HIZs). Ongoing work involves development of a histologically-driven MRI classification scheme that will reduce ambiguity for diagnoses and clinical studies relating endplate pathologies to pain.

Introduction

Endplate irregularities at the disc-vertebra interface in the spine are associated with back pain and injury;[15,16,77,79] however, studies on pathophysiology, natural history, and clinical significance are limited by a lack of consensus on terminology and classification. In a recent survey of a working group from the International Society of the Lumbar Spine (ISSLS), approximately 84% of orthopaedic clinicians and 80% of orthopaedic researchers agreed that a standardized endplate nomenclature is clinically needed.[104] Standardized nomenclature will improve the accuracy and consistency of clinical diagnostics, thereby enhancing therapeutic decision-making.

Clinical classification is often confused by various terms used to describe the same type of endplate irregularity; for example, separation at the annulus-vertebra interface has been described using several terms such as "avulsion," "cartilaginous herniation," and "endplate junction failure."[14–16,77,105–107] Conversely, the same term is often used to describe two or more different types of endplate irregularities; for example, nodes with traumatic expulsion of disc material vs. nodes showing more erosive morphologies are both termed "Schmorl's nodes,"[108,109] despite evidence suggesting that they have very different etiologies.[110] Another example of this is the use of the term "rim lesion" to describe both bony lesions and annular lesions near the endplate junction.[111–113]

To address the need for standardized nomenclature, the aims of this study were to: (1) identify and classify endplate pathologies in a cadaver population using histology, and (2) correlate histology and MRI findings. Rather than relying solely on MRI findings, our use of histology provided a high-resolution view of tissue features and structures involved, thereby providing the mechanistic underpinnings for clinical classification.

Materials and Methods

Study Population and Imaging

Fifteen cadaveric spines with moderate to severe disc degeneration (11 male / 4 female, age range 49-67 years, mean 58.2 ± 5.8 years) were obtained from donors within 72 hours post-mortem (UCSF Willed Body Program) and scanned *in situ* in the sagittal plane with MRI (GE 3T Signa HDx scanner; GE Healthcare, Waukesha, WI, USA). All 15 spines were scanned using two-dimensional T_1-weighted and T_2-weighted fast spin-echo sequences, and 8 of the 15 spines were also scanned using a three-dimensional ultrashort echo-time (UTE) sequence.

Histology Assessment

Following imaging, 89 lumbar and lower thoracic bone-disc-bone motion segments were extracted from the fifteen intact spines using a band saw. Motion segments were cut into 5- to 8-mm-thick parasagittal slabs, and ~1 cm thick parasagittal slabs from areas with known endplate irregularities were fixed in 10% formalin for histology. After fixation, slabs were decalcified in ethylenediaminetetraacetic acid (EDTA), dehydrated in ethanol, embedded in paraffin, and cut into 7-μm thick sections. Several sections from each motion segment were stained using the following stains: Hematoxylin and Eosin (H&E) for observing overall morphology, Masson thrichrome and Mallory-Heidenhain for visualizing connective tissue, including annular lamellae and their junction with the bony endplate, and Safranin O Fast Green for clear visualization of the cartilage endplate (CEP). Sections were imaged on a microscope with and without polarized light at 0.5X, 2X, 4X, 10X, and 20X magnifications. Histology images were assessed by two raters. A classification scheme of endplate irregularities was generated, and incidence of each type was recorded. Anatomical location (anterior/posterior and inferior/superior) of each endplate

irregularity was also recorded.

MRI Assessment

MR images of each spine were assessed by two clinical spine specialists. The use of different raters for MRI than those for histology allowed for unbiased comparisons between histology and MRI endplate irregularity classification. Each type of endplate irregularity seen on MRI was recorded, along with anatomical location.

Results

Histology Classification

Based on location and patho-anatomical features, endplate irregularities were grouped into the following categories and subcategories:

I. *Avulsion*: tissue separation at the disc-vertebra interface
    i. Tidemark avulsion: separation along tidemark, where outer annulus fibers insert into the calcified cartilage layer (Figure 28A and Figure 29C&D)
    ii. CEP-bone avulsion: separation between the cartilage endplate (CEP) and bone (Figure 28B)

II. *Nodes*:
    i. Traumatic: herniation of nucleus material through endplate (Figure 28C)
    ii. Erosive: bony erosion and abnormal fibrocartilage ingrowth (Figure 28D)

III. *Rim degeneration*: degeneration of bone-annulus interface, including bone marrow changes and loss of annular fiber organization (Figure 28E)

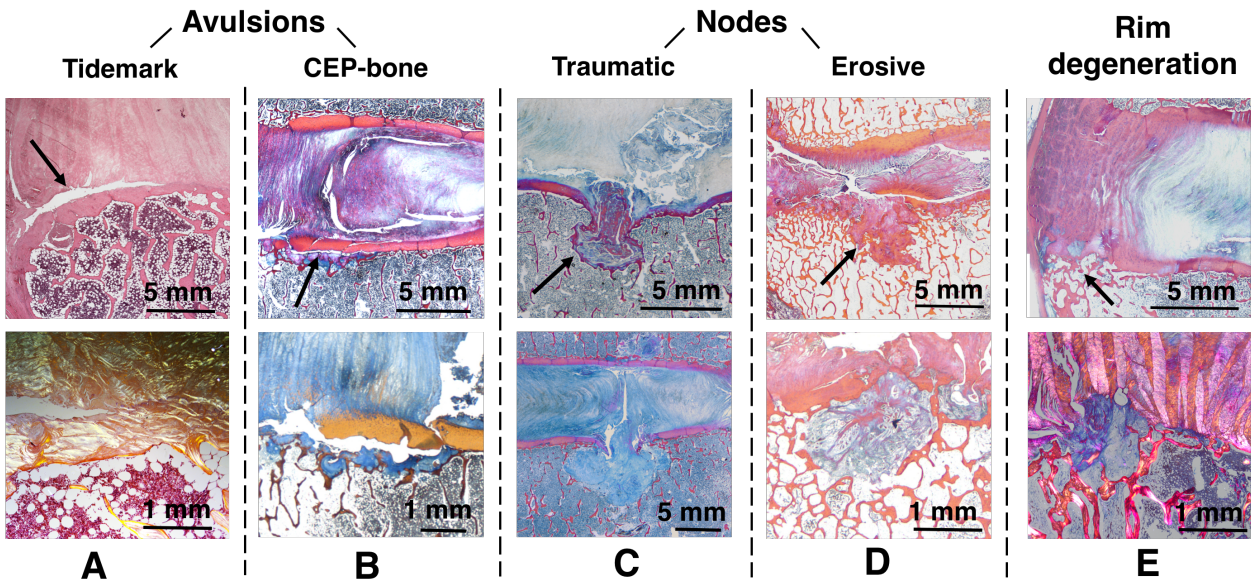

Figure 28. Categories of endplate irregularities as seen with histology: (A) Tidemark avulsion at the insertion of annulus fibers into the calcified cartilage layer; (B) CEP-bone avulsion; (C) traumatic node; (D) erosive node; (E) rim degeneration. Top images are lower magnification, with arrows pointing to endplate irregularities. Sections in (A) are stained with Hematoxylin and Eosin (top) and Safranin O (bottom), while sections in (B-E) are stained with Mallory-Heidenhain trichrome stain. Bottom images of (A) and (E) are taken under polarized light.

Prevalence of Endplate Irregularities

Ninety percent of avulsions occurred along the tidemark where outer annulus fibers insert into the calcified cartilage layer (Figure 29). Annulus fibers were observed to change direction upon crossing the tidemark (Figure 29A&B). Tidemark avulsions occurred in 35 of 89 discs, and of those discs, 14 had multiple avulsions. Eighty-seven percent of all avulsions occurred anteriorly.

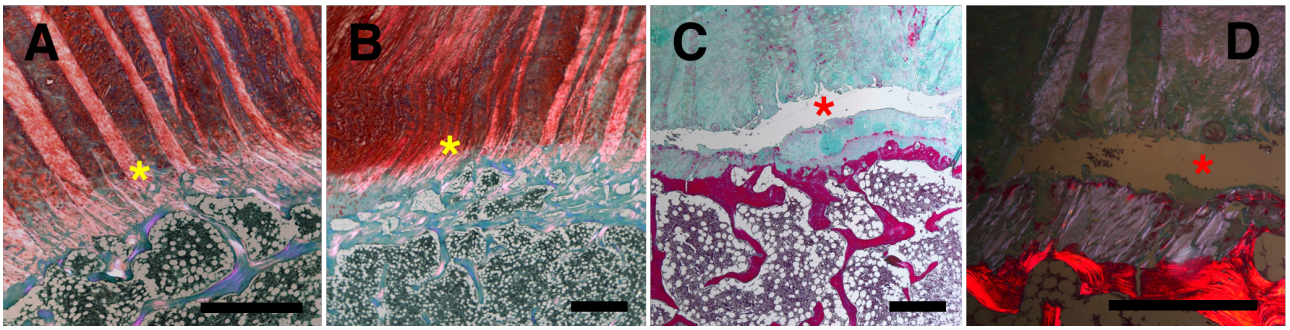

Figure 29. Histology images of (A&B) intact tidemarks, denoted by yellow asterisks, and (C&D) tidemark avulsions, denoted by red asterisks. Note that collagen fibers change direction at the tidemark (A&B). Sections are stained with (A,B,D) Hematoxylin and Eosin under polarized light, and (C) Masson Trichrome. Scale bars represent 1 mm.

Avulsions and rim degeneration were more common than nodes (Figure 30A) and occurred most frequently in the lumbar spine (Figure 30B), while nodes occurred most frequently in the thoracic spine. The number of cases of each endplate irregularity did not correlate significantly with age ($p > 0.3$).; however, the three oldest spines (ages 63, 65, and 67) had the highest numbers of tidemark avulsions (11, 7, and 8, respectively). Often, similar endplate irregularities were observed in multiple discs of the same spine; for example, 20 of 23 nodes were distributed amongst only 5 of the 15 spines, with 7 nodes occurring in a single spine (Figure 30C).

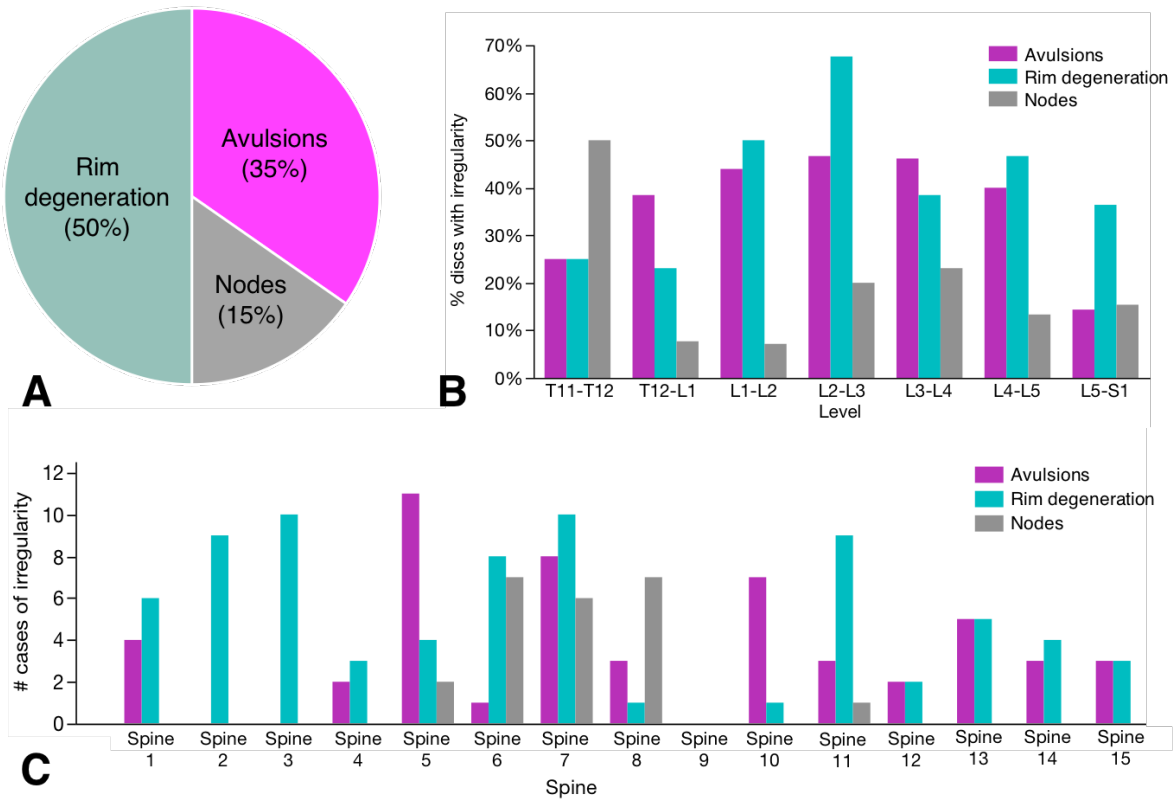

Figure 30. (A) distribution of endplate irregularities by category; (B) distribution of endplate irregularities by disc level; (C) distribution of endplate irregularities by individual, demonstrating a single category of irregularity often occurring multiple times in a given spine.

Tidemark Avulsions as High-Intensity Zones on T_2-weighted MRI

Tidemark avulsions were visible on T_2-weighted MRI as high-intensity zones (HIZs) in the corners (Figure 31). Interestingly, even small tidemark avulsions were visible, and in fact, appeared larger on MRI than on histology. Tidemark avulsions were not pronounced on T_1-weighted and UTE MRI (Figure 32).

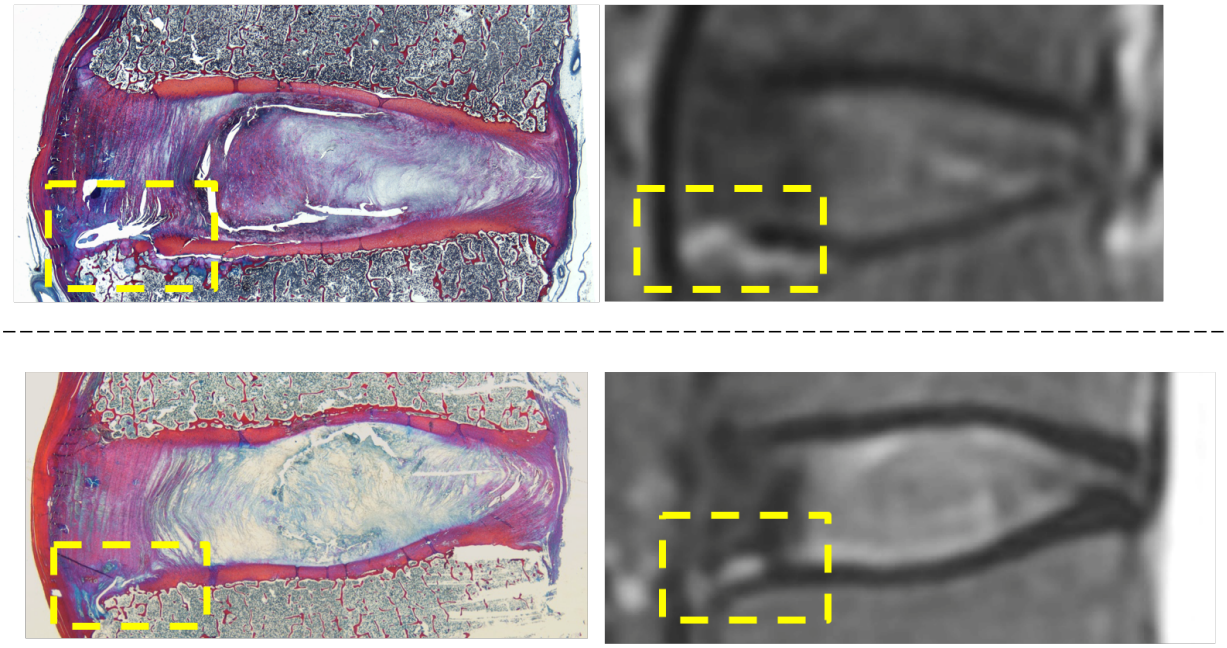

Figure 31. Tidemark avulsions on histology (left) and T2-weighted MRI (right). Tidemark avulsions appear as high-intensity zones (HIZ) on MRI.

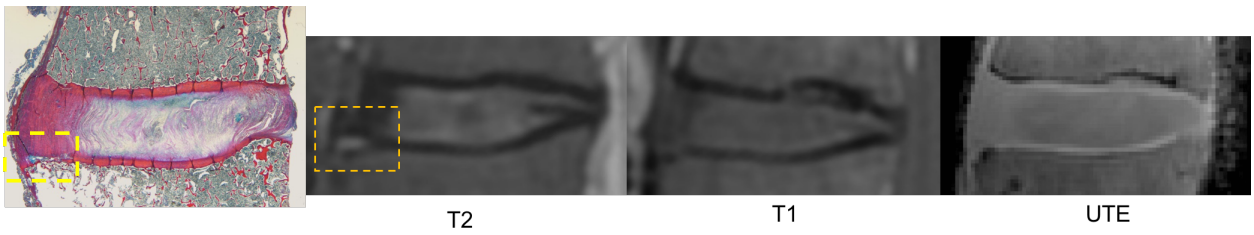

Figure 32. Tidemark avulsions on histology, T2-weighted MRI, T1-weighted MRI, and UTE. HIZ is visible on T2-weighted MRI. This finding is not pronounced on T1-weighted MRI and UTE.

Discussion

This study reveals the high prevalence of avulsions at the tidemark between the annulus and calcified cartilage layer. While rim lesions are well-documented,[113,114] the precise failure location of annulus fibers along the tidemark has only been described in biomechanical studies of excised animal tissue[106] and has not been previously described in human spines and related to MRI findings.

While the tidemark has not been identified as a main injury source, several studies have observed the anatomy of the tidemark in human spines.[12,91] By definition, a tidemark is the mineralization front between a calcified and non-calcified layer of tissue, and is also observed in tendon-bone insertions[23] and articular cartilage-bone interfaces.[115] Around the periphery of the disc where we observed tidemark avulsions, the cartilage endplate is calcified throughout its entire thickness, and the tidemark lies between the annulus and calcified cartilage. In the central portion of the disc, the cartilage endplate is mainly uncalcified hyaline cartilage, and the tidemark exists between the hyaline cartilage and a very thin or indiscernible layer of calcified cartilage.[12,105] Our observation that annulus fibers change direction upon crossing the tidemark agrees with previous observations.[91,105]

This study's finding that tidemark avulsions can be seen on MRI has great clinical significance. Damage at the disc-vertebra interface has been linked with both pain and injury,[15,16,77,79] and we have now shown for the first time that even minor separations at the disc-vertebra interface are visible on T_2-weighted MRI as HIZs. The presence of HIZs suggests that avulsion creates a defect, which collects fluid due to a vacuum effect, and this fluid collection is visible on MRI. Alternatively, gas may accumulate within the separation from surrounding

extracellular spaces, much like the "vacuum phenomenon" that has been observed in disc spaces and noted as high intensity zones on T_2-weighted MRI.[116,117] We found that tidemark avulsions appeared larger on MRI than histology, which may be explained by fluid and/or gas collections being lost during *ex vivo* sectioning. We initially hypothesized that the tidemark avulsions we observed on histology may have occurred during histology preparation, thus limiting clinical utility; however, the presence of HIZs on MRI showed that these avulsions are not purely histology preparation artifacts.

The term "high intensity zone" for spinal MRIs typically refers to areas of high signal intensity within the posterior annular substance on T_2-weighted MRI, and often reflects annular fissures.[118,119] The relationship between these annular HIZs and back pain is highly debated. Earlier studies found that HIZs may be a highly-specific signal for back pain,[120,121] whereas more recent work has shown that HIZs are prevalent in both symptomatic and asymptomatic individuals.[117] The HIZs we have observed in the current study differ from the classically-observed annulus HIZs in that they are located at the peripheral disc-vertebra interface. We have shown that these interfacial HIZs associate with delamination injury as seen with histology. Because of the aforementioned associations between endplate defects and back pain, these HIZs may represent painful lesions. Furthermore, recent work has found that the Oswestry Disability Index (ODI) score, an index used to quantify disability for low back pain, was significantly higher for discs with abnormally elevated anterior disc widening during dynamic flexion/extension imaging.[124] Anterior disc widening may, in theory, be caused by tidemark avulsions allowing the disc to detach and separate from the vertebra. This agrees with our findings that the majority (87%) of tidemark avulsions occurred anteriorly.

The mechanism of failure at the tidemark remains unclear. A biomechanical study of excised ovine tissue found that disc-bone specimens were more likely to fail at the tidemark in axial tension than in torsion or in-plane tension, and hypothesized that this may be due to acute fiber bending where the annulus fibers enter the calcified cartilage.[106] This suggests that tidemark failures may occur during bending, putting the annulus is tension. Despite our finding that the majority of tidemark avulsions occur anteriorly, traumatic avulsions coincident with disc herniation (not included in our study population) often occur posteriorly, with the inner annulus avulsing the cartilage endplate during forward bending. This difference, along with the high prevalence of tidemark avulsions we observed in discs from older donors, suggests that tidemark avulsion may be a repetitive-loading (fatigue) injury while cartilage endplate-bone avulsion may be a traumatic injury. Further studies are needed to test this hypothesis, such as biomechanical studies of the tidemark under fatigue loading.

This study has several limitations. First, we performed MRI on cadaver spines using higher resolution than typical clinical MRI. It is possible that tidemark avulsions may be more difficult to discern clinically due to limited image resolution. Thus, further studies are needed to confirm the visibility of tidemark avulsions with clinical MRI. Additionally, we retrospectively analyzed histology slides and MR images collected over the past several years that were not co-registered, and were therefore unable to match the exact location of histology slices with MRI slices. Despite this limitation, we were able to approximately match locations based on disc and endplate morphology.

We observed that similar endplate irregularities often occurred in multiple discs of a given spine, motivating further analysis of the unique etiologies of endplate irregularities and patient-specific risk factors. Additionally, ongoing analyses include nerve-staining of histology sections

to assess correlations between innervation and tidemark avulsions. Future clinical studies will also be important for assessing whether the tidemark avulsions observed in the current study correlate with symptoms, which would have major implications for diagnostics and treatment. Lastly, we are correlating MRI and histology classification of endplate irregularities and refining a histologically-driven MRI classification scheme. This classification scheme will serve as a valuable tool for standardizing types of endplate damage.

Acknowledgements

This study was supported by NIH R01 AR063705.

Chapter 5: Cartilage Endplate Thickness Variation Measured by Ultrashort Echo-Time MRI is Associated with Adjacent Disc Degeneration

The content of this chapter has been submitted as a research article to *Spine* and is currently in review. The authors are as follows:

Britta Berg-Johansen, PhD,*[1,2] Misung Han, PhD,*[3] Aaron J. Fields, PhD,*[1] Ellen C. Liebenberg, BS,[1] Brandon J. Lim, BS,[1] Peder EZ Larson, PhD,[2,3] Cigdem Gunduz-Demir, PhD,[4,5] Galateia J. Kazakia, PhD,[3] Roland Krug, PhD,[3] Jeffrey C Lotz, PhD[1,2]

* These authors contributed equally to this work

1. Department of Orthopaedic Surgery, University of California, San Francisco, CA, USA
2. Department of Bioengineering, UC Berkeley/UCSF Joint Program in Bioengineering, Berkeley, CA, USA
3. Department of Radiology and Biomedical Imaging, University of California, San Francisco, CA, USA
4. Department of Computer Engineering, Bilkent University, Ankara, Turkey
5. Neuroscience Graduate Program, Bilkent University, Ankara, Turkey

Abstract

Study Design: A magnetic resonance imaging study of human cadaver spines.

Objective: To investigate associations between cartilage endplate (CEP) thickness and disc degeneration.

Summary of Background Data: Damage to the CEP is associated with spinal injury and back pain. However, CEP morphology and its association with disc degeneration have not been well characterized.

Methods: Ten lumbar motion segments with varying degrees of disc degeneration were harvested from six cadaveric spines and scanned with MRI in the sagittal plane using a T_2-weighted 2D sequence, a 3D ultrashort echo-time (UTE) imaging sequence, and a 3D $T_{1\varrho}$ mapping sequence. CEP thicknesses were calculated from 3D UTE image data using a custom, automated algorithm, and these values were validated against histology measurements. Pfirrmann grades and $T_{1\varrho}$ values in the disc were assessed and correlated with CEP thickness.

Results: The mean CEP thickness calculated from UTE images was 0.74 ± 0.04 mm. Statistical comparisons between histology and UTE-derived measurements of CEP thickness showed significant agreement, with the mean difference not significantly different from zero ($p = 0.32$). Within-disc variation of $T_{1\varrho}$ (standard deviation) was significantly lower for Pfirrmann grade 4 than Pfirrmann grade 3 ($p < 0.05$). Within-disc variation of $T_{1\varrho}$ and adjacent CEP thickness heterogeneity (coefficient of variation) had a significant negative correlation ($r = -0.65$, $p = 0.04$). The standard deviation of $T_{1\varrho}$ and the mean CEP thickness showed a moderate positive correlation ($r = 0.40$, $p = 0.26$).

Conclusions: This study demonstrates that quantitative measurements of CEP thickness measured from UTE MRI are associated with disc degeneration. Our results suggest that variability in CEP thickness and $T_{1\rho}$, rather than their mean values, may serve as valuable diagnostic markers for disc degeneration.

Key words: cartilage endplate; endplate thickness; intervertebral disc; ultrashort echo-time MRI (UTE MRI); disc degeneration; low back pain; lumbar spine; image segmentation; image processing algorithm; T1rho; Pfirrmann grade; spatial variation

Key points:

- Cartilage endplate thickness was measured from ultrashort echo-time MRI using a novel automatic segmentation algorithm
- Variation in and $T_{1\rho}$ was significantly lower for discs with higher Pfirrmann grades.
- Variation in cartilage endplate thickness was significantly correlated with variation in $T_{1\rho}$.
- Our results suggest that variation in cartilage endplate thickness may be an important clinical marker of disc degeneration.

Mini Abstract:

In this study, lumbar motion segments were scanned with MRI, and CEP thickness was calculated from ultrashort echo-time MR images and correlated with disc degeneration parameters. We found that variation in CEP thickness was significantly associated with disc degeneration and therefore may be a valuable diagnostic marker for back pain patients.

Introduction

Low back pain is the leading cause of disability worldwide, affecting 70% to 85% of the population during their lives.[3] Costs related to back pain are estimated to exceed $100 billion every year in the United States.[125] With increasing average life expectancy, the prevalence of low back pain is likely to increase.[126] While the precise causes of lower back pain are not well understood, intervertebral disc degeneration is believed to be a leading factor.[127,128]

The intervertebral disc is avascular and is composed of a central gel-like nucleus pulposus, a surrounding annulus fibrosus, and superiorly and inferiorly located cartilage endplates (CEPs).[129] The nucleus pulposus mainly consists of proteoglycan and water so as to resist spinal compression hydrostatically. The annulus is mainly composed of type I collagen and forms a firm but flexible outer layer that provides strength and flexibility. The CEP is a 0.1 - 1.6 mm layer of hyaline cartilage between the vertebra and central portion of the disc (nucleus and inner annulus).[12,130] The CEP resists intradiscal pressure and allows nutrient transport by diffusion into the disc from vertebral blood vessels.[12,131]

Early stages of disc degeneration include biochemical changes such as a loss of proteoglycans and hydration.[10] In later stages, morphologic changes occur, including disc height loss, nucleus pulposus herniation, and annular tears.[132] With aging, the CEP becomes calcified and less permeable,[90,133] and consequently, nutrient transport across the endplates decreases with age, injury, and degeneration.[134,135] Damage to the CEP also associates with spinal injury and an increased risk of back pain.[15,16,77] Despite the potentially important role of the CEP in disc degeneration and back pain/injury, CEP morphology and its association with disc degeneration have not been well characterized.

One reason for this lack of characterization is that the CEP has a short T_2 relaxation time, and standard MRI sequences are unable to capture its signal. However, recent studies have demonstrated the feasibility of using a short-TE or ultrashort TE (UTE) MRI sequence for depicting the morphology of the CEP and quantifying the thickness.[18–21] Disc degeneration is often measured with the semi-quantitative Pfirrmann grading method[136], and has also been measured by T_2 and $T_{1\varrho}$ relaxation times. T_2 relaxation time is sensitive to changes in collagen and water,[137,138] while $T_{1\varrho}$ relaxation time is also sensitive to macromolecules and has the potential to identify early biochemical changes in the disc.[139–141]

The objective of this study was to evaluate whether UTE MRI-derived CEP thickness measurements can be made accurately, and associate with adjacent disc degeneration. This association is theoretically plausible since CEP thickness can alter nutrient transport into the disc and thereby affect disc matrix quality (represented by $T_{1\varrho}$). In our first aim, we measured the CEP thickness from 3D UTE images using a novel automatic thresholding algorithm, and validated the algorithm with histology-derived measurements. In our second aim, we measured disc $T_{1\varrho}$ relaxation times and compared these with adjacent CEP thickness measurements. Correlations between MRI-derived CEP thickness values, Pfirrmann grades, and disc $T_{1\varrho}$ were assessed to investigate the usefulness of CEP thickness measurement as a diagnostic tool.

Methods

Image Acquisition

Ten lumbar motion segments (4 L1-L2, 2 L2-L3, 3 L4-L5, 1 L5-S1) with varying degrees of disc degeneration were harvested from six human cadaver spines (age: 58.5 ± 5.2 years, 4 males, 2 females; Table 1) within 1 week post-mortem and scanned with MRI. Each motion segment was

attached to a rigid alignment guide that served as a fiducial marker for aligning UTE MR and histology locations (Figure 33). MR imaging was conducted using a Discovery MR 750W 3T scanner (GE Healthcare, Waukesha, WI) and an eight-channel phased-array wrist coil (Invivo, Gainesville, FL). The imaging protocol included a T_2-weighted 2D fast spin echo (FSE) sequence, a 3D UTE imaging sequence, and a 3D $T_{1\rho}$ mapping sequence. For all three sequences, imaging was performed in the sagittal plane.

T_2-weighted 2D FSE sequence used a repetition time (TR) of 7000 - 8000 ms, TE of 85 - 90 ms, 8 x 8 cm^2 FOV, 256 x 192 matrix size, 1.5 mm slice thickness, and 36 - 44 slices. UTE imaging used 3D radial acquisition combined with nonselective excitation, and scan parameters included 75 μs TE, 15° flip angle, 12 ms TR, 8 x 8 x 7 cm^3 field of view, 0.5 x 0.5 x 1.5 mm^3 spatial resolution, and 40 - 48 slices. Fat suppression was applied every five radial spoke acquisitions to minimize off-resonance artifacts from fatty components in the vertebral bodies. Magnetization-prepared angle-modulated partitioned-k-space spoiled gradient echo snapshots (3D MAPSS)[142] with eight spin-lock times (0, 2, 4, 8, 12, 20, 40, and 80 ms) and 500 Hz spin-lock frequency used for $T_{1\rho}$ mapping in the disc, with imaging parameters of 10 x 10 cm^2 field of view, 256 x 128 matrix size, 4 mm slice thickness, and 14-18 slices. On the same day of MR imaging, motion segments were scanned with high-resolution peripheral quantitative computed tomography (HR-pQCT) with an XtremeCT scanner (Scanco, Medical AG, Bruttisellen, Switzerland), yielding a 41 μm voxel size.

Histology

After imaging, the motion segments were sectioned into 5 - 10mm thick para-sagittal slabs for histology. Slabs were sectioned parallel to the channels of the alignment guide (Figure 33C) to

ensure sections were co-planar with UTE. Two para-sagittal slabs from each motion segment were chosen based on known regions of CEP defects and/or modic regions from MRI. Slabs were fixed, decalcified, and sectioned (7 μm thickness). Sections were stained with a tri-chrome stain containing aniline blue, orange G, and acid fuchsin. For subsequent validation of UTE CEP thickness measurements, CEP thickness was measured on photomicrographs using ImageJ (NIH) at 50 evenly-spaced positions from anterior to posterior.

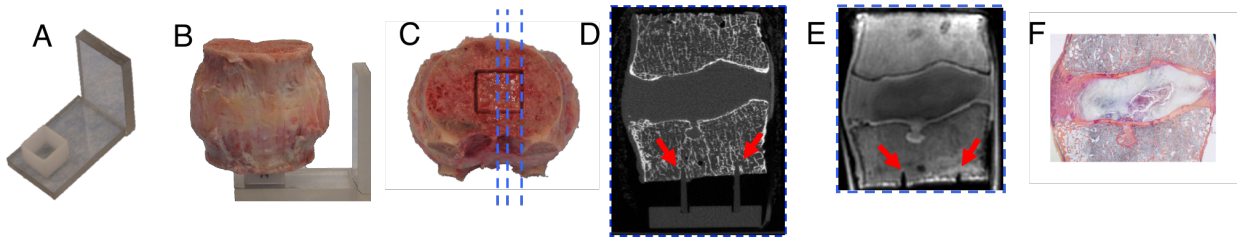

Figure 33. Method for co-aligning histology and MR images. (A-B) Motion segment is placed on rigid alignment guide; (C) histology, HR-pQCT, and MR images are taken parallel to alignment channels to ensure images are co-planar; matching (D) HR-pQCT, (E) MRI and (F) histology slices are determined relative to location of channel (red arrows). Visible channels in (D) and (E) indicate that this slice is within the square grid of the alignment guide.

UTE MRI CEP Thickness Measurement and Validation with Histology

UTE images were interpolated to a voxel size of 0.25 x 0.25 x 0.5 mm^3. Images were then processed using a custom, automated algorithm in Matlab (Mathworks; Natwick, MA) to calculate CEP thickness. The algorithm loops through the following steps for each MRI slice for all motion segments (Figure 34):

(1) Contours the endplates;

(2) Dilates the contours, and masks dilated contours over original image;

(3) Re-bins the data using Lanczos interpolation[143,144] to quadruple the number of pixels (thereby enhancing apparent resolution);

(4) Identifies and crops the inferior and superior endplate regions;

(5) Thresholds each endplate separately using adaptive (region-dependent) Otsu thresholding,[145] in which a unique threshold is calculated for different regions across the endplate with varying image intensity and contrast;

(6) Calculates thickness across the endplate, perpendicular to the tangent line at each location;

(7) Smooths the data using a one-dimensional digital filter

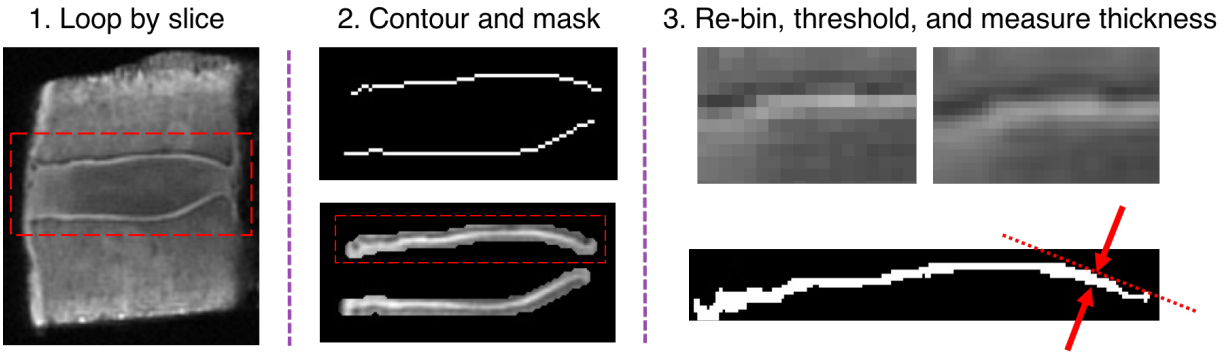

Figure 34. Steps of UTE CEP thickness algorithm. (1) Algorithm loops through MRI slices, (2) contours and masks the endplates, (3) re-bins to increase resolution, thresholds the endplate, and calculates CEP thickness values (red arrows) that are perpendicular to the tangent line (red dotted line) at each horizontal location. Panel 2 shows boxed region in panel 1, and panel 3 shows images for top endplate (dashed box in panel 2).

This algorithm is fully automatic besides the addition of a "threshold multiplier" as an input to certain specimens to tweak each region's threshold by the multiplier value.

Thickness measurements from UTE images were then validated with histology measurements. The matching MRI slice for each histology section was determined using the novel co-alignment method outlined in Figure 33D, which uses the channels from the alignment guide as fiducial markers. Altogether, 21 individual UTE MRI slices from five motion segments were matched to histology sections, yielding 40 matched CEPs (inferior and superior for each slice). For each CEP, thickness measurements were compared between UTE images and histology at each of the 50 evenly-spaced anterior-posterior positions.

Several comparison metrics were used to evaluate the agreement between UTE MRI-derived estimates of CEP thickness and their respective site-matched histology measurements. For UTE-histology pair, the systematic bias and noise in the thickness estimates were determined by calculating the mean difference and root-mean-square deviation (RMSD) for the 50 evenly-spaced anterior-posterior positions. The proportional bias was determined from Bland-Altman plots for each endplate.[146,147] General agreement between the two measurement techniques was assessed using correlation analysis.

MR Image Assessment and Association with Degeneration

Disc degeneration level was assessed using the Pfirrmann scoring system [24] based on T_2-weighted FSE images by a radiologist with 25 years of experience. Table 1 summarizes the donor age/sex and level of each motion segment, along with the associated Pfirrmann grade.

Table 1. Summary of Sample Sets

Motion Segment	Subject	Disc Level	Pfirrmann Grade
1	57 y (Male)	L1-L2	2
2	57 y (Male)	L4-L5	3
3	65 y (Male)	L1-L2	3
4	65 y (Male)	L4-L5	3
5	57 y (Female)	L1-L2	3
6	57 y (Female)	L2-L3	3
7	49 y (Male)	L1-L2	3
8	63 y (Male)	L2-L3	4
9	60 y (Male)	L4-L5	4
10	60 y (Male)	L5-S1	4

$T_{1\varrho}$ values in the disc were calculated using the MAPSS images with the eight different spin-lock times. Monoexponential fitting on a pixel-by-pixel basis was performed using the Levenberg-Marquardt algorithm. Manual segmentation of the disc was performed using the in-house image processing toolkit (IPP)[148] based on the MAPSS images with a spin lock time of 0 ms. The nucleus pulposus regions of the discs were segmented and estimated as the central half-width regions of the discs (along the anterior to posterior direction). It has been shown that the CEP regions adjacent to the nucleus are permeable and allow for nutrient diffusion into the disc.[149] CEP thickness values adjacent to these segmented disc regions were used for correlation analyses.

For each segment, the mean and coefficient of variation (CV) of the CEP thickness, averaged over the segmented superior and inferior CEP regions, were calculated as a possible degeneration biomarker. Two-tailed t-tests were conducted to assess differences in mean CEP

thickness, CV CEP thickness, and mean and standard deviation of $T_{1\varrho}$ between Pfirrmann grades 3 and 4. Only one disc had Pfirrmann grade 2, and thus Pfirrmann grade 2 was not included in t-tests. Univariate linear regression analysis was used to assess correlations between disc properties (mean $T_{1\varrho}$, standard deviation of $T_{1\varrho}$, and Pfirrmann grade) and CEP properties (mean CEP thickness and CV CEP Thickness), and Pearson correlation coefficients were calculated between the mean and standard deviation of $T_{1\varrho}$ and the mean and CV CEP thickness. Significance of statistical tests was defined as $p < 0.05$.

Results

Validation and Results of UTE Thickness Algorithm

Thickness maps from both superior and inferior CEPs for all ten motion segments demonstrated significant heterogeneity (Figure 35). The mean CEP thickness was 0.74 ± 0.04 mm. There was no difference in mean thickness values between superior and inferior CEPs ($p = 0.46$). CEPs tended to be thicker around the periphery and thinner in the central portion. Statistical comparison between histology and UTE-MRI-derived measurements of CEP thickness showed significant agreement (Figure 36). Although UTE MRI over-estimated CEP thickness (mean difference = 0.02 ± 0.13 mm), this over-estimation was not significantly different from zero ($p = 0.32$). UTE MRI had a small but significant proportional bias (-0.25 ± 0.73 mm, $p = 0.03$). This negative proportional bias indicated that UTE MRI's over-prediction of thickness was lesser in locations where the CEP was thicker. Histology and UTE MRI-based measurements of CEP thickness variation were significantly correlated for 28/40 CEP sections. The mean regression slope was 0.35 ± 0.27, indicating that UTE-predicted variations in thickness were generally greater in

magnitude than histology-measured variations in thickness. The random noise (RMSD) of the UTE MRI measurements was 0.23 ± 0.06 mm.

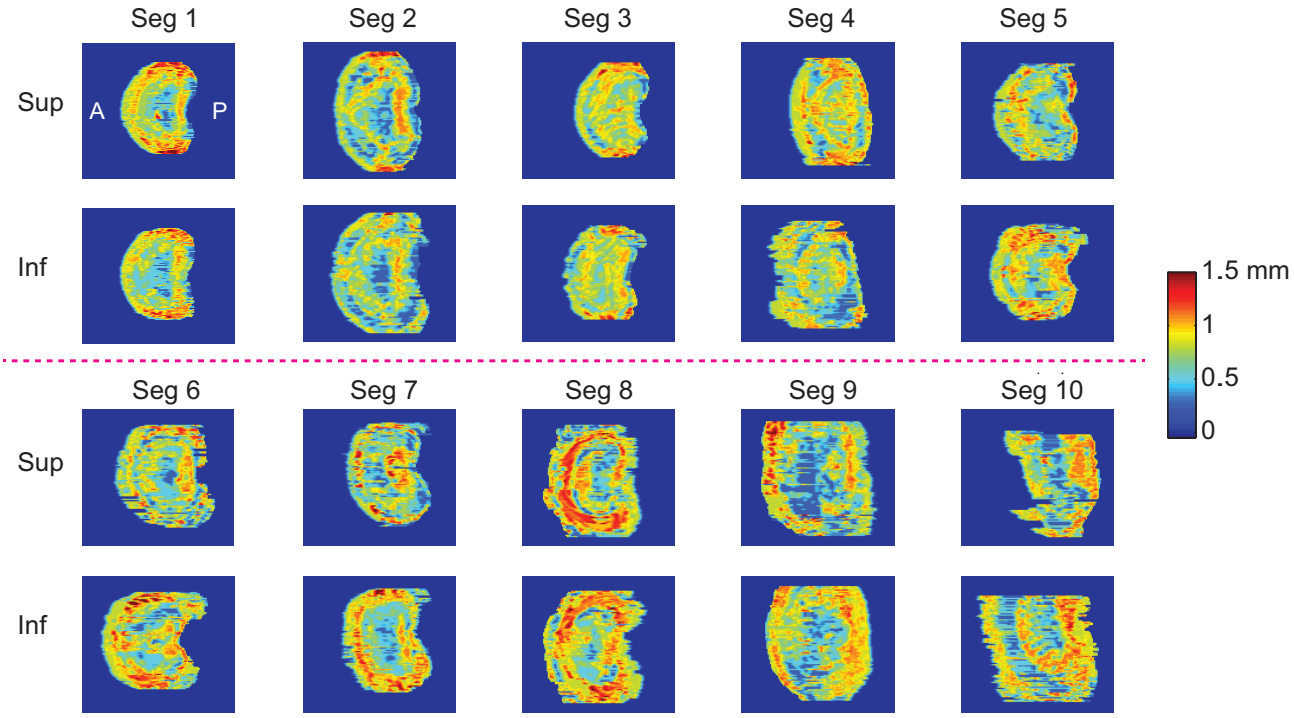

Figure 35. CEP thickness maps measured using Matlab algorithm on UTE images from all ten motion segments. The anterior-posterior direction is from the left to right of the maps.

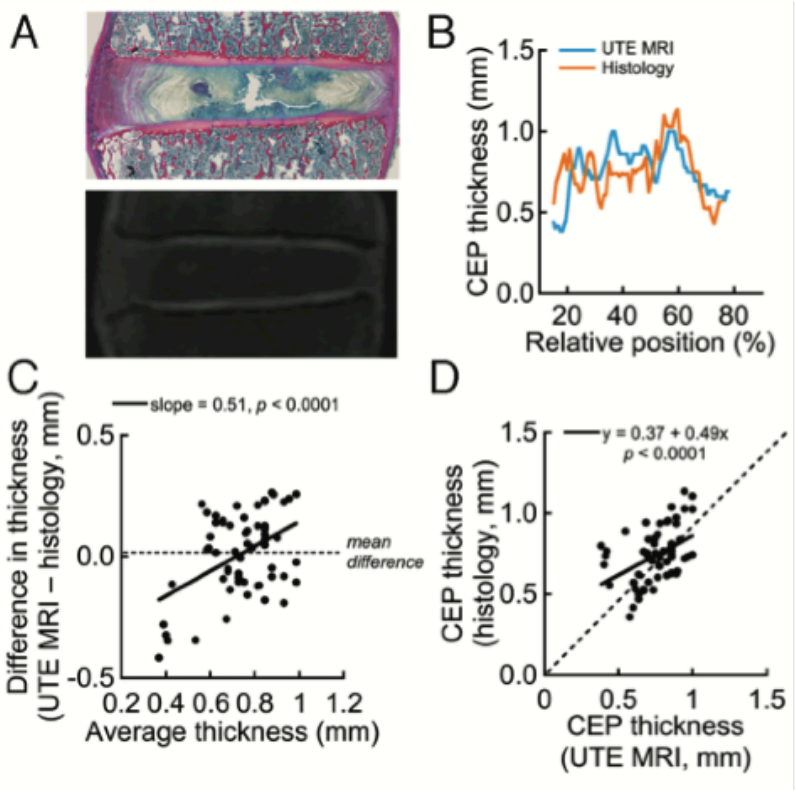

Figure 36. (A) Site-matched histology and UTE MR images; (B) Comparison of CEP thickness between UTE MRI and histology for a selected CEP section; (C) Bland-Altman plot for the same section, where proportional bias (slope) is 0.51 and mean difference is 0.013 mm; (D) Correlation between UTE and histology for the same section (slope = 0.37, which is less than 1, indicating that UTE overestimated the variation in endplate thickness). Dashed line denotes identical thickness measurement between UTE and histology.

Correlations Between CEP Thickness and Disc Degeneration

UTE-derived CEP thickness maps and disc $T_{1\rho}$ maps varied with Pfirrmann grade, with degenerated discs exhibiting poorly-delineated CEPs with point defects and lower thickness values (Figure 37). Several statistical trends were observed between the Pfirrmann grade, CEP thickness from UTE images, and disc $T_{1\rho}$ (Figure 38). Even with a limited sample size, the standard deviation of $T_{1\rho}$ was significantly lower for Pfirrmann grade 4 than Pfirrmann grade 3 ($p < 0.05$). The mean $T_{1\rho}$ also decreased with Pfirrmann grade as observed in previous literature,[139,141] although the difference was not significant. The CV CEP thickness was significantly higher for Pfirrmann grade 4 than Pfirrmann grade 3 ($p < 0.05$), while the mean CEP thickness was unaffected by Pfirrmann grade.

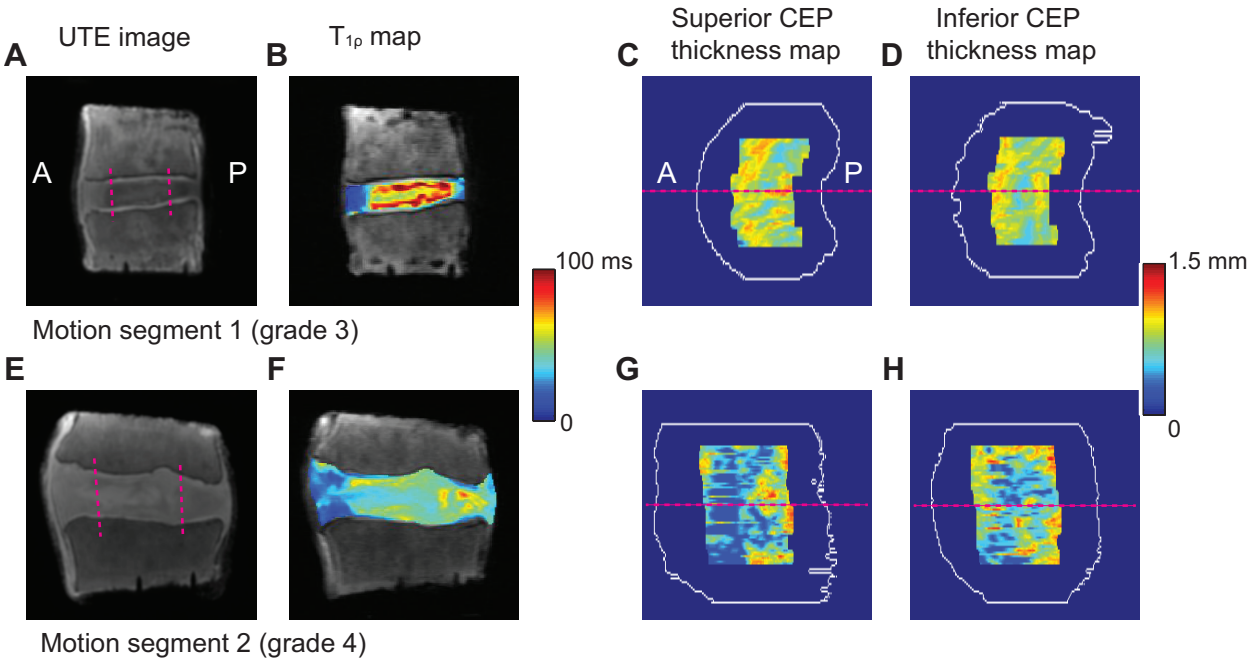

Figure 37. (A,E) UTE images of motion segments with Pfirrmann Grade 3 and 4. Pfirrmann Grade 3 disc has well-delineated CEPs with high and homogeneous thickness values, while Pfirrmann Grade 4 disc has poorly delineated CEPs with point defects and lower thickness

values. The region of the central half width of the disc is denoted with two pink dashed lines. The anterior-posterior direction is from the left to right. (B,F) $T_{1\rho}$ maps in the discs. (C-D,G-H) Thickness maps of CEPs are located superior and inferior to the segmented discs. The white contours represent the overall CEP boundaries before segmentation. The slice locations for (A) and (E) are denoted by pink dashed lines.

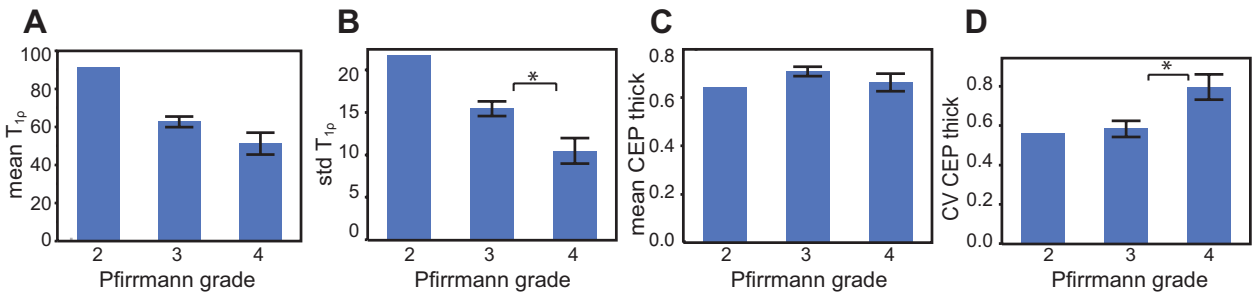

Figure 38. (A-D) The mean and standard deviation of $T_{1\rho}$ in the segmented disc and the mean and CV of CEP thickness averaged between the superior and inferior maps as a function of the Pfirrmann grade. Notably, the standard deviation of $T_{1\rho}$ is significantly lower for Pfirrmann grade 4 than 3 (B), and the CV CEP thickness is significantly higher for Pfirrmann grade 4 than 3 (D). Error bars represent ± standard error. * indicates significant difference in the two-sample t-test ($p < 0.05$).

Linear regression (Figure 39) showed that the standard deviation of $T_{1\rho}$ and CV CEP thickness had a significant negative correlation ($r = -0.65$, $p = 0.04$). The mean $T_{1\rho}$ and CV CEP thickness also had a moderate negative correlation, but this correlation was not significant ($r = -0.36$, $p = 0.31$). The standard deviation of $T_{1\rho}$ and the mean CEP thickness showed a moderate

positive correlation (r = 0.40, p = 0.26), while the mean CEP thickness and mean $T_{1\rho}$ showed no correlation (r = 0.11, p = 0.76).

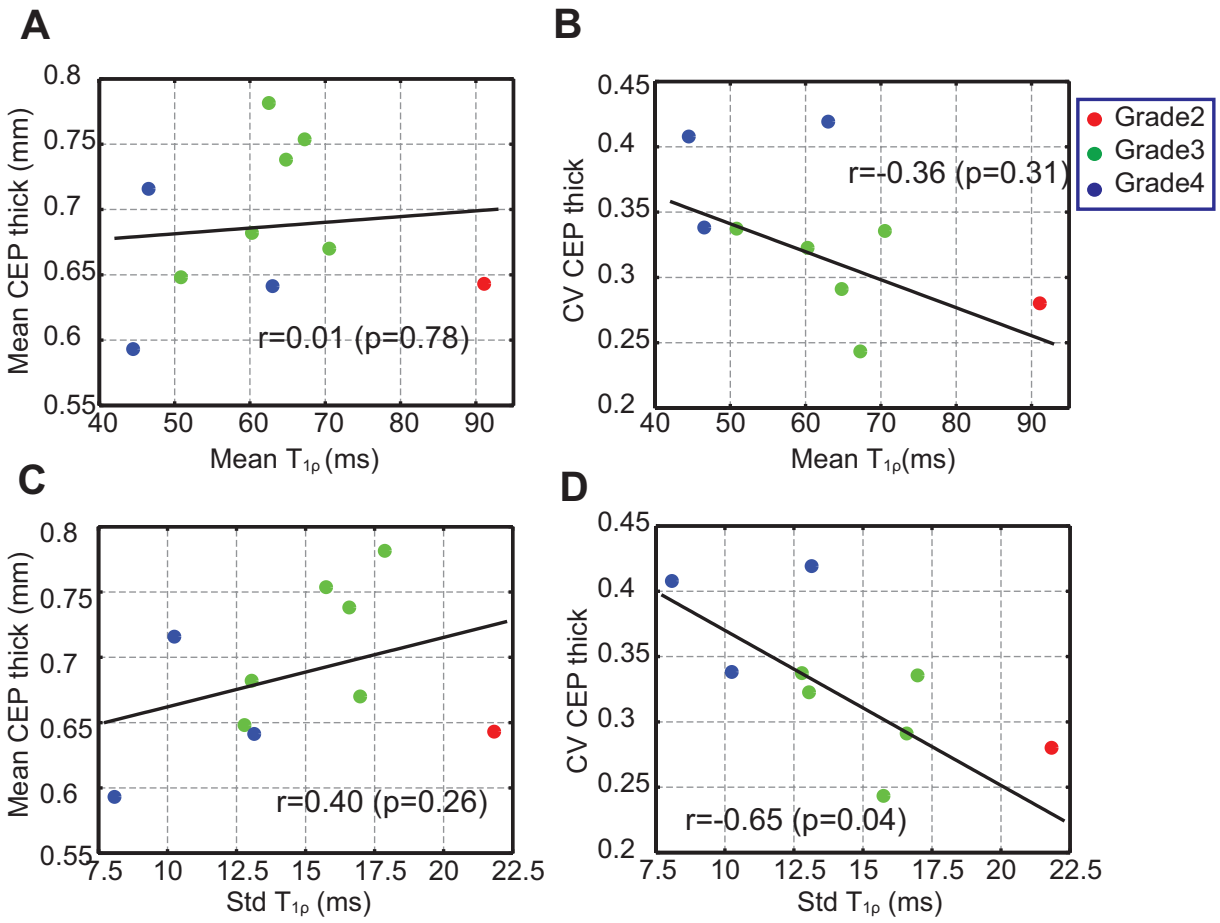

Figure 39. (A-D) Linear regression of the mean and CV of CEP thickness versus the mean and standard deviation of $T_{1\rho}$. The standard deviation of $T_{1\rho}$ and the CV CEP thickness have a significant negative correlation (D). Data points are color-coded by Pfirrmann grade. Pearson correlation coefficients and p-values are also denoted.

Discussion

In this study, we investigated whether quantitative measurements of CEP morphology could be made *in situ*, and whether these measurements have clinical utility. Even with a limited sample size, we observed that the variability in both CEP thickness and $T_{1\varrho}$ were significantly related to degeneration. Specifically, CV CEP thickness and the standard deviation of $T_{1\varrho}$ varied by Pfirrmann grade, and CV CEP thickness had a significant negative correlation with the standard deviation of $T_{1\varrho}$. However, the mean values of both CEP thickness and $T_{1\varrho}$ were not significantly associated with Pfirrmann grade or with each other. Taken together, these findings indicate that spatial heterogeneity in CEP and disc properties are more indicative of degeneration than the more commonly-reported mean values of these properties.

While several studies have reported calcification of the cartilage endplates with degeneration,[134,135] only two studies have quantified human CEP thickness using MRI,[18,20] one of which attempted to correlate CEP thickness with degeneration. These studies used a 3D gradient-echo sequence with a 3.7 ms TE, and calculated CEP thickness by manually outlining the CEP from several slices in ImageJ. No correlations were observed between CEP thickness and degeneration (as assessed by T_2 relaxation time and Pfirrmann grade). However, the authors did not assess heterogeneity in CEP thickness, which our findings suggest may be a more significant indicator of disc degeneration.

We present the first automatic, histologically validated technique for quantitatively measuring CEP thickness in three dimensions using MR images. While other studies have quantified CEP thickness manually and discretely using two-dimensional slices,[18,20,150] no algorithms to date have measured CEP thickness continuously across the entire endplate volume. To maximize histologic correlation, we utilized automatic, region-dependent thresholding that

minimized errors related to signal heterogeneity. The algorithm is being further developed to include measures of CEP curvature and CEP damage fraction. Variations in CEP curvature have been shown to alter the distribution of disc loading,[151] which may ultimately affect disc health.

Previous work has shown that CEP damage co-locates with modic lesions,[15] which are also highly specific predictors of back pain.[152,153] This may be due to factors secreted by nucleus cells that diffuse through damaged CEPs and irritate bone marrow cells. For example, osteoclastic activators are elevated in discs with modic lesions,[154] and coincident cellular behaviors of nucleus and marrow cells indicate detrimental disc/bone crosstalk.[155] Future studies that use similar imaging approaches as we have described here may help delineate associations between CEP damage, modic lesions, and physical symptoms. Given the strong association between CEP damage and back pain/injury,[15,16,77,79] we anticipate that standardized measures of CEP damage will add value to large cohort studies.

This study has several limitations. First, the resolution of the MR images limits the accuracy of CEP thickness measurements. Specifically, the current in-plane resolution was 0.5 x 0.5 mm^2, while the CEP thickness only ranged from 0 – 1.5 mm thick. To counteract the effects of limited resolution, we incorporated a re-sampling step in our algorithm that quadruples the number of pixels. This greatly improved our correlation with histology-based measures of CEP thickness. Second, CEPs were sometimes difficult to segment near the edges of the disc due to decreased contrast between the annulus fibrosus and CEP, leading to overestimation of thickness. However, our correlation analysis between CEP thickness and disc $T_{1\rho}$ was conducted for the central disc, and thus possible errors in the peripheral CEPs did not affect our correlation analysis. Lastly, some specimen images had overall poor contrast, but this was overcome by the addition of the

previously-discussed threshold multiplier. Increased image quality in future studies may allow for removal of the threshold multiplier, making the algorithm fully automatic.

In conclusion, our work demonstrates that quantitative measurements of the spatial variation of CEP thickness measured from UTE images are associated with disc degeneration. Spatial variations in CEP thickness and $T_{1\rho}$ in the disc were strongly associated with Pfirrmann grade. These two parameters may serve as important quantitative and objective diagnostic markers for back pain patients.

Acknowledgements

This work was supported by the National Institutes of Health (NIH) grant AR063705 and GE Healthcare.

Chapter 6: Conclusion

Summary and Main Conclusions

The experiments performed for this dissertation illuminate structural features of the disc-vertebra interface and the influence of structural variations on biomechanical strength and disc degeneration. In particular, results presented in Chapter 2 show that bone loss decreases spinal bending strength and flexibility, and may contribute to an increased risk for disc herniation. Chapter 3 highlights the mechanical weakness of the interface between the cartilage endplate and subchondral bone, and shows that degenerated discs with less dense vertebral endplates are at a higher risk for cartilage avulsion. Chapter 4 presents a histologic classification system for endplate irregularities and uncovers a previously unreported but highly prevalent form of avulsion at the tidemark, which can be seen on clinical MRI. Lastly, Chapter 5 introduces a novel Matlab algorithm for calculating cartilage endplate thickness using ultrashort echo-time MRI, and shows that variation in cartilage endplate thickness is positively correlated with disc degeneration. Taken together, these studies support the following main conclusions:

(1) The disc-vertebra interface is vulnerable to tensile failure due to a **lack of structural integration**;

(2) **Bone density** may be an important factor in maintaining disc-vertebra interface strength;

(3) Separations at the disc-vertebra interface are **visible with clinical imaging**; and

(4) **Cartilage endplate morphology** at the disc-vertebra interface is related to disc degeneration.

Interpretation of Key Findings

In Chapter 4, we discovered that the majority of avulsion-type injuries at the disc-vertebra interface are located at the tidemark – the mineralization front between the annulus and calcified cartilage layer. The tidemark exists along the entire surface of the vertebra. In the outer annulus region, this tidemark joins the annulus and calcified cartilage layer, while in the inner annulus region, the tidemark joins the hyaline cartilage endplate and the calcified cartilage layer (Figure 40).[105] The high prevalence of outer annulus tidemark avulsions found in Chapter 4 suggest that the biomechanical failures between the cartilage endplate and vertebral endplate at the inner annulus that were induced in Chapter 3 may occur specifically at the tidemark between the hyaline cartilage endplate and thin calcified cartilage layer. This is supported by Chapter 3's SEM results showing that cartilage-like tissue was present on both failure surfaces (Figure 24). Various other studies have also observed cartilage endplate-bone avulsions,[16,77,81,106] and further studies are needed to confirm with high-resolution imaging whether these avulsions occur at the tidemark.

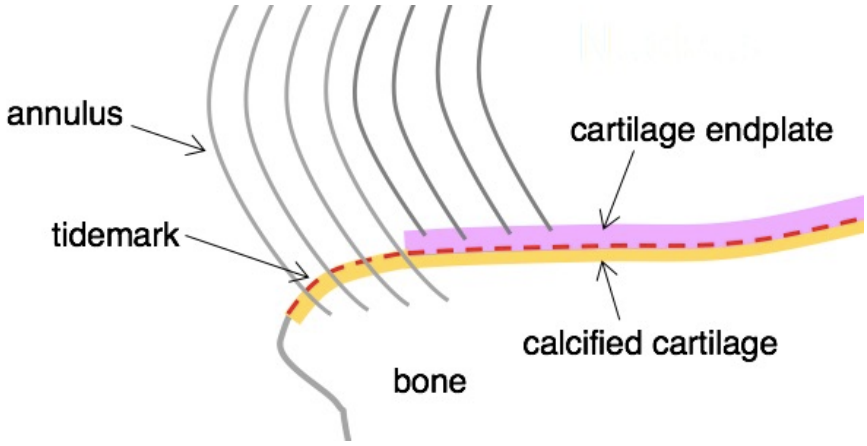

Figure 40. Tidemark anatomy. In the outer annulus, fibers cross the tidemark (red dotted line) and enter the calcified cartilage layer (yellow line). In the inner annulus, fibers enter the hyaline cartilage endplate (pink line), and the tidemark sits between the cartilage

endplate and calcified cartilage layer. The calcified cartilage layer is thicker at the outer annulus and thinner at the inner annulus.

The high prevalence of outer annulus tidemark avulsions without associated disc herniation identified in Chapter 4 suggest that this injury has a different mechanism than the traumatic cartilage endplate-bone avulsions induced in Chapter 3. One possibility is that outer annulus tidemark avulsions are fatigue injuries from repetitive loading, while the inner annulus cartilage endplate-bone avulsions associated with disc herniations[16,77] may be a traumatic injury (e.g. during excessive forward bending). For the latter, the annulus fibrosus must be relatively intact in order to avulse the cartilage endplate from the bone, and therefore may be more common in younger individuals with less degenerated discs. In degenerated discs with disrupted annular lamellae, the annulus itself may fail before the interface fails, although further biomechanical studies are needed to confirm this hypothesis.

This dissertation presents several novel methodologies and results that are important for clinical management of back pain. Notably, results highlight the vulnerability of the disc-vertebra interface and show that even very small disc-vertebra interface separations can be seen using clinical MRI. This suggests that patients with disc-vertebra interface injuries can be identified and selected for specific treatments related to the disc-vertebra interface. Furthermore, we have presented the first automatic thresholding algorithm for quantifying endplate morphology using clinical MRI, and have shown relationships between endplate morphology and disc degeneration. Previous biomechanical and structural studies of the endplate using animal models have limited clinical utility due to significant variation in endplate structure between animals and humans.[156] For example, animals retain growth plates throughout adult life, while the growth plate is absent

in adult humans. Therefore, the human tissue work presented in this dissertation is of great importance for advancing diagnostics and treatments of disc-vertebra interface injury.

Future Work

In Chapter 3, we identified failure mechanisms of the disc-vertebra interface and uncovered structural features of attachment. These data will be useful for complex finite element models of the intervertebral disc with accurate modeling of the interface. Modeling may help clarify the individual mechanistic contributions of small variations in structural features in improving cartilage-bone integration and decreasing stress concentrations at the interface. Data from this study may also help motivate treatments for patients with the disc-vertebra interface injuries observed in Chapters 2-4. Potential therapeutics may include staples or sutures to re-attach avulsed tissue, or a more complex repair method such as interface tissue engineering[157] or 3D printed scaffolds. Stages of degeneration may affect repair choice; for example, bio-glue may seep into vertebral pores of an older-osteoporotic spine and create strong fixation between the disc and vertebra, whereas bio-glue may not be as successful in younger discs with denser vertebral bone. Futures studies may include application of various treatments to avulsed endplates and pull-off tests to assess attachment strength,

The biomechanical experiments in Chapter 3 involved uniaxial tensile testing. Disc herniation is a flexion injury,[30,31] and uniaxial tension mimics the tension caused by annular fiber traction during bending. However, a recent animal study found that disc-vertebra interface failure can occur in complex loading states,[158] and future experiments and/or modeling may explore effects of complex loading states at the human disc-vertebra interface. Additionally, further studies are needed to assess the previously described hypothesis that tidemark avulsions as seen in Chapter

4 may be fatigue injuries from repetitive loading. These studies may involve biomechanical fatigue testing using various loads and loading rates to induce tidemark avulsion-type injuries, as well as structure-function analyses to identify risk factors.

Collectively, the work presented in this dissertation emphasizes the vulnerability of the disc-vertebra interface and uncovers failure mechanisms and important structure-function relationships. These findings will motivate new specialized diagnostics, preventive strategies, and treatments for many patients suffering from low back pain.

Bibliography

1. Vällfors B. 1985. Acute, subacute and chronic low back pain: clinical symptoms, absenteeism and working environment. Scand J Rehabil Med Suppl 11:1–98.

2. Rubin DI. 2007. Epidemiology and Risk Factors for Spine Pain. Neurol Clin 25(2):353–371.

3. Andersson GB. 1999. Epidemiological features of chronic low-back pain. Lancet 354(9178):581–5.

4. Luo X, Pietrobon R, X Sun S, et al. 2004. Estimates and Patterns of Direct Health Care Expenditures Among Individuals With Back Pain in the United States. Spine (Phila Pa 1976) 29(1):79–86.

5. Koes BW, Tulder MW Van, Thomas S. 2006. Clinical review: Diagnosis and treatment of low back pain. Br Med J 332(7555):1430–1434.

6. Deyo RA, Gray DT, Kreuter W, et al. 2005. United States Trends in Lumbar Fusion Surgery for Degenerative Conditions. Spine (Phila Pa 1976) 30(12):1441–1445.

7. Dhillon K. 2016. Spinal Fusion for Chronic Low Back Pain: A " Magic Bullet " or Wishful Thinking? Malaysian Orthop J 10(1):61–68.

8. Van Tulder MW, Koes B, Seitsalo S, Malmivaara A. 2006. Outcome of invasive treatment modalities on back pain and sciatica: An evidence-based review. Eur Spine J 15(SUPPL. 1):82–92.

9. Depalma MJ, Ketchum JM, Saullo T, et al. 2011. What Is the Source of Chronic Low Back Pain and Does Age Play a Role? Pain Medicine 12:224–233.

10. Adams MA, Roughley PJ. 2006. What is Intervertebral Disc Degeneration , and What Causes It? Spine 31(18):2151–2161.

11. Mwale F, Iatridis JC, Antoniou J. 2008. Quantitative MRI as a diagnostic tool of intervertebral disc matrix composition and integrity. Eur Spine J 17(SUPPL. 4):432–40.

12. Roberts S, Menage J, Urban JP. 1989. Biochemical and structural properties of the cartilage end-plate and its relation to the intervertebral disc. Spine (Phila Pa 1976) 14:166–174.

13. Adams MA, Burton K, Bogduk N. 2006. The biomechanics of back pain. Churchill Livingstone Elsevier.

14. Lotz JC, Fields a J, Liebenberg EC. 2013. The role of the vertebral end plate in low back pain. Glob spine J 3(3):153–64.

15. Fields AJ, Liebenberg EC, Lotz JC. 2014. Innervation of pathologies in the lumbar vertebral

end plate and intervertebral disc. Spine J 14(3):513–521.

16. Rajasekaran S, Bajaj N, Tubaki V, et al. 2013. ISSLS Prize winner: The anatomy of failure in lumbar disc herniation: an in vivo, multimodal, prospective study of 181 subjects. Spine (Phila Pa 1976) 38(17):1491–500.

17. Fields AJ, Rodriguez D, Gary KN, et al. 2014. Influence of biochemical composition on endplate cartilage tensile properties in the human lumbar spine. J Orthop Res 32(2):245–252.

18. Moon SM, Yoder JH, Wright AC, et al. 2013. Evaluation of intervertebral disc cartilaginous endplate structure using magnetic resonance imaging. Eur Spine J 22(8):1820–1828.

19. Bae WC, Statum S, Zhang Z, et al. 2013. Morphology of the cartilaginous endplates in human intervertebral Disks with Ultrashort echo Time Mr imaging 1. Radiology 266(2):564–574.

20. DeLucca JF, Peloquin JM, Smith LJ, et al. 2016. MRI quantification of human spine cartilage endplate geometry: Comparison with age, degeneration, level, and disc geometry. J Orthop Res 34(8):1410–1417.

21. Fields AJ, Han M, Krug R, Lotz JC. 2015. Cartilaginous End Plates: Quantitative MR Imaging with Very Short Echo Times—Orientation Dependence and Correlation with Biochemical Composition. Radiology 274(2):482–489.

22. Thomopoulos S, Williams GR, Gimbel J a., et al. 2003. Variation of biomechanical, structural, and compositional properties along the tendon to bone insertion site. J Orthop Res 21(3):413–419.

23. Thomopoulos S, Marquez JP, Weinberger B, et al. 2006. Collagen fiber orientation at the tendon to bone insertion and its influence on stress concentrations. J Biomech 39(10):1842–1851.

24. Dunlop JWC, Weinkamer R, Fratzl P. 2011. Artful interfaces within biological materials. Mater Today 14(3):70–78.

25. Liu Y, Birman V, Chen C, et al. 2011. Mechanisms of Bimaterial Attachment at the Interface of Tendon to Bone. J Eng Mater Technol 29(1):997–1003.

26. Jazrawi LM, Alaia MJ, Chang G, et al. 2011. Advances in magnetic resonance imaging of articular cartilage. J Am Acad Orthop Surg 19(7):420–429.

27. Paietta RC, Burger EL, Ferguson VL. 2013. Mineralization and collagen orientation throughout aging at the vertebral endplate in the human lumbar spine. J Struct Biol 184(2):310–320.

28. Nosikova YS, Santerre JP, Grynpas M, et al. 2012. Characterization of the annulus fibrosus-vertebral body interface: Identification of new structural features. J Anat 221(6):577–589.

29. Johnston SL, Campbell MR, Scheuring R, Feiveson AH. 2010. Risk of Herniated Nucleus Pulposus Among U.S. Astronauts. Aviat Space Environ Med 81(6):566–574.

30. Adams MA, Hutton WC. 1982. Prolapsed intervertebral disc. A hyperflexion injury 1981 Volvo Award in Basic Science. Spine (Phila Pa 1976) 7(3):184–91.

31. McNally DS, Adams MA, Goodship AE. 1993. Can intervertebral disc prolapse be predicted by disc mechanics? Spine (Phila Pa 1976) 18(11):1525–30.

32. Belavý DL, Adams M, Brisby H, et al. 2016. Disc Herniations In Astronauts : What Causes Them, And What Does It Tell Us About Herniation On Earth ? Eur Spine J 25(1): 144-154.

33. Wing PC, Tsang IK, Susak L, et al. 1991. Back pain and spinal changes in microgravity. Orthop Clin North Am 22(2):255–62.

34. Young KS, Rajulu S. 2011. The Effects of Microgravity on Seated Height (Spinal Elongation). NASA Hum Res Progr Investig Work NASA Houston, TX USA .

35. Matsumura Y, Kasai Y, Obata H, et al. 2009. Changes in water content of intervertebral discs and paravertebral muscles before and after bed rest. J Orthop Sci 14(1):45–50.

36. Adams M, Dolan P. 1996. Time-dependent changes in the lumbar spine's resistance to bending. Clin Biomech 11(4):194–200.

37. Adams MA, Dolan P, Hutton WC. 1987. Diurnal variations in the stresses on the lumbar spine. Spine (Phila Pa 1976) 12:130–137.

38. Rannou F, Richette P, Benallaoua M, et al. 2003. Cyclic tensile stretch modulates proteoglycan production by intervertebral disc annulus fibrosus cells through production of nitrite oxide. J Cell Biochem 90(1):148–57.

39. Belavý DL, Armbrecht G, Richardson C a, et al. 2011. Muscle atrophy and changes in spinal morphology: is the lumbar spine vulnerable after prolonged bed-rest? Spine (Phila Pa 1976) 36(2):137–45.

40. Adams MA, McNally DS, Wagstaff J, Goodship AE. 1993. Abnormal stress concentrations in lumbar intervertebral discs following damage to the vertebral bodies: a cause of disc failure? Eur Spine J 1(4):214–221.

41. McNally DS, Adams MA. 1992. Internal intervertebral disc mechanics as revealed by stress profilometry. Spine (Phila Pa 1976) 17(1):66–73.

42. Leblanc A, Schneider V, Shackelford L, et al. 2000. Bone mineral and lean tissue loss after long duration space flight. J Musculoskel Neuron Interact 1(2):157–160.

43. Lang T, LeBlanc A, Evans H, et al. 2004. Cortical and trabecular bone mineral loss from the spine and hip in long-duration spaceflight. J Bone Miner Res 19(6):1006–12.

44. Edgerton VR, Zhou MY, Ohira Y, et al. 1995. Human fiber size and enzymatic properties after 5 and 11 days of spaceflight. J Appl Physiol 78(5):1733–1739.

45. Bailey JF, Hargens AR, Cheng KK, Lotz JC. 2012. Post-Spaceflight Recovery of Biomechanical Properties of Murine Intervertebral Discs. Gravitational Sp Biol 26(2):38–47.

46. Bailey JF, Hargens AR, Cheng KK, Lotz JC. 2014. Effect of microgravity on the biomechanical properties of lumbar and caudal intervertebral discs in mice. J Biomech 47(12):2983–8.

47. Sinha RK, Shah SA, Hume EL, Tuan RS. 2002. The effect of a 5-day space flight on the immature rat spine. Spine J 2(4):239–243.

48. Guerin HAL, Elliott DM. 2006. Degeneration affects the fiber reorientation of human annulus fibrosus under tensile load. J Biomech 39(8):1410–1418.

49. Green T, Adams M, Dolan P. 1993. Tensile properties of the annulus fibrosus. Eur Spine J 2:209–214.

50. Watts NB. 1999. Clinical utility of biochemical markers of bone remodeling. Clin Chem 45:1359–1368.

51. Deftos LJ. 1998. Clinical Essentials of Calcium and Skeletal Disorders. Professional Communications.

52. Vico L, Collet P, Guignandon A, et al. 2000. Effects of long-term microgravity exposure on cancellous and cortical weight-bearing bones of cosmonauts. Lancet 355(9215):1607–1611.

53. Jee WS, Wronski TJ, Morey ER, Kimmel DB. 1983. Effects of spaceflight on trabecular bone in rats. Am J Physiol 244:R310–R314.

54. Morey ER, Baylink DJ. 1978. Inhibition of bone formation during space flight. Science 201:1138–1141.

55. Turner RT, Evans GL, Wakley GK. 1995. Spaceflight results in depressed cancellous bone formation in rat humeri. Aviat Sp Environ Med 66:770–774.

56. Wing P, Tsang I, Gagnon F, et al. 1992. Diurnal changes in the profile shape and range of motion of the back. Spine (Phila Pa 1976) 17:761–766.

57. Noyes FR, DeLucas JL, Torvik PJ. 1974. Biomechanics of anterior cruciate ligament failure: an analysis of strain-rate sensitivity and mechanisms of failure in primates. J Bone Joint Surg Am 56(2):236–253.

58. Rodrigues S a., Wade KR, Thambyah A, Broom ND. 2012. Micromechanics of annulus-end plate integration in the intervertebral disc. Spine J 12(2):143–150.

59. Inoue H. 1981. Three-Dimensional Architecture of Lumbar Intervertebral Discs. Spine (Phila Pa 1976) 6(2):139–146.

60. Shirazi-Fard Y, Kupke JS, Bloomfield SA, Hogan HA. 2013. Discordant recovery of bone mass and mechanical properties during prolonged recovery from disuse. Bone 52(1):433–43.

61. Barou O, Valentin D, Vico L, et al. 2002. High-resolution three-dimensional micro-computed tomography detects bone loss and changes in trabecular architecture early: comparison with DEXA and bone histomorphometry in a rat model of disuse osteoporosis. Invest Radiol 37:40–46.

62. Evans GL, Morey-Holton E, Turner RT. 1998. Spaceflight has compartment- and gene-specific effects on mRNA levels for bone matrix proteins in rat femur. J Appl Physiol 84:2132–2137.

63. Westerlind KC, Turner RT. 1995. The skeletal effects of spaceflight in growing rats: tissue-specific alterations in mRNA levels for TGF-beta. J Bone Miner Res 10:843–848.

64. Adams MA, Freeman BJ, Morrison HP, et al. 2000. Mechanical initiation of intervertebral disc degeneration. Spine (Phila Pa 1976) 25:1625–1636.

65. Pollintine P, Dolan P, Tobias JH, Adams MA. 2004. Intervertebral disc degeneration can lead to "stress-shielding" of the anterior vertebral body: a cause of osteoporotic vertebral fracture? Spine (Phila Pa 1976) 29:774–782.

66. Kwok AWL, Wang Y-XJ, Griffith JF, et al. 2012. Morphological changes of lumbar vertebral bodies and intervertebral discs associated with decrease in bone mineral density of the spine: a cross-sectional study in elderly subjects. Spine (Phila Pa 1976) 37:E1415-21.

67. Alini M, Eisenstein SM, Ito K, et al. 2008. Are animal models useful for studying human disc disorders/degeneration? Eur Spine J 17(1):2–19.

68. Oshima H, Ishihara H, Urban JP, Tsuji H. 1993. The use of coccygeal discs to study intervertebral disc metabolism. J Orthop Res 11(3):332–8.

69. Wilke H, Neef P, Caimi M, et al. 1999. New In Vivo Measurements of Pressures in the Intervertebral Disc in Daily Life. Spine (Phila Pa 1976) 24(8):755–762.

70. Ishihara H, McNally DS, Urban JP, Hall AC. 1996. Effects of hydrostatic pressure on matrix synthesis in different regions of the intervertebral disk. J Appl Physiol 80(3):839–46.

71. Elliott DM, Sarver JJ. 2004. Young Investigator Award Winner: Validation of the Mouse and Rat Disc as Mechanical Models of the Human Lumbar Disc. Spine (Phila Pa 1976) 29(7):713–722.

72. Callaghan JP, McGill SM. 1995. Frozen storage increases the ultimate compressive load of porcine vertebrae. J Orthop Res 13:809–812.

73. Panjabi MM, Krag M, Summers D, Videman T. 1985. Biomechanical time-tolerance of fresh cadaveric human spine specimens. J Orthop Res 3:292–300.

74. Smeathers JE, Joanes DN. 1988. Dynamic compressive properties of human lumbar intervertebral joints: a comparison between fresh and thawed specimens. J Biomech 21:425–433.

75. Dhillon N, Bass E, Lotz J. 2001. Effect of Frozen Storage on the Creep Behavior of Human Intervertebral Discs. Spine (Phila Pa 1976) 26(8):883–888.

76. Gleizes V, Viguier E, Féron JM, et al. 1998. Effects of freezing on the biomechanics of the intervertebral disc. Surg Radiol Anat 20:403–407.

77. Lama P, Zehra U, Balkovec C, et al. 2014. Significance of cartilage endplate within herniated disc tissue. Eur Spine J 23(9):1869–77.

78. Mann DC, Rajmaira S. 1990. Distribution of Physeal and Nonphyseal Fractures in 2,650 Long-Bone Fractures in Children Aged 0-16 Years. J Pediatr Orthop 10:713–716.

79. Thompson KJ, Dagher AP, Eckel TS, et al. 2009. Modic changes on MR images as studied with provocative diskography: clinical relevance--a retrospective study of 2457 disks. Radiology 250(3):849–855.

80. Wade KR, Robertson P a., Broom ND. 2011. A fresh look at the nucleus-endplate region: New evidence for significant structural integration. Eur Spine J 20(8):1225–1232.

81. Balkovec C, Adams MA, Dolan P, McGill SM. 2015. Annulus Fibrosus Can Strip Hyaline Cartilage End Plate from Subchondral Bone: A Study of the Intervertebral Disk in Tension. Glob spine J 5(5):360–5.

82. Thompson JP, Pearce RH, Schechter MT, et al. 1990. Preliminary evaluation of a scheme for grading the gross morphology of the human intervertebral disc. Spine (Phila Pa 1976) 15(5):411–415.

83. Roberts S, McCall IW, Menage J, et al. 1997. Does the thickness of the vertebral subchondral bone reflect the composition of the intervertebral disc? Eur Spine J 6(6):385–389.

84. Silva MJ, Wang C, Keaveny TM, Hayes WC. 1994. Direct and computed tomography thickness measurements of the human, lumbar vertebral shell and endplate. Bone 15(4):409–414.

85. Wang Y, Battié MC, Boyd SK, Videman T. 2011. The osseous endplates in lumbar vertebrae: Thickness, bone mineral density and their associations with age and disk degeneration. Bone 48(4):804–809.

86. Raghupathy R, Witzenburg C, Lake SP, et al. 2011. Identification of Regional Mechanical Anisotropy in Soft Tissue Analogs. J Biomech Eng 133(9):91011.

87. Lecompte D, Smits A, Bossuyt S, et al. 2006. Quality assessment of speckle patterns for digital image correlation. Opt Lasers Eng 44(11):1132–1145.

88. Hulme PA, Boyd SK, Ferguson SJ. 2007. Regional variation in vertebral bone morphology and its contribution to vertebral fracture strength. Bone 41(6):946–957.

89. Wang Y, Owoc JS, Boyd SK, et al. 2013. Regional variations in trabecular architecture of the lumbar vertebra: Associations with age, disc degeneration and disc space narrowing. Bone 56(2):249–254.

90. DeLucca JF, Cortes DH, Jacobs NT, et al. 2016. Human cartilage endplate permeability varies with degeneration and intervertebral disc site. J Biomech 49(4):550–557.

91. Brown S, Rodrigues S, Sharp C, et al. 2016. Staying connected: structural integration at the intervertebral disc-vertebra interface of human lumbar spines. Eur Spine J :1–11.

92. Adams M a, Green TP, Dolan P. 1994. The strength in anterior bending of lumbar intervertebral discs. Spine (Phila Pa 1976) 19(19):2197–2203.

93. Law T, Anthony M-P, Chan Q, et al. 2013. Ultrashort time-to-echo MRI of the cartilaginous endplate: Technique and association with intervertebral disc degeneration. J Med Imaging Radiat Oncol 57(4):427–434.

94. Ayache J, Beaunier L, Boumendil J, et al. 2010. Artifacts in Transmission Electron Microscopy. In: Sample Preparation Handbook for Transmission Electron Microscopy. New York, NY: Springer New York; p 125–170.

95. Benjamin M, Kumai T, Milz S, et al. 2002. The skeletal attachment of tendons--tendon "entheses". Comp Biochem Physiol A Mol Integr Physiol 133(4):931–945.

96. Adams MA, McNally DS, Chinn H, Dolan P. 1994. Posture and the compressive strength of the lumbar spine. Clin Biomech 9(1):5–14.

97. Willburger RE, Ehiosun UK, Kuhnen C, et al. 2004. Clinical Symptoms in Lumbar Disc Herniations and Their Correlation to the Histological Composition of the Extruded Disc Material. Spine (Phila Pa 1976) 29(15):1655–1661.

98. Yoshiaki H, Nakahara S. 1989. A pathologic study of lumbar disc herniations in the elderly. Spine (Phila Pa 1976) 14(9):1020–1024.

99. Tanaka M, Nakahara S, Inoue H. 1993. A Pathologic Study of Discs in the Elderly. Spine (Phila Pa 1976) 18(11):1456–1462.

100. Arce CA, Dohrmann GJ. 1985. Thoracic disc herniation. Improved diagnosis with computed tomographic scanning and a review of the literature. Surg Neurol 23(4):356–361.

101. Genin GM, Kent A, Birman V, et al. 2009. Functional grading of mineral and collagen in the attachment of tendon to bone. Biophys J 97(4):976–985.

102. Ho SP, Kurylo MP, Fong TK, et al. 2010. The biomechanical characteristics of the bone-periodontal ligament-cementum complex. Biomaterials 31(25):6635–6646.

103. Wagermaier W, Gupta HS, Gourrier A, et al. 2006. Spiral twisting of fiber orientation inside bone lamellae. Biointerphases 1(1):1.

104. Zehra U, Bow C, Lotz JC, et al. 2017. Structural vertebral endplate nomenclature and etiology: a study by the ISSLS Spinal Phenotype Focus Group. Eur Spine J. In review.

105. Junhui L, Zhengfeng M, Zhi S, et al. 2015. Anchorage of annulus fibrosus within the vertebral endplate with reference to disc herniation. Microsc Res Tech 78(9):754–760.

106. Rodrigues S a, Thambyah A, Broom ND. 2015. A multiscale structural investigation of the annulus-endplate anchorage system and its mechanisms of failure. Spine J 15(3):405–16.

107. Berg-Johansen B, Liebenberg EC, Li A, et al. 2015. Spaceflight-induced bone loss alters failure mode and reduces bending strength in murine spinal segments. J Orthop Res :1–10.

108. Sonne-Holm S, Jacobsen S, Rovsing H, Monrad H. 2013. The epidemiology of Schmorl's nodes and their correlation to radiographic degeneration in 4,151 subjects. Eur Spine J 22(8):1907–1912.

109. Pfirrmann CW, Resnick D. 2001. Schmorl nodes of the thoracic and lumbar spine: radiographic-pathologic study of prevalence, characterization, and correlation with degenerative changes of 1,650 spinal levels in 100 cadavers. Radiology 219(2):368–374.

110. Samartzis D, Mok FPS, Karppinen J, et al. 2014. Classification of Schmorl's nodes of the lumbar spine and association with disc degeneration: A large-scale population-based MRI study. Osteoarthr Cartil 24(10):1753–1760.

111. Vernon-Roberts B, Moore RJ, Fraser RD. 2007. The natural history of age-related disc degeneration: the pathology and sequelae of tears. Spine (Phila Pa 1976) 32(25):2797–2804.

112. Melrose J, Smith SM, Little CB, et al. 2008. Recent advances in annular pathobiology provide insights into rim-lesion mediated intervertebral disc degeneration and potential new approaches to annular repair strategies. Eur Spine J 17(9):1131–1148.

113. Osti OL, Vernon-Roberts B, Moore R, Fraser RD. 1992. Annular tears and disc degeneration in the lumbar spine. A post-mortem study of 135 discs. J Bone Joint Surg Br 74(5):678–682.

114. Hilton RC, Ball J. 1984. Vertebral rim lesions in the dorsolumbar spine. Ann Rheum Dis 43(2):302–307.

115. Cohen NP, Foster RJ, Mow VC. 1998. Composition and Dynamics of Articular Cartilage : Structure, Function, and Maintaining Healthy State. J Orthop Sports Phys Ther 28(4):203–215.

116. Resnick D, Niwayama G, Guerra J, et al. 1981. Spinal vacuum phenomena: anatomical study and review. Radiology 139(2):341–8.

117. Schweitzer ME, El-Noueam KI. 1998. Vacuum disc: Frequency of high signal intensity on t2-weighted MR images. Skeletal Radiol 27(2):83–86.

118. DF F, PC M. 2001. Nomenclature and Classificaiton of Lumbar Disc Pathology. Spine 26(5):1-.

119. Shan Z, Chen H, Liu J, et al. 2017. Does the high-intensity zone (HIZ) of lumbar Intervertebral discs always represent an annular fissure? Eur Radiol 27(3):1267–1276.

120. Aprill C, Bogduk N. 1992. High-intensity zone: A diagnostic sign of painful lumbar disc on magnetic resonance imaging. Br J Radiol 65(773):361–369.

121. Schellhas KP, Pollei SR, Gundry CR, Heithoff KB. 1996. Lumbar disc high intensity zone: correlation of magnetic resonance imaging and discography. Spine (Phila Pa 1976) 21:79–86.

122. Carragee EJ, Paragioudakis SJ, Khurana S. 2000. 2000 Volvo Award winner in clinical studies: Lumbar high-intensity zone and discography in subjects without low back problems. Spine (Phila Pa 1976) 25(23):2987–92.

123. Rankine J, Gill K, Hutchinson C, et al. 1999. The Clinical Significance of the High-Intensity Zone on Lumbar Spine Magnetic Resonance Imaging. Spine (Phila Pa 1976) 24(18):1913.

124. Gornet MF, Hipp JA, Copyay AG, Schranck FW. 2017. The Effect of Abnormal Disc Mechanics on Activities of Daily Living. Int Soc Adv Spine Surg Conf Abstr :Abstract Number 711.

125. Katz JN. 2006. Lumbar disc disorders and low-back pain: socioeconomic factors and consequences. J Bone Joint Surg Am 88 Suppl 2:21–24.

126. Hoy D, Bain C, Williams G, et al. 2012. A systematic review of the global prevalence of low back pain. Arthritis Rheum 64(6):2028–2037.

127. Luoma K, Riihimäki H, Luukkonen R, et al. 2000. Low Back Pain in Relation to Lumbar Disc Degeneration. Spine (Phila Pa 1976) 25(4):487–492.

128. Peng B, Hou S, Wu W, et al. 2006. The pathogenesis and clinical significance of a high-intensity zone (HIZ) of lumbar intervertebral disc on MR imaging in the patient with discogenic low back pain. Eur Spine J 15(5):583–587.

129. Raj PP. 2008. Intervertebral disc: Anatomy-physiology-pathophysiology-treatment. Pain Pract 8(1):18–44.

130. Moore RJ. 2000. The vertebral end-plate: what do we know? Eur Spine J 9(2):92–96.

131. Urban JP, Holm S, Maroudas A, Nachemson A. 1977. Nutrition of the intervertebral disk. An in vivo study of solute transport. Clin Orthop Relat Res (129):101–114.

132. Modic MT, Ross JS. 2007. Lumbar Degenerative Disk Disease. Radiology 245(1):43–61.

133. Martin MD, Boxell CM, Malone DG. 2002. Pathophysiology of lumbar disc degeneration: a review of the literature. Neurosurg focus 13(2):1-6.

134. Roberts S, Urban JPG, Evans H, Eisenstein SM. 1996. Transport Properties of the Human Cartilage Endplate in Relation to its Composition and Calcification. Spine (Phila Pa 1976) 21(4):415–420.

135. Bernick SOL, Cailliet R. 1982. Vertebral end-plate changes with aging of human vertebrae. Spine (Phila Pa 1976) 7(2):97–102.

136. Pfirrmann CWA, Metzdorf A, Zanetti M, et al. 2001. Magnetic Resonance Classification of Lumbar Intervertebral Disc Degeneration. Spine 26(17):1873–1878.

137. Weidenbaum M, Foster RJ, Best B a, et al. 1992. Correlating magnetic resonance imaging with the biochemical content of the normal human intervertebral disc. J Orthop Res 10(4):552–561.

138. Perry J, Haughton V, Anderson PA, et al. 2006. The value of T2 relaxation times to characterize lumbar intervertebral disks: Preliminary results. Am J Neuroradiol 27(2):337–342.

139. Pandit P, Talbott JF, Pedoia V, et al. 2016. T1ϱ and T2-based characterization of regional variations in intervertebral discs to detect early degenerative changes. J Orthop Res 34(8):1373–1381.

140. Auerbach JD, Johannessen W, Borthakur A, et al. 2006. In vivo quantification of human lumbar disc degeneration using T1ϱ-weighted magnetic resonance imaging. Eur Spine J 15(S3):338–344.

141. Blumenkrantz G, Zuo J, Li X, et al. 2010. In vivo 3.0-tesla magnetic resonance T1ϱ and T2 relaxation mapping in subjects with intervertebral disc degeneration and clinical symptoms. Magn Reson Med 63(5):1193–1200.

142. Li X, Han ET, Busse RF, Majumdar S. 2008. In vivo T1rho mapping in cartilage using 3D magnetization-prepared angle-modulated partitioned k-space spoiled gradient echo snapshots (3D MAPSS). Magn Reson Med 59(2):298–307.

143. Lanczos C. 1938. Trigonometric Interpolation of Empirical and Analytical Functions. Stud Appl Math 17(1–4):123–199.

144. Madhukar BN, Narendra R. 2013. Lanczos Resampling for the Digital Processing of Remotely Sensed Images. Proc Int Conf VLSI, Commun Adv Devices, Signals & Syst Netw 258:403–411.

145. Otsu N. 1979. A threshold selection method from gray-level histograms. IEEE Trans Syst Man Cybern 9(1):62–66.

146. Bland JM, Altman DG. 1999. Measuring agreement in method comparison studies. Stat Methods Med Res 8(2):135–160.

147. Martin Bland J, Altman D. 1986. Statistical Methods for Assessing Agreement Between Two Methods of Clinical Measurement. Lancet 327(8476):307–310.

148. Carballido-Gamio J, Bauer J, Lee K-Y, et al. 2005. Combined image processing techniques for characterization of MRI cartilage of the knee. Conf Proc Annu Int Conf IEEE Eng Med Biol Soc IEEE Eng Med Biol Soc Annu Conf 3:3043–6.

149. Nachemson A, Lewin T, Maroudas A, Freeman MAR. 1970. In Vitro Diffusion of Dye Through the End-Plates and the Annulus Fibrosus of Human Lumbar Inter-Vertebral Discs. Acta Orthop Scand 41(6):589–607.

150. Setton LA, Zhu W, Weidenbaum M, et al. 1993. Compressive properties of the cartilaginous end-plate of the baboon lumbar spine. J Orthop Res 11(2):228–239.

151. Langrana NA, Kale SP, Edwards WT, et al. 2006. Measurement and analyses of the effects of adjacent end plate curvatures on vertebral stresses. Spine J 6(3):267–278.

152. Weiner BK, Vilendecic M, Ledic D, et al. 2015. Endplate changes following discectomy: natural history and associations between imaging and clinical data. Eur Spine J 24(11):2449–2457.

153. Dudli S, Fields AJ, Samartzis D, et al. 2016. Pathobiology of Modic changes. Eur Spine J 25(11).

154. Torkki M, Majuri ML, Wolff H, et al. 2016. Osteoclast activators are elevated in intervertebral disks with Modic changes among patients operated for herniated nucleus pulposus. Eur Spine J 25(1):207–216.

155. Dudli S, Sing DC, Hu SS, et al. 2017. ISSLS Prize in Basic Science 2017: Intervertebral disc/bone marrow cross-talk with Modic changes. Eur Spine J :1–12.

156. Zhang Y, Lenart BA, Lee JK, et al. 2014. Histological Features of Endplates of the Mammalian Spine. Spine (Phila Pa 1976) 39(5):E312–E317.

157. Seidi A, Ramalingam M, Elloumi-Hannachi I, et al. 2011. Gradient biomaterials for soft-to-hard interface tissue engineering. Acta Biomater 7(4):1441–1451.

158. Berger-Roscher N, Casaroli G, Rasche V, et al. 2017. Influence of Complex Loading Conditions on Intervertebral Disc Failure. Spine (Phila Pa 1976) 42(2):E78–E85.

Appendix A: Pilot Testing for Four-Point Bending

Chapter 2 presented a novel method for four-point bending of murine discs using custom 3D printed fixtures. Due to the small size of the intervertebral disc space in murine motion segments, micro-compression pilot testing combined with X-ray imaging was performed to assure that bone-on-bone contact did not occur. Bone-on-bone contact would skew the data with large contact forces. This pilot testing is described below.

Objective: Visualize bending of samples with X-ray to check for bone-on-bone contact

Method: Attached custom four-point bending system to vice (Figure 41, left) and took X-ray images at incremental displacements of the vice. Actual displacements were calculated post-testing using ImageJ.

Results: Bone-on-bone contact was not observed (Figure 41, right).

Conclusion: The custom-designed four-point bending test does not produce bone-on-bone contact that would skew loading results.

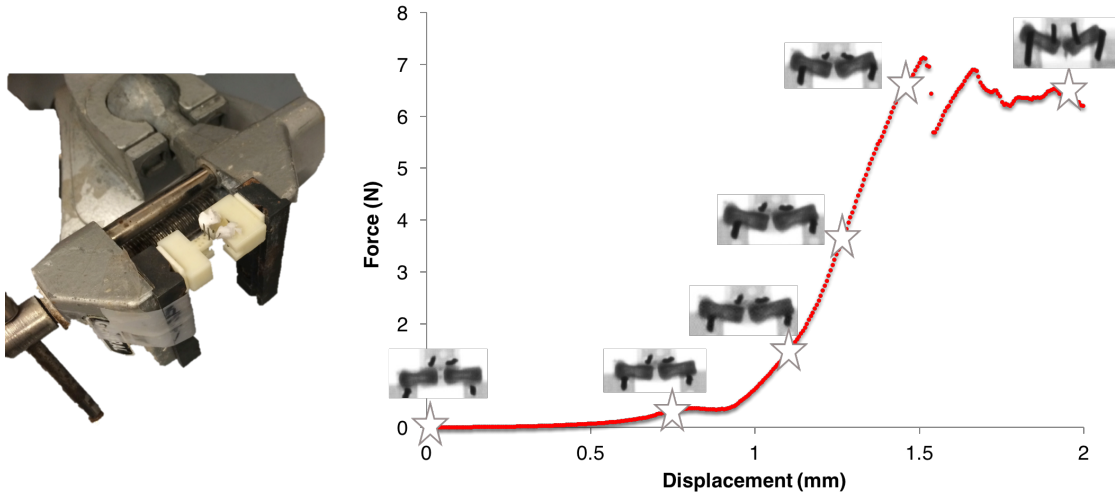

Figure 41. (Left) Four-point bending supports attached to vice. (Right) Pilot test data with overlaid micro-compression X-rays, showing no bone-on-bone contact. Stars represent displacement where each X-ray was taken.

Appendix B: Table of Disc Height and Thompson Grade for Chapter 3

Chapter 3 presented a manuscript in press titled "Structure-Function Relationships at the Disc-Vertebra Interface." The following table was not included in the manuscript but is included here for reference.

Table 2. Disc height and Thompson grade for each disc. *Images for Spine #2 were unavailable for analysis, as noted in Chapter 3.

Spine #	Level	Disc height (mm)	Thompson Grade
1	T11-T12	5.8	2
	T12-L1	5.9	2
2	T8-T9	*	*
	T10-T11	*	*
	T11-T12	*	*
3	T12-L1	6.7	2
4	T11-T12	9.4	3
	T12-L1	9.0	3
5	T11-T12	7.8	2
	T12-L1	7.3	2
6	T10-T11	4.7	4
	T11-T12	5.8	4
	T12-L1	8.6	3
7	T12-L1	7.5	2

Appendix C: Additional Tidemark Avulsion Images

Chapter 4 identified a highly prevalent form of avulsions at the tidemark between the outer annulus and calcified cartilage at the vertebral rim, and found that these tidemark avulsions were visible on T_2-weighted MRI as high-intensity. This appendix provides additional examples of tidemark avulsions as seen on histology and MRI (Figure 42).

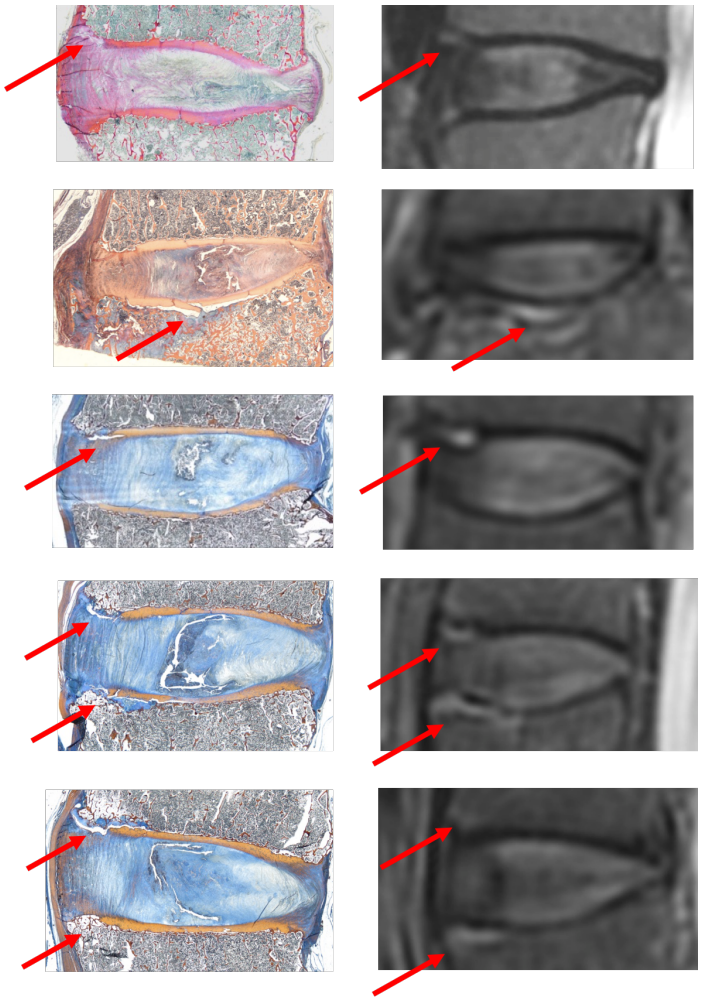

Figure 42. Avulsions on histology (left) and T_2-weighted MRI (right) for five discs. Histology slices on left are approximately matched with MRI slices on right. Note that avulsion of the cartilage endplate from bone (second row) also shows HIZ on MRI.

Appendix D: Additional Contributions

This appendix includes the abstracts for two manuscripts that do not directly relate to my dissertation for which I was second author and contributed my efforts. I have listed my contributions for each.

The Effect of Simulated Microgravity on Lumbar Spine Biomechanics: an *in vitro* Study

Cory J. Laws, Britta Berg-Johansen, Alan R. Hargens, Jeffrey C. Lotz

Published in: European Spine Journal

Abstract

Purpose: Disc herniation risk is quadrupled following spaceflight. This study tested the hypothesis that swelling-induced disc height increases (comparable to those reported in spaceflight) stiffen the spine and elevate annular strain and nuclear pressure during forward bending.

Methods: Eight human lumbar motion segments were secured to custom-designed testing jigs and subjected to baseline flexion and compression and pure moment flexibility tests. Discs were then free-swelled in saline to varying supraphysiologic heights consistent with prolonged weightlessness and re-tested to assess biomechanical changes.

Results: Swelling-induced disc height changes correlated positively with intradiscal pressure ($p < 0.01$) and stiffening in flexion ($p < 0.01$), and negatively with flexion range of motion ($p < 0.05$). Swelling-induced increases in disc height also led to increased annular surface strain under combined flexion with compression. Disc wedge angle decreased with swelling ($p < 0.05$); this loss of wedge angle correlated with decreased flexion range of motion ($R^2 = 0.94, p < 0.0001$) and decreased stiffness fold change in extension ($p < 0.05$).

Conclusion: Swelling-induced increases in disc height decrease flexibility and increase annular strain and nuclear pressure during forward bending. These changes, in combination with the measured loss of lordotic curvature with disc swelling, may contribute toward increased herniation risk. This is consistent with clinical observations of increased disc herniation rates after microgravity exposure and may provide the basis for future countermeasure development.

My contributions to this study included data analysis, contributing to writing the manuscript, and responding to reviewer comments.

Alterations in Intervertebral Disc Composition, Matrix Homeostasis and Biomechanical Behavior in the UCD-T2DM Rat Model of Type 2 Diabetes

Aaron J. Fields, Britta Berg-Johansen, Lionel N. Metz, Stephanie Miller, Brandan La, Ellen C. Liebenberg, Dezba G. Coughlin, James L. Graham, Kimber L. Stanhope, Peter J. Havel, Jeffrey C. Lotz

Published in: Journal of Orthopaedic Research

Abstract

Type 2 diabetes (T2D) adversely affects many tissues, and the greater incidence of discogenic low back pain among diabetic patients suggests that the intervertebral disc is affected too. Using a rat model of polygenic obese T2D, we demonstrate that diabetes compromises several aspects of disc composition, matrix homeostasis, and biomechanical behavior. Coccygeal motion segments were harvested from 6-month-old lean Sprague-Dawley rats, obese Sprague-Dawley rats, and diabetic

obese UCD-T2DM rats (diabetic for 69 ± 7 days). Findings indicated that diabetes but not obesity reduced disc glycosaminoglycan and water contents, and these degenerative changes correlated with increased vertebral endplate thickness and decreased endplate porosity, and with higher levels of the advanced glycation end-product (AGE) pentosidine. Consistent with their diminished glycosaminoglycan and water contents and their higher AGE levels, discs from diabetic rats were stiffer and exhibited less creep when compressed. At the matrix level, elevated expression of hypoxia-inducible genes and catabolic markers in the discs from diabetic rats coincided with increased oxidative stress and greater interactions between AGEs and one of their receptors (RAGE). Taken together, these findings indicate that endplate sclerosis, increased oxidative stress, and AGE/RAGE-mediated interactions could be important factors for explaining the greater incidence of disc pathology in T2D.

My contribution to this manuscript involved harvesting rat motion segments, conducting all biomechanical tests, and helping with data analysis and interpretation.

Publishing Agreement

It is the policy of the University to encourage the distribution of all theses, dissertations, and manuscripts. Copies of all UCSF theses, dissertations, and manuscripts will be routed to the library via the Graduate Division. The library will make all theses, dissertations, and manuscripts accessible to the public and will preserve these to the best of their abilities, in perpetuity.

Please sign the following statement:

I hereby grant permission to the Graduate Division of the University of California, San Francisco to release copies of my thesis, dissertation, or manuscript to the Campus Library to provide access and preservation, in whole or in part, in perpetuity.

Author Signature Britta Berg-Johansen

Date 6/11/17